POLITECNICO DI MILANO

DIPARTIMENTO DI ENERGIA

Doctoral Programme in Energy and Nuclear Science and Technology

XXXII Cycle (2016-2019)

Remaining Wear Life Prediction of Aviation Hydraulic Pump Based on Monitoring Abrasive Debris Generation

(The Ph.D. Thesis)

Doctoral Dissertation of:	Tongyang Li
Supervisors:	Prof. Enrico Zio (POLITECNICO DI MILANO)
	Prof. Shaoping Wang (BEIHANG UNIVERSITY)
Tutor:	Prof. Francesco Di Maio
Coordinator:	Prof. Vincenzo Dossena

8 October, 2019, Beijing

Acknowledgements

This thesis is completed under the careful guidance of my supervisors, Prof. Wang Shaoping and Prof. Enrico Zio. In my several years of doctoral study, Prof. Wang gave me selfless help and care in my study, life and other aspects. Prof. Wang's noble personality, serious and responsible attitude towards work, meticulous spirit of scholarship, vigorous style of life is the model of my life. Prof. Wang is the guiding light on my path towards scientific research. She has taught me to face all the problems in my study and work with a scientific way of thinking, a steadfast attitude towards work and an unyielding spirit of studying. Meanwhile, I felt so privileged to spent an 18-month life learning from Prof. Zio, who provides me substantial supports by exemplary guidance, great technical supports, numberless insightful discussions, timeless patience, and constant encouragements throughout all the course of this thesis. His humorous attitude towards life and inquisitive research spirit impressed me a lot. Here I would like to express my highest respect and heartfelt thanks to my supervisors Prof. Wang Shaoping and Prof. Enrico Zio! In the future life and work, I will remember those valuable things both professors taught me and pass them on.

I would like to express my special appreciation and thanks to Prof. Francesco Di Maio, for his selfless help on my joint-Ph.D. enrollment into Politecnico Di Milano. Thanks to the students and teachers of LASAR for accompanying me to study and live in Milan: Prof. Piero Baraldi, Miao Yu, Prof. Prof. Yu Yu, Prof. Zou Yanhua, Gao haifeng, Wang Wei, Yang Zhe, Chen Shiyu, Xu Mingjing, su huai, Lv Xuefei, Hao zhaojun, Liu yue, Pang ji, Federico Antonello, Dario Valcamonico, Edoardo, Luca Bellani, Seyed Mojtaba Hoseyni.

I would also like to thank China Scholarship Council and the Education Office of Embassy of P. R. China in Italy for awarding me the scholarship under the support of State Scholarship Fund, allowing me to pursue the 18-month study in Politecnico di Milano as joint-P h.D. student.

Thank my parents for what they have done for my growth. From my birth to now, every step of my growth is inseparable from your care and education. Now that I am about to graduate and go to work, I will spend the rest of my life repaying my parents for raising me. I sincerely wish them good health and happiness! Thank you to my family and friends!

[This page intentionally left blank.]

Abstract

Compared with service life prediction, the remaining useful life prediction depends on not only the performance degradation model, but also the accurate estimation of current system degradation state. The degradation of an aviation hydraulic pump is largely caused by the abrasive wear of frictional pairs. Since the structure of aviation hydraulic pump is complex, there is no onboard monitoring method being able to detect the exact wear state of the pump, which prevents the system from being accurately predicted. The abrasive debris, as the main product of abrasive wear, have drawn much attention since early ages and have been used as an indicator for the diagnosis and prognosis. The main problem is that currently there is no available degradation model describing the degradation process based on features of debris, meanwhile, because of the high-throughput of hydraulic flow in aviation hydraulic system, the detection of debris features is challenged by the aliasing problems caused by the short distance of two adjacent debris particles. Besides, the techniques to predict the remaining useful life are not complete. The debris-based prediction method is still far from being practically used.

Aiming at solving the problems mentioned above, the study mainly considers the following works:

(1) For the paucity of available degradation models for features of debris, the study proposed a mesoscale numerical modeling method combining both macroscale stress distribution with microscale rough surfaces. The method is able to solve the count, size distribution and morphology of generated debris under certain work conditions and given surface roughness. The method can be applied for arbitrary scales of debris to reduce the computational cost.

(2) For more accurate data acquisition, the aliasing problem caused by the superimposed induced voltages of debris should be overcome, so that the degradation state can be well estimated. The study proposed a signal separation method based on degenerate unmixing estimation technique. By combining with the convolutional neural networks, the method is able to achieve online signal separation.

(3) The degradation model can rarely cover all the degradation paths, which results in

modeling uncertainty. Meanwhile, noise can hardly be avoided during the measuring process, which results in measuring uncertainty. The modeling uncertainty and measuring uncertainty will then lead to inaccurate estimation of current state of the system. The study proposed an adaptive-order particle filter based prediction method which is able to promote the short-term and long-term predicting accuracy.

Key words: remaining useful life, abrasive debris, aliasing error, performance degradation, particle filter, reliability.

Contents

List of figures

List of tables

SECTION I. GENERALITIES

This section of the dissertation describes the context of the Ph.D. research, its relevance, the state-of-the-art methods, the challenges that are addressed and the overview of the developed method.

1. Introduction

An aircraft hydraulic power supply system provides high-pressure fluid for the actuation system, braking system, landing gear system, and other sub-function systems. As the power source of an aircraft hydraulic system, an aviation piston pump's performance influences flight safety directly. Therefore, an aircraft prognostics and health management (PHM) system appears to keep high reliability and long life of an aerial piston pump. In PHM technologies, an accurate estimation of the remaining useful life (RUL) is the most difficult issue because it is related to the failure physics and stress spectrum imposed on a hydraulic pump. Since the structure of an aviation piston pump is very complicated, its failure generation and development are comprehensively affected by inner frictional pairs with uncertain characteristics. Statistically, an aviation piston pump shows variant degradation paths under diversiform operating conditions, which unavoidably brings about a great deal of uncertainties and difficulties in the analytic solution of the RUL. Although the life of a certain type of aviation piston pump can be obtained through tens of thousands of hours of experiments under a fixed spectrum, it is difficult to give the exact RUL under an arbitrary condition. A prognostic estimation method of RUL is imminently needed, which will highly benefit the reduction of costs by providing the possibility to define predictive maintenance strategies and prolonging useful life.

Since abrasive wear is believed to be the main failure mode of the aviation piston pump, this work mainly focuses on predicting the remaining wear life of aviation piston pump. There are four main friction pairs in a typical aviation piston pump: pair of the cylinder block and the valve plate, pair of the swash plate and the slipper, pair of the slipper and the piston, and pair of the piston and the cylinder block. Under normal circumstances, oil film exists between the friction pairs. It is shown that the fully lubricating condition become mixed lubrication and wear occurs and becomes serious with an increase of the serving time [1]. The wear makes the displacement between friction pairs become larger and leakage happens. The leakage caused by wear can lead

to a decrease of the outlet flow rate, which will eventually result in the failure of pump. In an actual hydraulic system of an aircraft, the outlet flow is controlled to be at a stable value, which means that the decline of the outlet flow cannot be monitored.

There are two main difficulties for modeling the degradation of pump. One difficulty is related to insufficient data for data-driven modeling: as components in aircraft are highly reliable, they rarely fail and life tests usually take several thousand hours [2, 3]. The other one is that there is no deterministic model to describe the degrading paths due to the complex degradation mechanisms occurring in axial piston pumps under a variety of conditions. Some works tried to investigate oil film and contact principles for improved design [4, 5], but the models and results can seldom be used for life prediction. On the other hand, abrasive wear between the main friction pairs is believed to be the main degradation mechanism, as supported by analyses and experimental results [6, 7]. Considering these aspects, the system modeling and current state acquisition or estimation cannot be well integrated with existing health indicators. In other words, the current state can be measured by the return oil flow, as health indicator, but there is no model of system operation as a function of the return oil flow.

There are also difficulties for monitoring the wear degradation of pump. The real wear state can be observed by atomic force microscopy (AFM) or transmission electron microscopy (TEM), but the devices cannot be used on an assembled product, which makes the state of pump can hardly be detected online. Wear debris, as the direct product of wear, is employed as health indicator in recent years, which can be measured by several online oil debris detection methods [8, 9]. However, the accuracy still cannot be held at an acceptable level especially for high-throughput and high-concentration aviation hydraulic system.

In addition, the modeling and measuring process will unavoidably bring about uncertainties. Since we are not able to machine the product as our expectation, the machining error may make the pump operate away from the model, which is recognized as modeling uncertainty. The noises caused by the vibration and environmental factors make the measurement process keep away from accurate, which is recognized as measuring uncertainty. The modeling and measuring uncertainties lead to the

mismatching of the model and monitoring data, which will influence the predicting accuracy.

In this Ph.D. thesis, the objective is to develop a feasible method for remaining wear life prediction of aviation axial piston pump, which includes I. modeling of abrasive debris generation based on wear mechanism to characterize the system behavior under different operational conditions, including different lubricating conditions and working pressures, II. online abrasive debris detection method especially for aliasing signal processing to promote the accuracy of measurement, III. uncertainty processing method to eliminate the mismatching problem caused by modeling and measuring uncertainties, and, IV. remaining useful life prediction framework based on monitoring abrasive debris generation to provide accurate predicting result.

The main original contribution of the research lies in the development of a complete method for predicting remaining wear life of aviation axial piston pumps. Specifically, we have developed novel methods for addressing the following three issues: 1) modeling abrasive debris generation given arbitrary concerning scale and working stress with fixed initial roughness, 2) restoring aliasing signals for debris feature statistics with limited detecting sensors, 3) processing uncertainties caused by modeling and measuring for a comprehensive matching result.

1.1 Abrasive debris particles generation

The relative motion for transmission, breaking and damping effects between two sliding surfaces which are known as a friction pair inevitably brings about material loss. During the wear process, the contact stress results in the generation of wear debris which contains critical information of the wear status of the contact surfaces and has been studied for the relation with wear since early ages [10].

Wear debris analysis has long been a powerful method to examine the status of mechanical systems. Limited to the instruments, until the ferrography was introduced, the underlying causes that produced wear debris were analyzed and interpreted [11]. Anderson analyzed the wear debris recorded by ferrography over a period of about 10 years since 1971 and gave out primeval relationship between particle features (quantity, size, shape and composition) and wear characteristics (severity, rate, mode and source) [12]. With the development of ferrography and other debris detection methods [13-15] like optics, capacitance, resistance, ultrasonic and electromagnetic induction, wear debris obtains a more accurate and precise monitoring. Currently, wear debris has been deemed to be an indicator of wear states. Wang et al. [16] modeled wear state evolution by recognizing features from online ferrographic images. Hong et al. [10] suggested the peak in debris generation rate as the indicator of failure. Consequently, experimental results and statistical data [17-19] on various engineering machines under multiple working conditions provide bases for the subsequent studies of the wear debris generation mechanism.

Microscale wear mechanism is complicated and is commonly used to interpret macroscale experimental results. The more micro the observation is, the less the distance is believed between the results and the truth. Being distinguished from micro mechanism and macro results, the mesoscale wear debris is considered to be an intermediate product based on the micro mechanism and its statistical characteristics consist a macro result.

Despite passing over a half century, the primitive observation result is still the fundamental relation of wear currently [20]. Holms proposed an atoms removal theory

in 1946 when discussed the conductivity of electrical contacts, which was the basic form of the classical Archard's law [21]. The Archard's law states that the wear volume is proportional to the normal force and sliding distance while the constant wear coefficient is fully empirical [22]. Archard's law has been verified by numerous experimental results in macroscopic scale [23-25], however, an accurate prediction model is still missing for the complex systematic mechanism in determining the wear coefficient under different materials and lubricating conditions [20]. In the past two decades, with the help of advanced technologies such as AFM and TEM, the deformed asperities which were abraded atom by atom gradually were observed in nanoscale [26, 27]. Jacobs indicated that Archard's law failed in the regime of nanoscale contacts [27, 28]. They found that with nanoscale sliding, silicon atoms are worn off without fracture. Similar phenomenon was found in Diamond [29], Diamond-like carbon which is widely used coating material [28] and metallic materials [30, 31]. Later, Jacobs proposed an atomic attrition mechanism [26, 32]. This microscale mechanism makes it possible to give out a predictive result of wear. Inspired by the mechanism, Aghababaei et al. [33] found that the atomic attrition more likely happens when the junction size of two asperities is small while fractured attrition exists when the junction size is larger, which gives a uniform explanation of the two mechanisms. Atomic simulations by using molecular dynamics (MD) [34-36] is usually conducted on single asperity. These simulations seldom establish connections with macroscopic results. Practically, wear debris, as the product of macroscale wear and result of microscale hypothesis, provides a potential to predict macro wear with micro theories.

Conducting an experiment on wear usually takes large amount of time while the experiment results rarely cover all the degradation paths under multi-stage work conditions. Whereas, people always try to figure out the exact change of the contact surfaces. Therefore, theoretical understanding of the debris generation mechanism and the corresponding simulative analysis gain increasing efforts. Generally, the generation of debris is influenced by wear modes, stress conditions, lubrication states and material deformation and failure criterion, which makes it a systematic problem and difficult to be analytically described. Considering the numerical methods, finite element method

(FEM) is commonly used in modeling wear process [37-39]. FEM, in fact, shows advantages in macro-scale analysis that a macroscopic geometry with distributed stress conditions can be well solved. Practically, the size of a wear particle is in the 1-500 μm range while the radius of a contact surface may be several decimeters, which means the mesh should be quiet fine and will cause huge computational cost. Although there are methods to build a rough surface for FEM [40], a steep asperity may cause a singular solution which will make the previous time consumption invalid. The boundary element method (BEM) requires only the discretization of boundaries and reduces the computational cost sharply compared to FEM [41]. Therefore, BEM has been widely used in solving rough surface contact and wear problems [42-44]. Allwood [45] compared the existing approaches and found that when the grid points are more than 2000, the conjugate gradient method (CGM) [46] performed fastest and the error of pressure and contact region is about 0.5%. Liu et al. [47] proposed a discrete convolution and fast Fourier transform (DC-FFT) technique which also had a good performance but it is more suitable for rough surfaces generated by periodical force like ball bearing. By using these methods, Akchurin et al. [48, 49] proposed a wear particle model in running-in stage and verified the model using experimental results. Done et al. [50] analyzed the fretting wear and the effect of debris was also included which showed a better result than that without considering the debris. At asperity level, BEM meets the requirement of speed and accuracy and is then employed in this work to model wear debris generation.

1.2 Wear debris detection and aliasing signal processing

Currently, the return oil flow is the commonly used indicator for the prognosis of aviation hydraulic pumps [51]. To obtain the indicator, hydraulic pumps should be taken down from the aircraft, which cannot meet the requirement of condition-based maintenance (CBM). Other indicators, like output pressure and vibration signals, are limited in information by the operational conditions, and thus contain few characteristics useful for the prognosis. On the other hand, aviation hydraulic pumps are typical rotatory machines and the wear of the three main frictional pairs is the primary cause of the output pressure degradation. Debris detection methods, then, show a great potential for the diagnosis and prognosis of aviation hydraulic pumps. Different from applications on engines [52], rolling bearings [53], and many other machines [54, 55], abrasive debris detection methods have to face adverse circumstances when being applied to the pump detection because the oil is not only used for lubrication, but for the power transmission as well.

1.2.1 Wear debris detection

By ferrography [11], people started to establish the relationship between debris features and characteristics of material loss [12]. Nowadays online debris detection methods were introduced and debris analysis has become a powerful approach for interpreting material loss and providing prognostic information. Existing methods include optics, capacitance, resistance, ultrasonic, x-ray and inductive methods [56]. Compared with the other methods, the inductive sensors are usually easily-installed on oil pipes and able to differentiate ferrous debris from non-ferrous debris [57].

Research studies [10, 56] indicate that for engineering applications the sizes of debris usually range from $1\mu m$ to $150\mu m$ under normal work conditions. When severe wear happens, the sizes of debris will follow a different distribution. Several inductive sensors have been designed to promote the detection precision. Hong, et al. [13] proposed a radial inductive sensor which can detect $20\mu m$ thick ferromagnetic debris

in 20mm diameter pipes. Li, et al. [58] introduced a high throughput inductive pulse sensor which is able to detect 50μm debris in lubrication oil with a high throughput. Zhu, et al. [9] utilized a sensor array which is able to detect debris at a flow rate of 460mL/min. High precision means identifying more debris from the same contaminative oil. High throughput results in short time-interval, which will influence the detecting performance. Large diameter pipes will reduce the intensity and uniformity of magnetic field.

1.2.2 Aliasing signal processing of inductive debris detection method

The inductive sensor generates independent pulses as long as the distances between the debris which pass through the pipes are large enough. However, if two wear particles are close enough, the two induced voltages of the sensor will be superposed and an aliasing signal will be generated, as shown in Figure 1. In such a situation, when two wear debris particles are wrongly recognized as one, both the concentration and the size of the debris will be influenced. According to Reference [12], during normal machine separation, wear debris exhibits a constant concentration and small size. The concentration and size of particles increase gradually with time when abnormal wear begins. The accumulative error caused by aliasing will influence the abrasive debris detection precision. Because of the complexity of the wear and tear of a hydraulic pump, aliasing happens more frequently in debris detection. Due to the high flow rate, this situation is serious under certain pipe diameters.

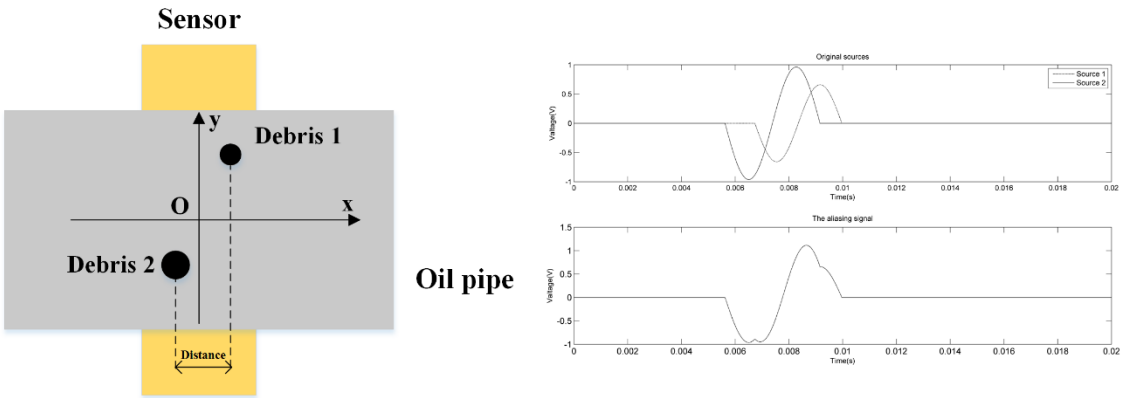

Figure 1. The aliasing phenomenon.

In prior work, an RMF-based debris detection method [13] using inductive techniques was proposed, and the method exhibited good performance in wear particles monitoring. Experiments show that the aliasing phenomenon appears so frequently that it often leads to inaccurate detection. In contrast with the application to the lubrication oil, debris detection in an aviation hydraulic pump is much more difficult because the output high pressure oil leads to a high oil flow rate, which means that much more information is included in the same length of a signal section under the same sampling frequency. If the sampling frequency is not high enough, only one pulse can be detected and it will display error information. Therefore, the issue of how to extract accurate information of the wear particles from the aliasing signals is extremely urgent in RMF detection.

Although inductive wear sensors have different precision and accuracy levels in detecting wear particles [58-61], few works have investigated the aliasing problem. Zhong et al. [62] proposed a new layout of sensors for the aliasing signals and gave a theoretical analysis. On the other hand, the literature on signal extraction [63-65] typically only addresses independent pulses for small flow rates. In fact, the aliasing problem is to some extent similar to the cocktail party problem [66], which is widely researched in speech recognition. Both problems focus on recognizing different sources from mixed signals. Among the speech recognition methods, independent component analysis (ICA) shows good performance in processing linear mixtures of signals produced by multiple sources and has been successfully used for the separation of other kinds of signals. Han et al. [67] used the FAST-ICA (an implementation of the fast fixed-point algorithm for ICA) and wavelet packet method to separate the vibration signals of rolling bearings mixed by a set of sources. The problem is that, when using ICA methods, the number of sensors should be more than the number of sources and all of the mixed signals should be synchronized. In debris detection systems, the sources are the superposed voltages induced by the wear particles, which means that the sources are far more than the sensors and the synchronization of detection can hardly be conducted. Alexander et al. [68] proposed a degenerate unmixing estimation technique (DUET) to separate sources from the time-frequency domain and, in their later works

[69], the time-frequency mask is used to demix the sources. This method assumes that the environment is anechoic and the sources are independent, which is consistent with the debris detection situation. For speech recognition, the background noise usually gives a negative contribution to the source separation. In DUET, high weights caused by the background noise will decrease the accuracy of demixing. To reduce the influence of the noise, Hussain et al. proposed an adaptive noise cancellation technique [70], and Chong et al. [71] combined the method with particle filtering. Hong et al. employed the band pass filter to enhance the signal-to-noise ratio (SNR) of the sensor by 2.67 times [72].

1.3 Remaining useful life prediction of axial piston pump

Over past decades, a lot of research has been conducted in estimating the RUL of machinery. The methods can be generally divided into two categories [73]: data-driven methods and model-based methods. Typical data-driven methods based on machine learning are artificial neural networks (ANNs) and the hidden semi-Markov model (HSMM). Zangenehmadar et al. [74] used an ANN to assess the RUL of pipelines successfully in which more than 80000 groups of data were used for training. Dong et al. [75-77] applied the HSMM function for machine health prognosis and verified the method by using data from a real hydraulic pump health monitoring application case study. In fact, the data used for training were far more than the sample size of a certain type of aviation piston pump. Several thousands of hours were taken to obtain only one set of lift-cycle data of an aviation piston pump [78]. He et al. [79] presented a health monitoring and prognostic method using the PSO-SVM to predict the RUL for an axial piston pump. The small sample problem is what makes an aviation piston pump distinguish from traditional machinery. Model-based methods like physics-of-failure (POF) and filter-based methods are also widely utilized for prediction of component life. Liu et al. [80] developed a failure physics model for the creep fatigue of a piston, and the degradation mechanism was analyzed for prognosis. Lamoureux et al. [81] defined a health indicator to describe the degradation of an aircraft engine fuel pumping unit by using a linear regression method. To build a model by POF, the mechanism needs to be known firstly. Thereby, this kind of method can hardly be used in a complicated system like an aviation piston pump whose failure mechanism is still under research. Filter-based functions take advantages in combining system models with experimental data. For linear systems with Gaussian noise, Kalman filter (KF) is a commonly used prognostic technique, and its effectiveness has been proven in many works [82-85]. Extended KF (EKF) and unscented KF (UKF) methods are modified KFs to cope with non-linear systems while limitation is shown in some systems with high nonlinearity. Specifically, for the axial piston pumps of aircraft, there are actually limited studies and applications. Wang et al. [86] predicted the RUL of one type of

aviation axial piston pump by using Wiener process, in which the return oil flow was proposed as health indicator. Li et al. [87] proposed an adaptive-order particle filter method for the prediction and an empirical grey model was used as the system model. Shi et al. [88] focused on an EHA pump and conducted the prediction using particle filter (PF), in which wear of slipper/swashplate pair was the main degradation mechanism. Li et al. [89] introduced a novel method for extracting degradation features from vibration signals. Xu et al. [90] did a simulation of prediction based on return oil flow and calculated wear life based on Archard model. These methods are either based on some restrictive assumptions or using simplified models.

According to the fact that the sample size of an aviation piston pump is very small, a data-driven method would not be a good choice for life prediction. Among model-based methods, PF has shown great advantages as an efficient prognostics tool in handling the uncertainty and noise affecting measurements [91]. A dual-particle-filter method was used to estimate the state of charge for power Li-ion batteries[92]. To address the particle impoverishment problem, a modified particle filter, named intelligent particle filter (IPF), was proposed by Yin and Zhu [93]. Miao et al. [94] introduced an improved PF algorithm – unscented particle filter (UPF) into battery RUL prediction, and the analytical results showed that UPF could predict the actual RUL with an error less than 5%. Enrico et al. [95-98] improved the method a lot by applying PF functions in different degrading systems, and the framework to estimate the RUL of nonlinear components provides ideas for the prognosis of pump systems. However, to adopt the method, a degrading model should be built. Some parts of a piston pump has been modeled like a friction mechanism model of oil between the valve plate and the cylinder block in axial piston pumps [1] and a wear mechanism model of friction pairs [62] while a physical model that can be used for prediction has not been proposed[99, 100]. For a system that is difficult to be modeled, an empirical model or a model built according to historical data is used to describe the degrading process. Fagogenis et al. [101] proposed an auto-regressive (AR) model with an RUS boost classifier, and a CMAPSS dataset provided by the NASA AMES research center was used to verify the performance of computing the RUL of turbofan engines. A gray prognostic model based

on the Markov process was used for a gas turbine compressor's state estimation [102]. These kinds of models compromise the merits of data-driven models and have less demand in data quantity.

1.4 Overview of the developed method

Figure. 2 provides an overview of the research developed in the Ph.D. thesis, which includes modeling of abrasive debris generation, monitoring abrasive debris online and matching the model and data for remaining wear life prediction. These will be introduced in the following paragraphs and, then, described in more details in the following Sections.

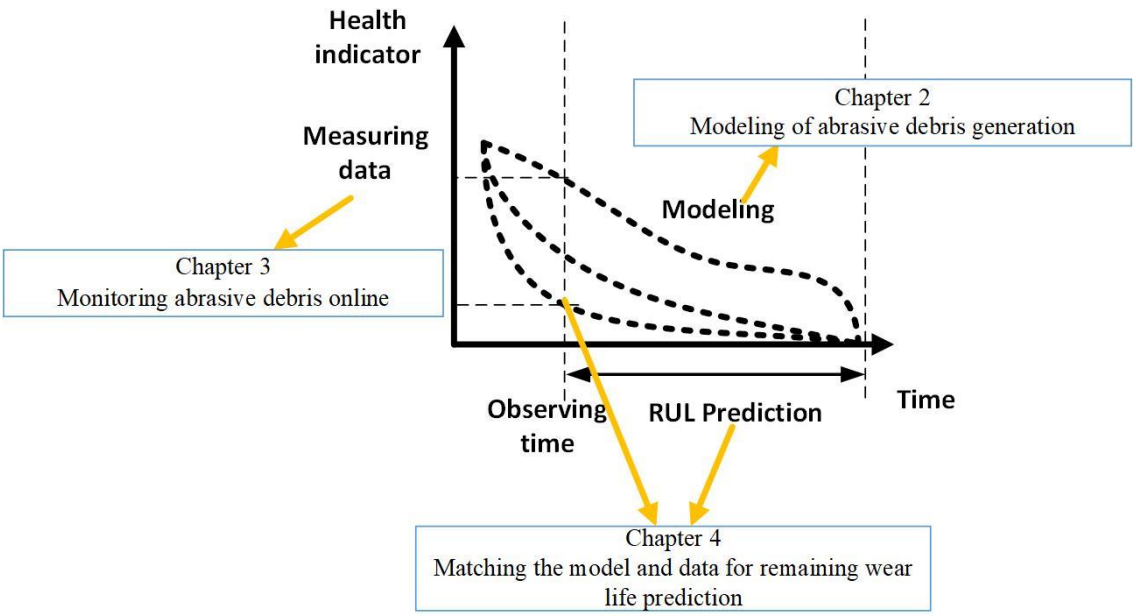

Figure. 2 Framework of the developed method

1.4.1 Modeling of abrasive debris generation

A mesoscale abrasive debris generation model is proposed to solve the wear process of a certain rough surface with given roughness and external work stress, and the statistical results of the numerical model is collected as the characteristic degradation model of the wear process. Under mixed lubrication condition, the contact stress and subsurface stress of rough sliding friction with elastic materials are calculated by boundary element method. Due to the large range of size of abrasive debris and limited computational ability, the solution scale can be set according to the concerning scale.

1.4.2 Monitoring abrasive debris online

When the abrasive debris sensor based on electromagnetic induction principle is utilized to detect high-concentration abrasive debris in high-throughput hydraulic oil, the output induced voltage will be superimposed due to the small clearance of abrasive debris particles, which will reduce the accuracy in judging the number and size of abrasive particles and other characteristics. Aiming at solving the problem of aliasing signals of abrasive debris particles, a degenerate unmixing estimation method for separating aliasing signals is proposed. Since at the same time, the number of the debris particles may be greater than the number of sensors, based on the underdetermined blind source separation method and series sensor structure, the presented aliasing signal separation method can effectively improve the detection accuracy which provides the basis for the life prediction.

1.4.3 Matching the model and data for remaining wear life prediction

The system degradation model based on numerical method and the detection data based on aliasing signal separation method may be accompanied by uncertainties, which will lead to the inaccurate matching of the model and data. In this paper, the uncertainties are characterized as model uncertainty and measurement uncertainty, and the wear state estimation method based on adaptive order particle filter is proposed. When using data of different lengths for short-term prediction and long-term prediction, the model is adaptive to match the optimal order, and the relatively accurate state estimation is obtained. Combined with the numerical degradation model of mesoscale abrasive generation, the separation method for aliasing signals and the wear state estimation method of adaptive order particle filter, a remaining wear life prediction method of hydraulic pump based on monitoring abrasive particles is proposed.

1.5 Thesis Structure

Figure. 3 shows the structure of the thesis work. Chapters 2, 3 and 4 are dedicated to the research objectives introduced in Section 1.4 and, Chapter 5 draws the conclusions and future perspectives. At the end, a collection of the international peer-reviewed journals papers finalized during the Ph.D. is included for further details.

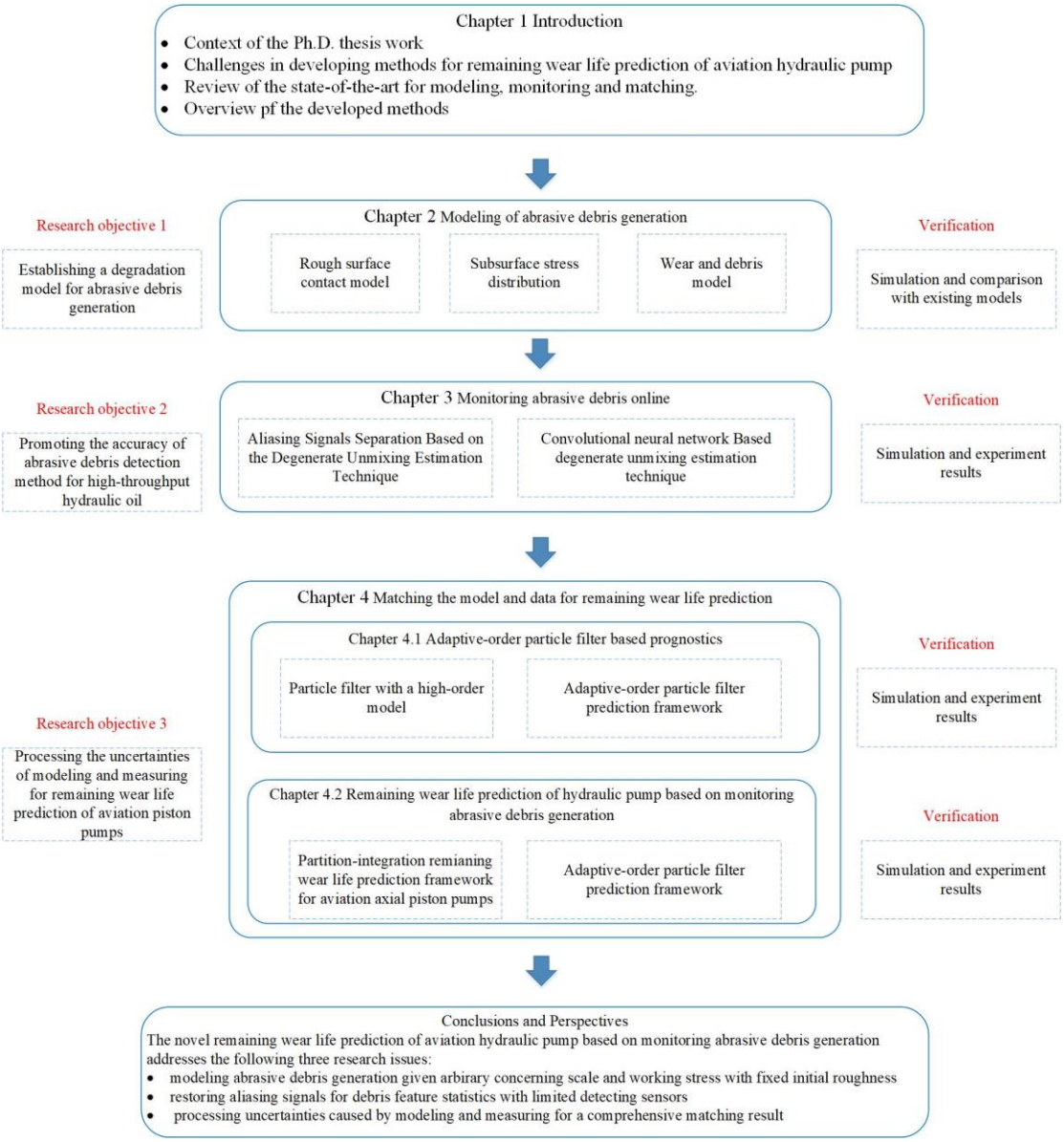

Figure. 3 Sketch of the thesis structure

SECTION II. DETAILS OF THE DEVELOPED METHOD

This Section consists in 3 Chapters (i.e., Chapters 2 Degradation paths modeling method, Chapter 3 Measuring accuracy promoting method, Chapter 4 Current state estimating method, and Chapter 5 Conclusions and future perspectives) that describe in details the original contributions resulting from the Ph.D. research work.

.

2. Modeling of abrasive debris generation

Contents of the Chapter have been adapted from:

1[J] Tongyang Li, Jian Shi, Shaoping Wang, Enrico Zio and Zhonghai Ma. Mesoscale Numerical Modeling for Predicting Wear Debris Generation[J]. Tribology Letters, 2019, 67(2): 38.

3[C] Tongyang Li, Shaoping Wang, Jian Shi and Enrico Zio. Mechanical Wear Life Prediction Based on Abrasive Debris Generation [C], 2019 Prognostics and System Health Management Conference (PHM 2019).

Wear debris has become a powerful indicator for wear conditions monitoring of engineering machines. However, there is still a lack of effective method for predicting the generation of wear debris with given rough surfaces. We developed a numerical model based on atomic attrition mechanism for abrasive debris generation modeling. The modeling approaches including rough contact model, subsurface stress distribution and debris generation model are given in Section 2.1. The numerical prediction procedure is presented by a case study and results are compared with existing models quantitatively or qualitatively in Section 2.2. Then in Section 2.3, some conclusions are drawn.

2.1 Modeling approaches

2.1.1 Rough contact model

At debris level, the contact surfaces are rough surfaces instead of macroscopically smooth surfaces. The load is applied on real contact area instead of apparent contact area. Practically, profilometry techniques, such as AFM and White Light Interferometry (WLI) is used to give out real surface profile [103]. However, when the diameter of the

stylus is larger than the distance of two grooves, an error unavoidably appears. For the rough surface modeling, there is no general agreement, so a Fourier based digital filter [104] is used to generate artificial isotropic rough surfaces with Gaussian height distribution. According to Greenwood and Tripp's theory [105], the contact of two rough surfaces can be regarded as an equivalent rough surface with a smooth flat plane. Then, the problem is described as a discrete contact model that a grid can be set to describe both surfaces. Node (i, j) denotes the node at row i and column j of the grid. Suppose that an external applied load P_0 is conducted, a load balance should be satisfied

$$P_0 = \int_{\Gamma_c} p_{i,j} \mathrm{d}\Gamma \tag{2-1}$$

where Γ_c is the real contact area and $p_{i,j}$ is the contact pressure at node (i, j). $u_{i,j}$ is the total deformation of both surfaces at node (i, j).

$$u_{i,j} = \sum_{k=0}^{M_x-1} \sum_{l=0}^{M_y-1} K_{i-k,j-l} p_{k,l}, 0 \le i < M_x, 0 \le j < M_y \tag{2-2}$$

where M_x and M_y are the amount of rows and columns of the grid. Note that $K_{i-k,j-l}$ is the coefficient and its solution on an elastic half-space can be obtained by

$$K_{i-k,j-l} = \frac{1}{\pi E^*} \int_{x_k-\frac{1}{2}a_x}^{x_k+\frac{1}{2}a_x} \int_{y_l-\frac{1}{2}a_y}^{y_l+\frac{1}{2}a_y} \frac{dxdy}{\sqrt{(x_i - x_k)^2 + (y_i - y_k)^2}} \tag{2-3}$$

where a_x and a_y are the grid spaces of rows and columns. The E^* is the composite Young's Modulus, which can be calculated by

$$\frac{1}{E^*} = \frac{1-\nu_1^2}{E_1} + \frac{1-\nu_2^2}{E_2} \tag{2-4}$$

where ν_1 and ν_2 are the Poisson's ratios of the two surfaces. E_1 and E_2 are the Young's Modulus of the two surfaces. Within the framework of Hertz's hypotheses, the real contact pressure $p_{i,j}$ and the corresponding deformation $u_{i,j}$ on each node can be

obtained by solving

$$\begin{cases} h_{i,j} = u_0 + u_{i,j}, (i,j) \in \Gamma_c \\ p_{i,j} > 0, (i,j) \in \Gamma_c \\ h_{i,j} \le u_0 + u_{i,j}, (i,j) \notin \Gamma_c \\ p_{i,j} = 0, (i,j) \notin \Gamma_c \\ P_0 = a_x a_y \sum_{i=0}^{M_x-1} \sum_{j=0}^{M_y-1} p_{i,j} \end{cases} \tag{2-5}$$

where u_0 is the surface deflection and $h_{i,j}$ is the separation at node (i, j) of the two surfaces when there is no load. The single-loop CGM and multi-level multi-summation (MLMS) method proposed by Polonsky and Keer [46] is employed to solve the problem. Note that some small errors of the method was revised by Allwood [45]. Then, the real contact pressure $p_{i,j}$ can be used to get subsurface stress.

2.1.2 Subsurface stress distribution

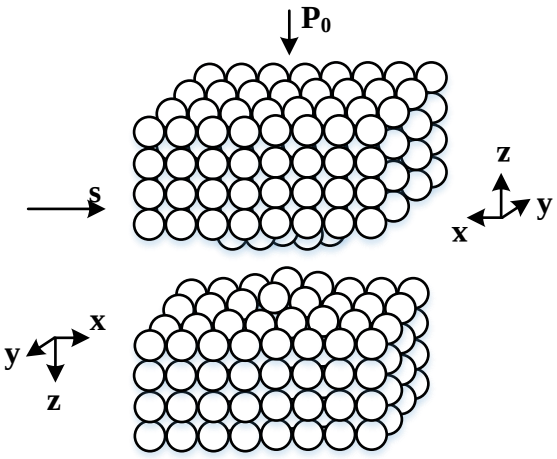

Figure. 4 Coordinate system of two contact surfaces.

Based on Green's function [106], the elastic half-space can be described as a Boussinesq problem. Suppose that the z direction is perpendicular to the x-y plane as is shown in Figure. 4. Each sphere in the figure stands for a minimum removable particle under a given solution. The discretized formation of Green's function can be expressed as

$$\sigma_{qr}(x_i, y_j, z_m) = \sum_{k=0}^{M_x-1}\sum_{l=0}^{M_y-1}(p_{k,l}D_{qr}^{N}(x_i - x_k, y_j - y_l, z_m) + s_{k,l}D_{qr}^{S}(x_i - x_k, y_j - y_l, z_m)),$$
$$q, r = x, y, \text{or } z \tag{2-6}$$

where $\sigma_{qr}(x_i, y_j, z_m)$ is the stress at node (i, j, m), $p_{k,l}$ is the normal pressure and $s_{k,l}$ is the shear traction at node $(k, l, 0)$. $D_{qr}^{N}(x_i - x_k, y_j - y_l, z_m)$ and $D_{qr}^{S}(x_i - x_k, y_j - y_l, z_m)$ are the influence coefficients of normal pressure and shear traction, respectively. Liu and Wang [107] proposed the discretized formation of the influence coefficients:

$$\begin{aligned} D_{qr}^{N}(x_i - x_k, y_j - y_l, z_m) = \frac{1}{2\pi}(&T_{qr}^{N}(x_i - x_k + \frac{1}{2}a_x, y_j - y_l + \frac{1}{2}a_y, z_m) + \\ &T_{qr}^{N}(x_i - x_k - \frac{1}{2}a_x, y_j - y_l - \frac{1}{2}a_y, z_m) - \\ &T_{qr}^{N}(x_i - x_k - \frac{1}{2}a_x, y_j - y_l + \frac{1}{2}a_y, z_m) - \\ &T_{qr}^{N}(x_i - x_k + \frac{1}{2}a_x, y_j - y_l - \frac{1}{2}a_y, z_m)) \end{aligned} \tag{2-7}$$

Note that the influence coefficients of shear traction have the same formation with that of normal pressure after replacing the subscript N by S. The analytical solution of function T^N and T^S is:

$$\begin{cases} T_{xx}^{N}(x, y, z) = -2\nu\tan^{-1}\dfrac{xy}{Rz} + 2(1-2\nu)\tan^{-1}\dfrac{x}{R+y+z} - \dfrac{xz}{R(R+y)} \\ T_{yy}^{N}(x, y, z) = T_{xx}^{N}(y, x, z) \\ T_{zz}^{N}(x, y, z) = -\tan^{-1}\dfrac{xy}{Rz} + \dfrac{xz}{R(R+y)} + \dfrac{yz}{R(R+x)} \\ T_{xy}^{N}(x, y, z) = (2\nu-1)\ln(R+z) - \dfrac{z}{R} \\ T_{xz}^{N}(x, y, z) = -\dfrac{z^2}{R(R+y)} \\ T_{yz}^{N}(x, y, z) = -\dfrac{z^2}{R(R+x)} \end{cases} \tag{2-8}$$

$$\begin{cases} T_{xx}^{S}(x,y,z) = -2\ln(R+y) + z(1-2\nu)\left[\dfrac{y}{R(R+z)} + \dfrac{z}{R(R+y)}\right] - \dfrac{2\nu x^2}{R(R+y)} \\ T_{yy}^{S}(x,y,z) = 2\nu\ln(R+y) - z(1-2\nu)\dfrac{y}{R(R+z)} - \dfrac{2\nu y}{R} \\ T_{zz}^{S}(x,y,z) = -\dfrac{z^2}{R(R+y)} \\ T_{xy}^{S}(x,y,z) = \ln(x+R) - z(1-2\nu)\dfrac{x}{R(R+z)} - \dfrac{2\nu x}{R} \\ T_{xz}^{S}(x,y,z) = -\dfrac{xz}{R(R+y)} - \tan^{-1}\dfrac{xy}{Rz} \\ T_{yz}^{S}(x,y,z) = \dfrac{z}{R} \end{cases} \tag{2-9}$$

where $R=\sqrt{x^2+y^2+z^2}$. By substituting Eq. (2-8) and Eq. (2-9) into Eq. (2-7), the influence coefficients of normal pressure and shear traction can be obtained. Substituting Eq. (2-7) into Eq. (2-6), the subsurface stress at arbitrary given node can be obtained and the corresponding Von Mises stress can be calculated:

$$\sigma_{VM} = \frac{1}{\sqrt{2}}\sqrt{(\sigma_{xx}-\sigma_{yy})^2 + (\sigma_{xx}-\sigma_{yy})^2 + (\sigma_{xx}-\sigma_{yy})^2 + 6(\sigma_{xy}^2+\sigma_{yz}^2+\sigma_{xz}^2)} \tag{2-10}$$

2.1.3 Wear and debris model

At the macroscale level, Archard wear equation is commonly used to predict the total material loss during the wear process. At microscale level, the wear volume is the summation of the atoms. The proposed model is based on the atomic attrition mechanism. The minimum removable unit consists of a wear debris particle in mesoscopic scale. The accurate description of the generation of wear debris is the key to the prediction of wear. The debris generates when the material fails. Under a specific applied load, the fracture criterion of different materials may be various. The classic Hertz's theory states that when the stress exceeds approximate three times of the yield stress, there will be a plastic deformation. According to Akchurin's result [48], a Von

Mises stress based failure criterion shows a good agreement with the AFM experimental data. The wear model is given in a numerical way: supposing that the surface and subsurface stress have been accurately calculated by the aforementioned method, the Von Mises stress at each node (i, j, k) can be obtained by Eq. (2-10). At arbitrary time T, the potential removal set $S_p(t)$ is

$$S_p(t) = \left\{(i, j, k) \mid \sigma_{VM}(x_i, y_j, z_k) > \sigma_{yield}\right\} \tag{2-11}$$

where σ_{yield} is the yield stress. Then, the actual removal set $S_a(t)$ is

$$S_a(t) = \left\{(i, j, k) \mid (i, j, k) \in S_p(t), (i, j, k-1) \in S_a(t), \mathrm{k} > 0\right\} \cup \left\{(i, j, 0) \mid (i, j, 0) \in S_p(t)\right\} \tag{2-12}$$

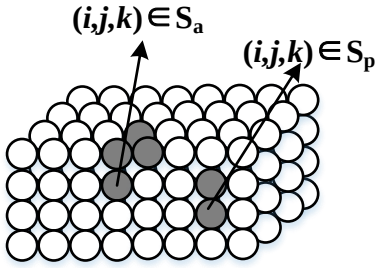

Figure. 5 Schematic diagram of potential removal set and actual removal set.

As is shown in Figure. 5, if the Von Mises stress of a surface node $(i, j, 0)$ exceeds σ_{yield}, the node belongs to the actual removal set. For the subsurface nodes, the node belongs to the actual removal set when all the nodes above it belong to the actual removal set. So there is a fast way in solving the wear process that in a layer-by-layer calculation, not all the subsurface stress, but the nodes whose upper nodes belong to the actual removal set should be calculated, which saves computational cost by approximately 50%~70% (depending on the actual stress distribution).

The nodes in $S_a(t)$ constitute the wear debris at time step t. Figure. 6 shows a simulative results of $S_a(t)$ in which we can see that not all of the nodes are joint together. Some of the joint nodes are marked by solid lines which is recognized as one wear particle. So there may be several wear particles simultaneously. To automatically

finished the recognition process, we define that a wear particle is a node set WP and the following simple algorithm may be used to get all the wear particles:

1.An arbitrary node $(i_0, j_0, k_0) \in S_a(t)$ is moved into WP, then $(i_0, j_0, k_0) \in WP, (i_0, j_0, k_0) \notin S_a(t)$.

2.For $\forall (i, j, k) \in S_a(t)$, if $(i-i_1)^2 + (j-j_1)^2 + (k-k_1)^2 = 1, (i_1, j_1, k_1) \in WP$, (i, j, k) is move into WP. Repeat until $\forall (i, j, k) \in S_a(t), (i-i_1)^2 + (j-j_1)^2 + (k-k_1)^2 \neq 1, (i_1, j_1, k_1) \in WP$.

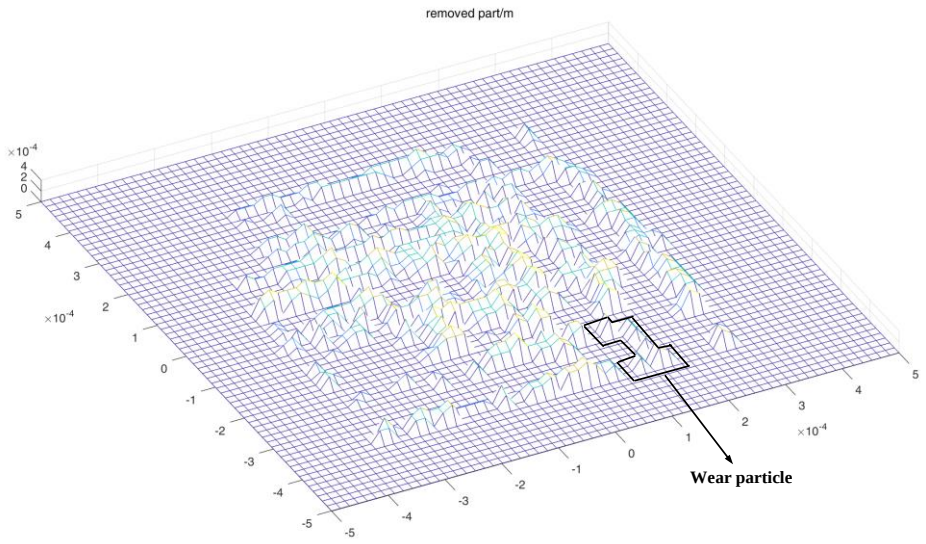

Figure. 6 Schematic diagram of a wear particle.

The volume of each wear particle can be obtained by

$$V_i = N_i \cdot ax \cdot ay \tag{2-13}$$

where N_i is the amount of nodes in WP_i and WP_i is the i_{th} wear particle. Usually, the equivalent diameter of the particle is estimated by

$$D_i = \sqrt[3]{\frac{6V_i}{\pi}} \tag{2-14}$$

By integrating the volume of each wear particle, the wear rate is given by

$$V_w = \sum V_i \tag{2-15}$$

In this model, wear debris generates only due to the contact pressure between rough surfaces. In fact, the fatigue may also cause wear but it is not considered in this work. Besides, we assume that wear debris deviates from surfaces instantaneously and keeps away from the surfaces after generation. So a three-body abrasive wear may not occur under the above assumption. The contact surfaces are updated after each iteration by removing all the wear particles each simulation step. The simulation step is proportional to the sliding distance. Theoretically, the moving distance for each step equals the length of the investigated surface along the moving direction. Because of the flash abrasion assumption, the actual moving distance of each step is larger than the theoretical result. An amplification coefficient may be used to describe the actual moving distance. The amplification coefficient is related to the applied load and friction coefficient but assumed to be a constant in this work.

2.2 Simulation results and discussion

2.2.1 Development of worn surface topography and wear debris

The proposed method can be applied on multiple applications with different scales by setting different research areas. In this case, we mainly focus on the generation of micron-sized wear debris particles which are commonly found in engineering mechanical systems and may cause severe wear. A pair of rough surfaces with initial roughness $80\,\mu m$ is firstly generated. Usually, a smooth convex [46] is added to the rough surface to avoid spurious stress concentration along edges during the simulation process. According to the statistical results [13], most of debris produced by mechanical components range from $50\,\mu m$ to $150\,\mu m$. At the running-in stage, the equivalent debris size of some larger debris may reach $300\,\mu m$ or $500\,\mu m$. The research area is set to cover the aforementioned resolution. As is shown in Figure. 7, one rough surface contains 128×128 data points within a $1\,mm^2$ area. The grid spaces are $ax = ay = 7.8125\mu m$,

which also limits the minimum size of debris particles. Theoretically, the minimum equivalent diameter is about 10.8 μm. It should be noted that the results are strongly dependent on the sampling distance of the rough surfaces [108-111]. Gaussian autocorrelation function may be used to reduce the dependence of surface statistics on the measurement resolution. In this case, the debris whose equivalent diameters are less than 10.8 μm are ignored and believed to have little effect. The values of parameters for the simulation is listed in TABLE 1. Without loss of generality, steel is chosen and the work condition is chosen to be consistent with statistical data.

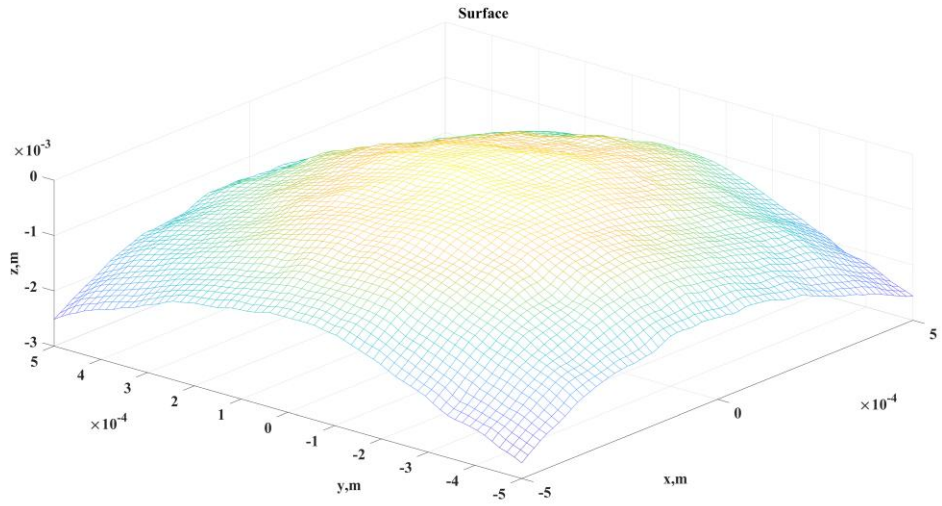

Figure. 7 An artificial surfaces on a smooth convex.

TABLE 1 Values of parameters for simulation

Parameter	Meaning	Value
μ_c	Dry friction coefficient	0.3
v_1	Poisson's ratios of upper surface	0.3
v_2	Poisson's ratios of lower surface	0.3
E_1	Young's Modulus of upper surface	210GPa
E_2	Young's Modulus of lower surface	210GPa
L_x	Length of simulation space in x direction	1mm
L_y	Length of simulation space in y direction	1mm
R_z	Resolution in z direction	7.8125 μm
σ_{yield}	Yield stress of composite surface	355MPa
F_0	Initial normal force	50N

The two rough surfaces are assumed to contact each other initially with normal pressure F_0 applied. The static pressure distribution is calculated by BEM. The initial Hertz contact pressure of the surface is shown in Figure. 8. For the accuracy of the pressure distribution, a statistical result [45] shows that the method generally over-predicts the area of contact by around 0.5% and under-predicts the peak pressure by 0.5% with respect to the test result. The corresponding Mises stress of subsurface is then calculated layer by layer. For each layer, the solving resolution is R_z and the stress in z direction is assumed to be equal. The subsurface Mises stress of the first layer is shown in Figure. 9.

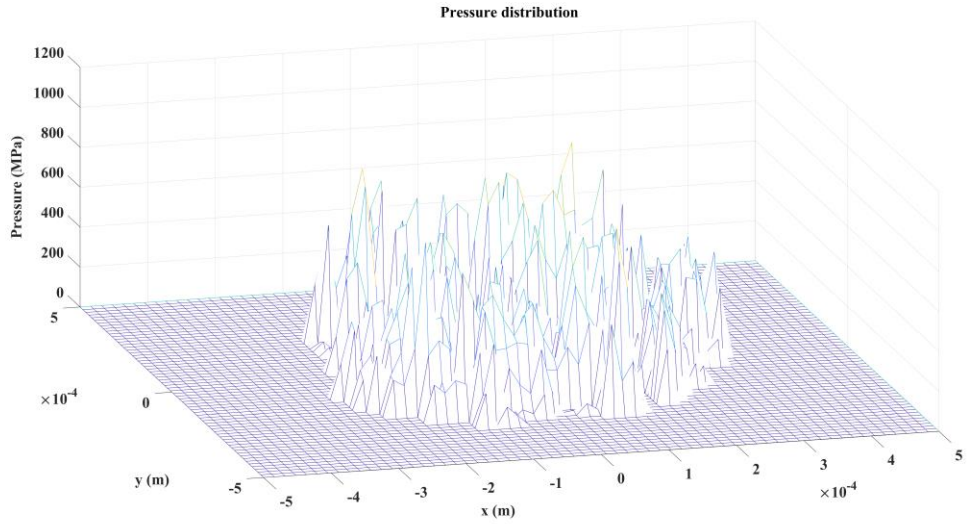

Figure. 8 Contact pressure distribution.

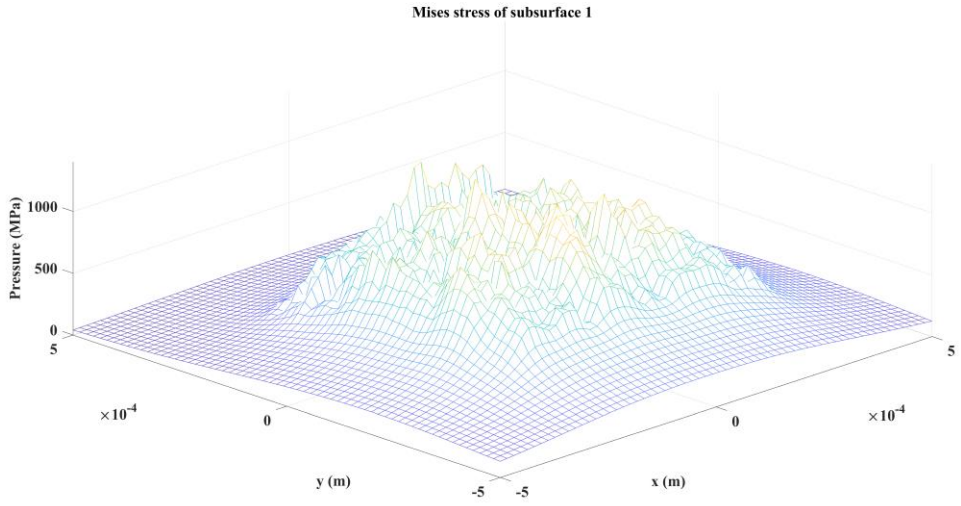

Figure. 9 The subsurface Mises stress of the first layer.

Applying the proposed method onto the surface, a visible wear process can be obtained. As is shown in Figure. 10, after each step, the researched surface profile is updated. From (a) to (i) in Figure. 10, the wear status of the surface becomes more server. The relative roughness which is the current roughness over the initial roughness of the surface is used to evaluate the transformation process as is shown in Figure. 11. The relative roughness decreases, which indicates that the rough surface is smoothened by the wear process. A similar decreasing curve was shown in Spijker's work [36] by using MD at the atomistic scale. Within the 1 mm^2 area, there is a step change at the first

time unit, then the roughness goes down and remains relatively stable at 1.0015, which can be regarded as the running-in stage. If the 1 mm^2 area is a small part of a surface, the closer the contact area is from the edge of the surface, the lower the computational accuracy is, because the coefficient of normal stress by the adjacent surface is related to the distance according to Eq. (2-3). In addition, the spurious stress concentration may also occur which may not be recognized during the Monte Carlo simulation. So the simulation stops when the real contact area covers 80% of the whole surface.

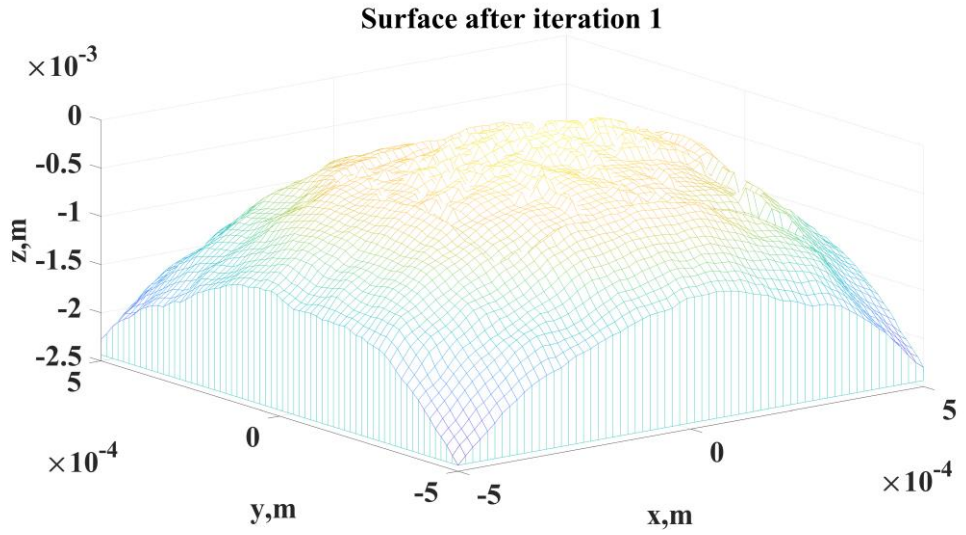

(a)

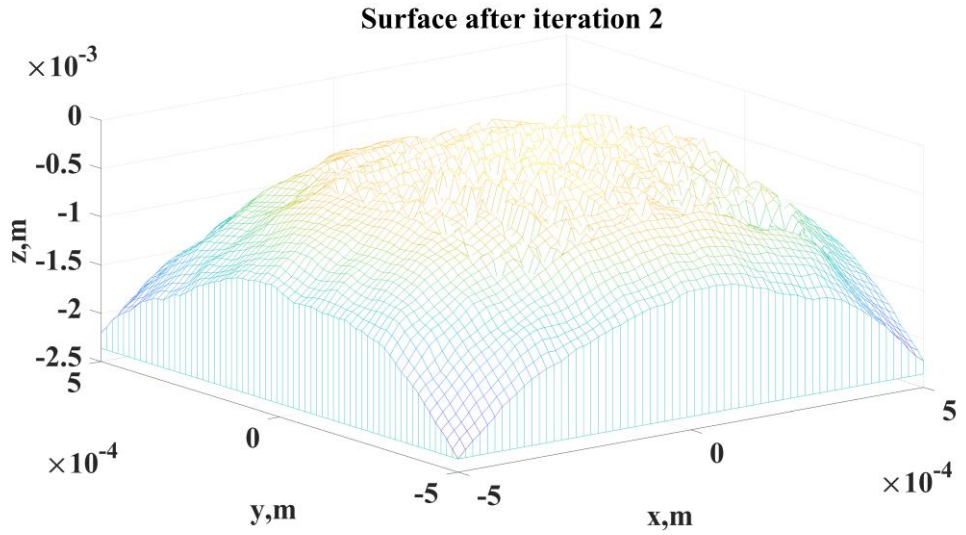

(b)

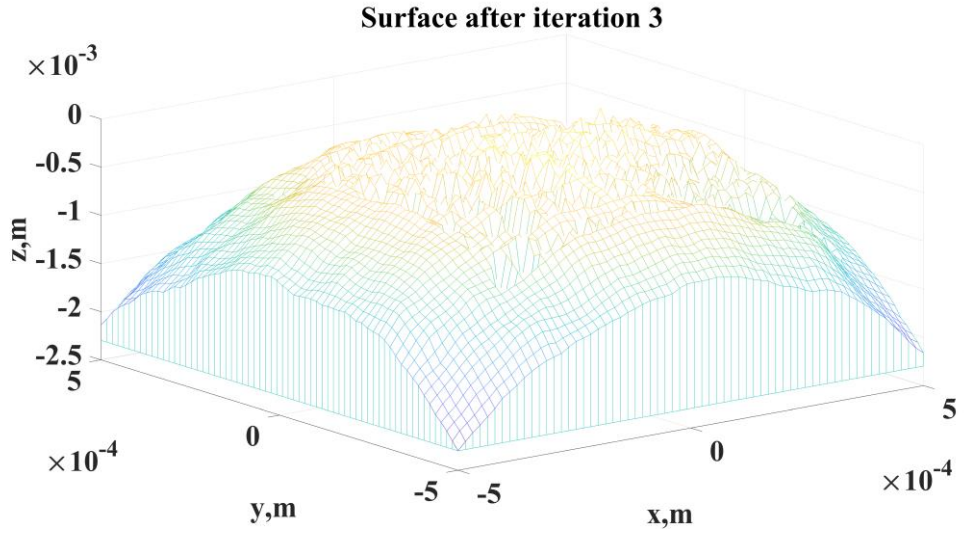
Surface after iteration 3
×10-3
0
-0.5
-1
-1.5
-2
-2.5
z,m
5
0
-5
×10-4
y,m
-5
0
5
×10-4
x,m

(c)

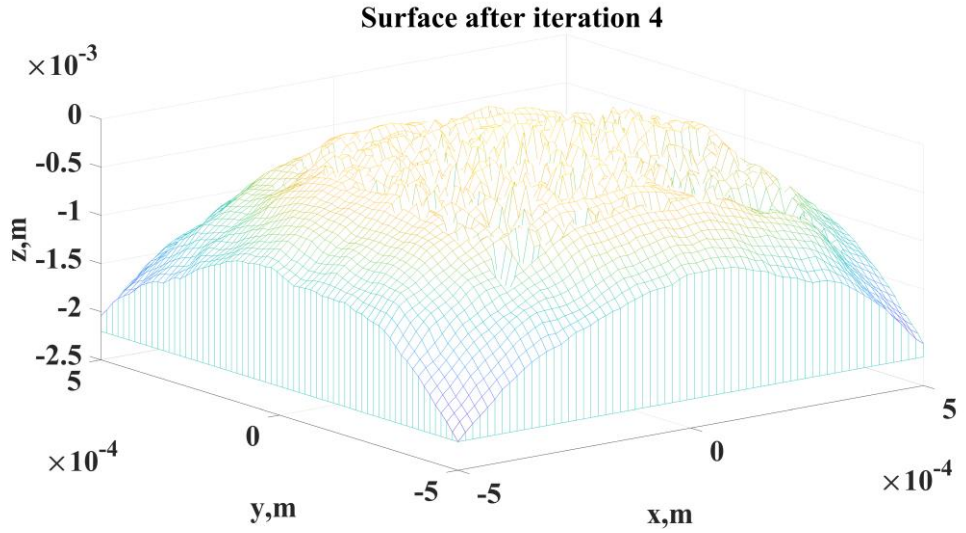
Surface after iteration 4
×10-3
0
-0.5
-1
-1.5
-2
-2.5
z,m
5
0
-5
×10-4
y,m
-5
0
5
×10-4
x,m

(d)

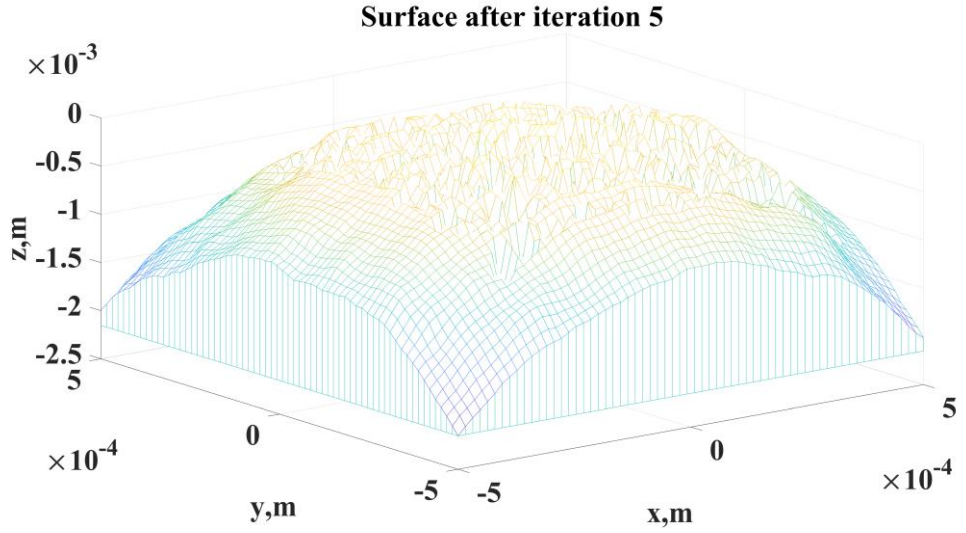
Surface after iteration 5
×10-3
0
-0.5
-1
-1.5
-2
-2.5
z,m
5
0
-5
×10-4
y,m
-5
0
5
×10-4
x,m

(e)

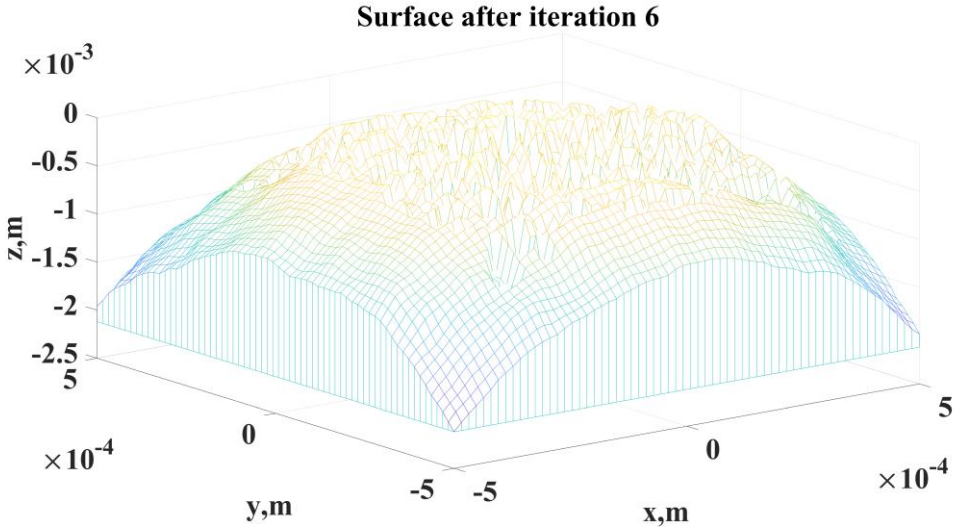
Surface after iteration 6
×10-3
0
-0.5
-1
-1.5
-2
-2.5
z,m
5
0
-5
×10-4
y,m
-5
0
5
×10-4
x,m

(f)

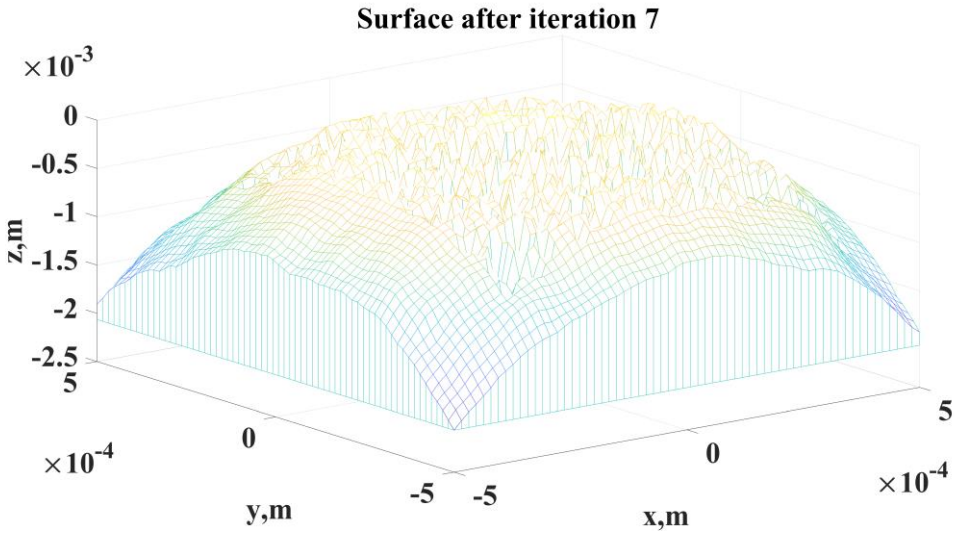
Surface after iteration 7
×10-3
0
-0.5
-1
-1.5
-2
-2.5
z,m
5
0
-5
×10-4
y,m
-5
0
5
×10-4
x,m

(g)

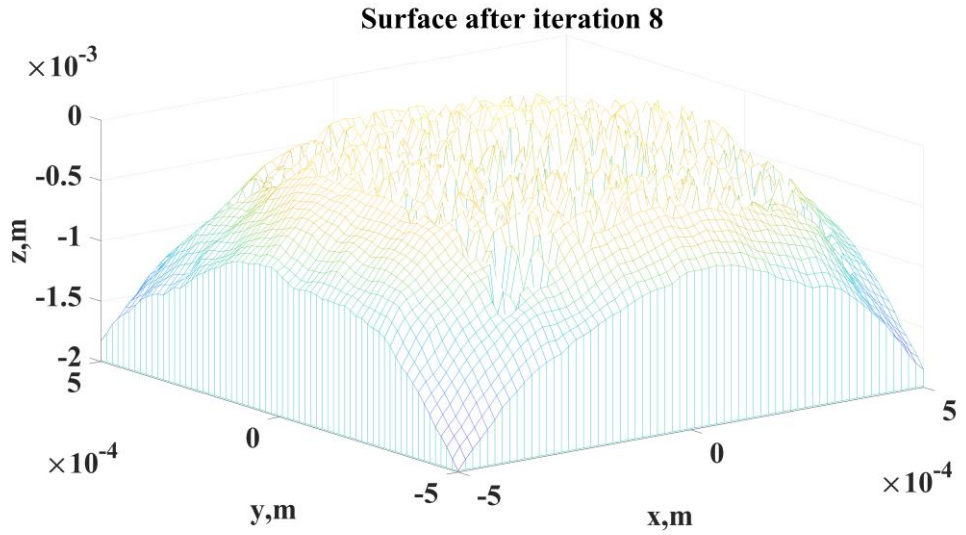

(h)

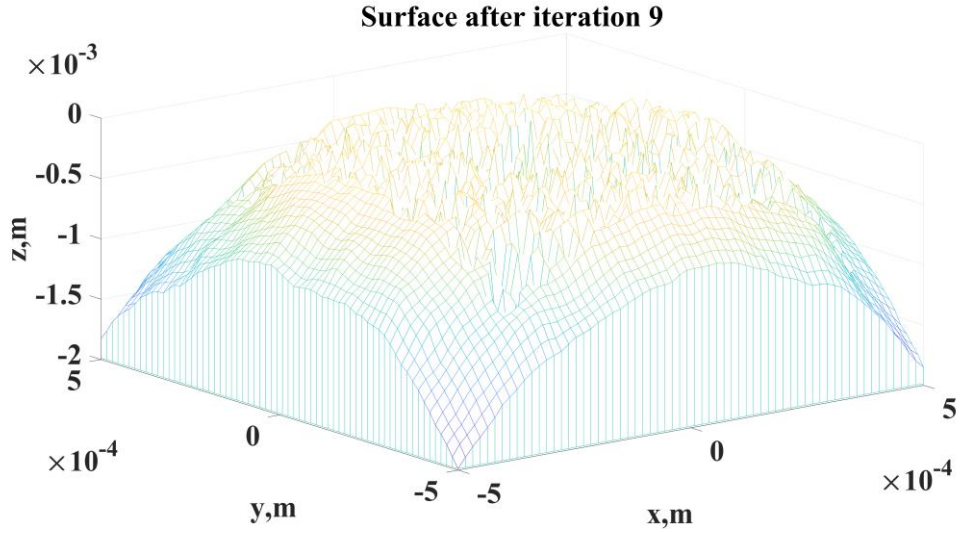

(i)

Figure. 10 Simulation of wear process.

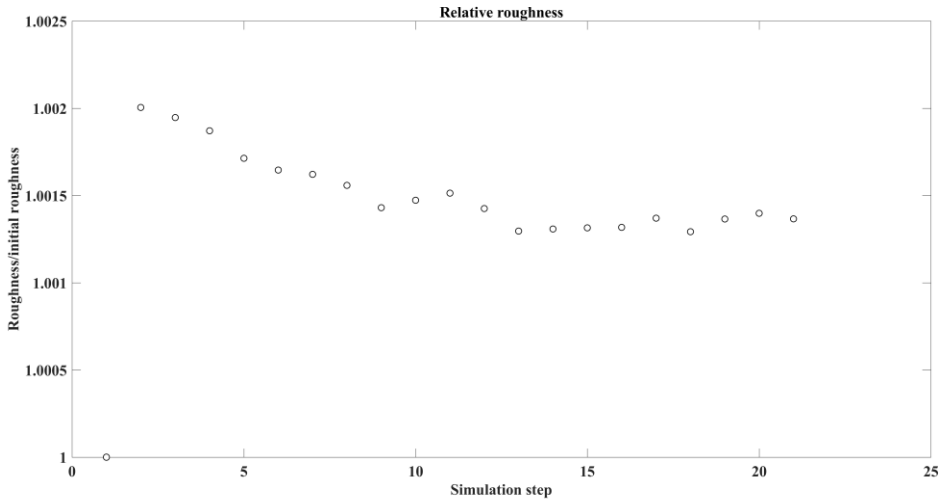

Figure. 11 Relative roughness.

During the wear process, the real contact area increases and the normal stress on each point decreases. For each step, with updating of the surface, wear debris is collected from the removed part. As is shown from Figure. 12 (a) to Figure. 12 (i), some of the removed parts are displayed from which we can see that the topologies of the removed parts change a lot during the process. At the beginning, the removed part can almost be recognized as an entirety. In later simulation, the entirety becomes small particles which means the equivalent debris size decreases. In Figure. 12 (a), the equivalent debris size is about 307 μm and in Figure. 12 (i), the average equivalent debris diameter is 93 μm. However, these values cannot be recognized as a common result for the work condition shown in Figure. 12. The topology of the generated rough surface shows an influence on the wear debris generation.

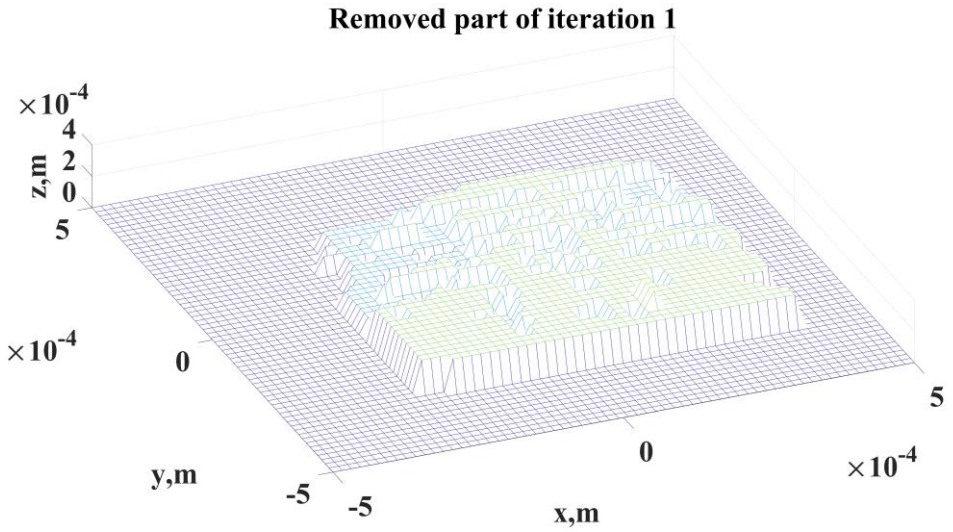
Removed part of iteration 1
×10^-4
4
2
0
z,m
5
0
-5
y,m
-5
0
5
×10^-4
x,m

(a)

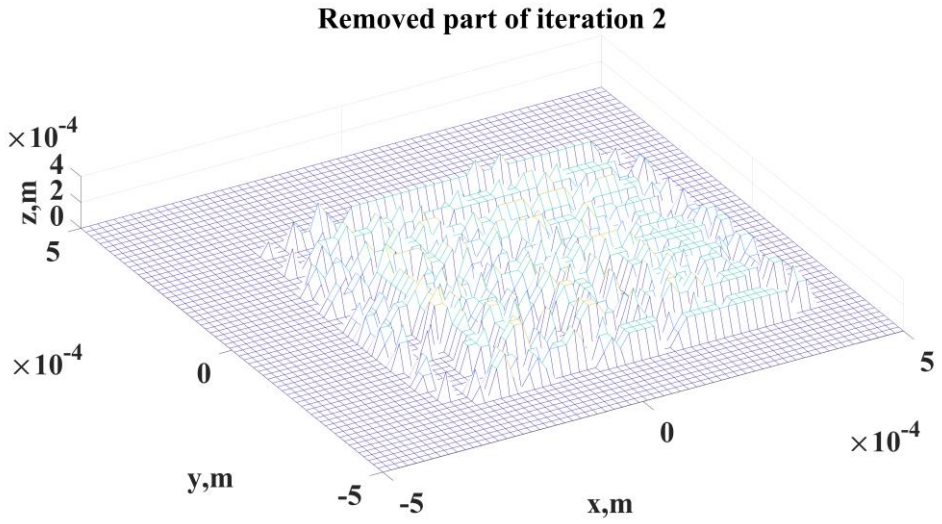
Removed part of iteration 2
×10^-4
4
2
0
z,m
5
0
-5
y,m
-5
0
5
×10^-4
x,m

(b)

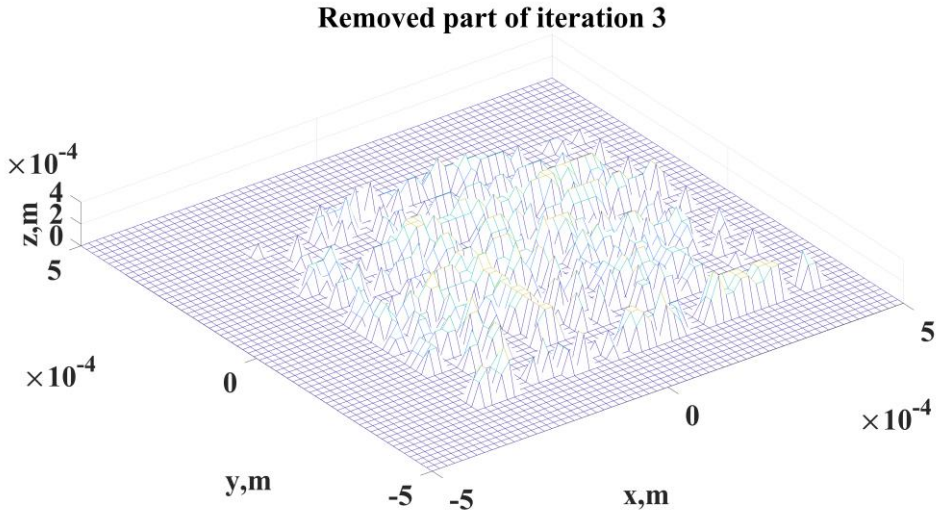
Removed part of iteration 3
×10^-4
4
2
0
z,m
5
0
-5
y,m
-5
0
5
×10^-4
x,m

(c)

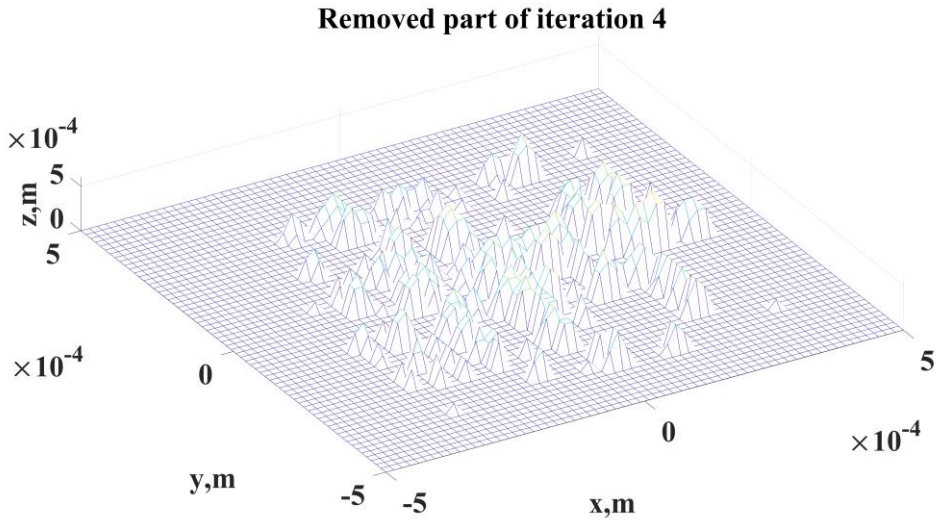
Removed part of iteration 4
×10-4
5
z,m
0
5
×10-4
0
y,m
-5
-5
0
x,m
5
×10-4

(d)

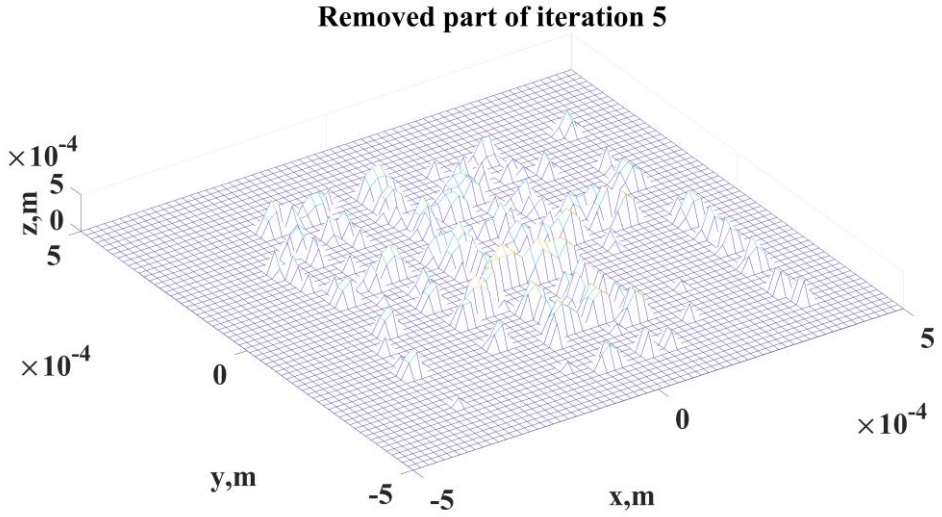
Removed part of iteration 5
×10-4
5
z,m
0
5
×10-4
0
y,m
-5
-5
0
x,m
5
×10-4

(e)

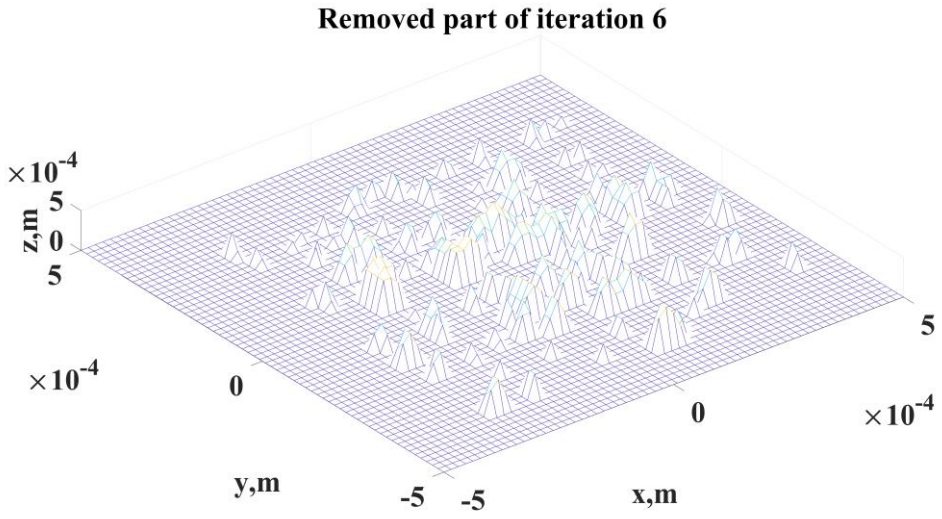
Removed part of iteration 6
×10-4
5
z,m
0
5
×10-4
0
y,m
-5
-5
0
5
×10-4
x,m

(f)

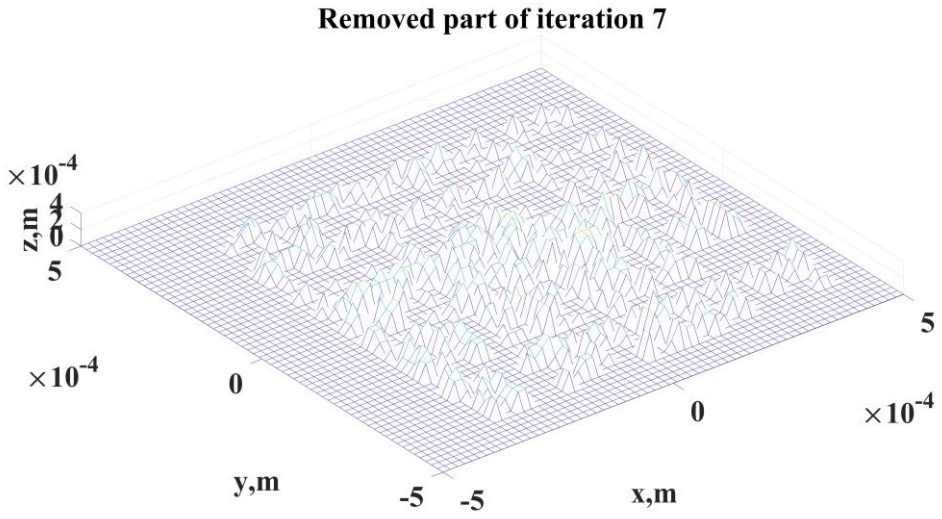
Removed part of iteration 7
×10-4
4
2
z,m
0
5
×10-4
0
y,m
-5
-5
0
5
×10-4
x,m

(g)

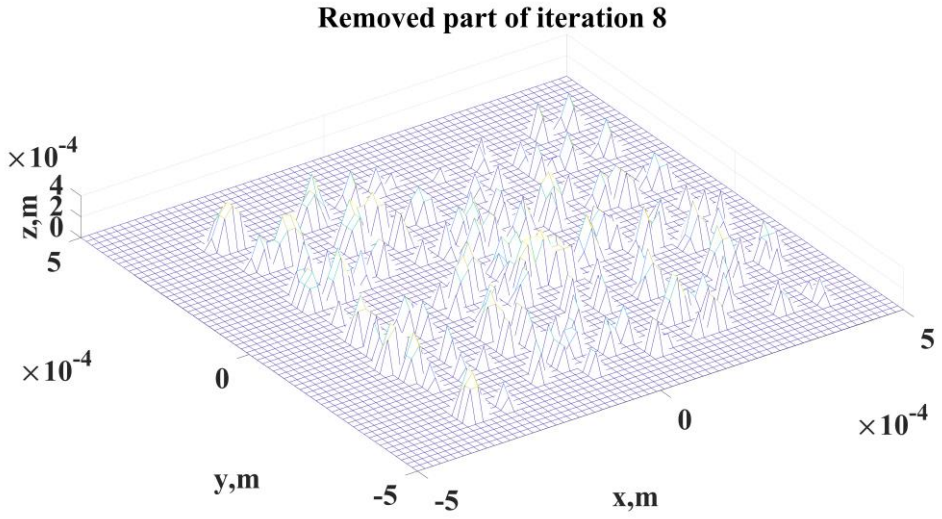
Removed part of iteration 8
×10-4
4
2
z,m
0
5
×10-4
0
y,m
-5
-5
0
5
×10-4
x,m

(h)

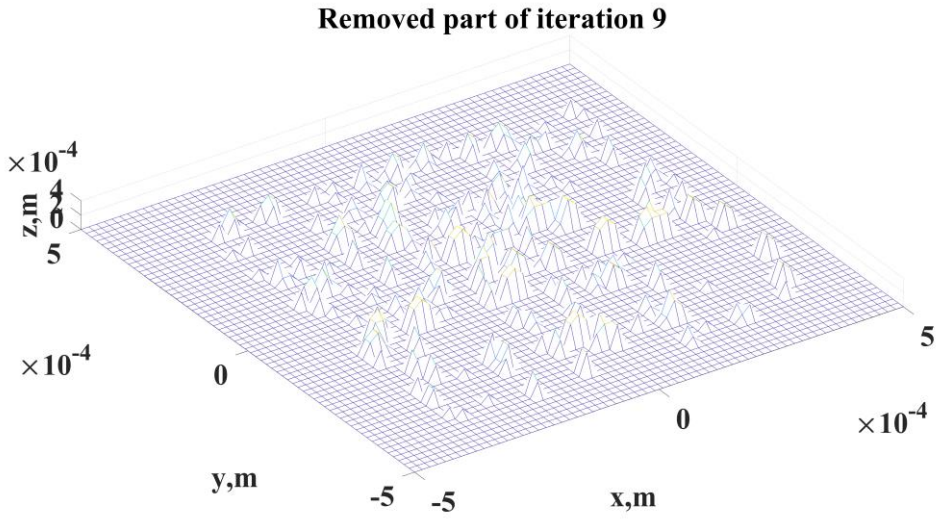

(i)

Figure. 12 Simulation of wear debris.

To avoid the randomness of artificial surfaces, a Monte Carlo simulation is carried out. 100 pairs of generated rough surfaces each with 1 mm^2 area are tested by the proposed method. The roughness of the original surface is controlled from 78 μm to 82 μm. All the rough surfaces are added onto the same convex to get a statistical result. We investigated the wear rate for surfaces with different topologies. The simulation step is proportional to time unit but does not correspond to a practical meaning. Therefore, the cumulative wear volume is used instead of wear rate to describe the wear process. Considering the influences by the applied load, surfaces with same parameters are tested under 50N and 100N. Mean wear volumes with standard deviation bars are shown in Figure. 13. Generally, the wear volume displays a linear function with respect to the simulation step. Total wear volume loss of 10 randomly selected surfaces are also obtained by finite element method and their mean value are also shown in Figure. 13. To make the two method comparable, the amplification coefficient is set to be 0.72. For the predicting result, most of the surfaces show a similar wear rate in the beginning, while the difference becomes evident after about 10 steps. Compared with other surfaces, the roughness of the surface with markedly different wear rate does not display

a difference. So the topology is considered to account for the individual difference. The individual behavior is not an accident. 7 of the 100 pairs of surfaces show non-linear wear rate as well in contrast with major surfaces. In Popov's work [112], Rabinowicz criterion was used and similar inflection point appeared in their curve of wear volume versus sliding distance. Figure. 14 shows changing of real contact areas, which may account for the changes of friction coefficient during the silding. This randomness may give an explanation to the engineering phenomenon that even for the same batch of machines, their degradation paths are various from each other under the same work condition. The average wear volumes per each simulation step of the specimen are approximate $2.135\times10^{-10}\,\mathrm{m}^3$ at 50N and $3.6107\times10^{-10}\mathrm{m}^3$ at 100N .

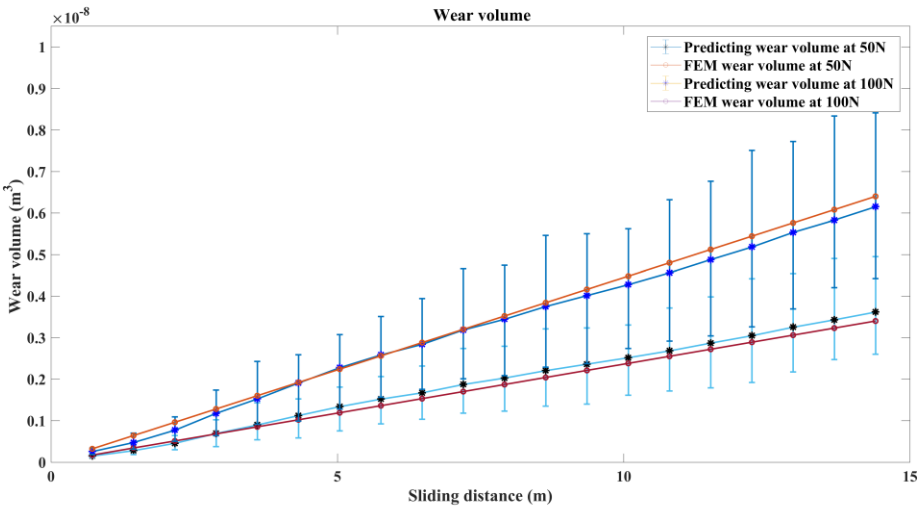

Figure. 13 Wear volume of rough surfaces.

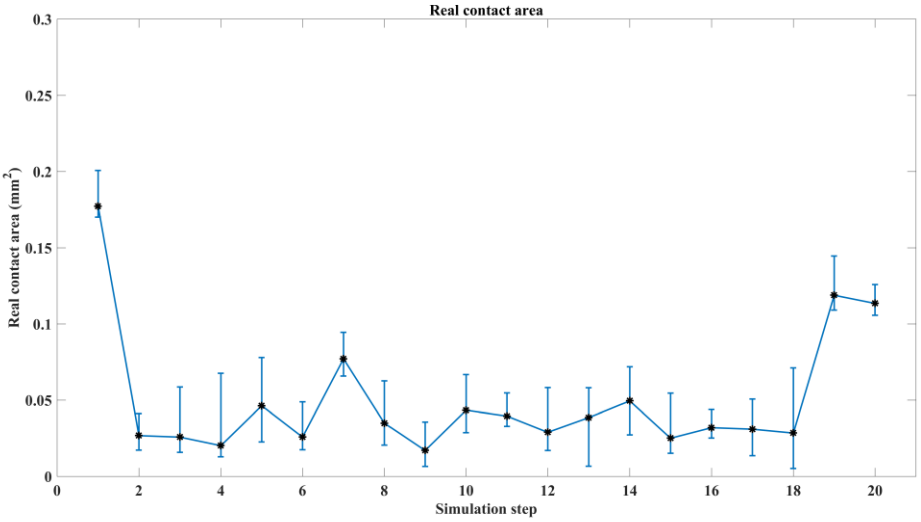

Figure. 14 Real contact area of wear process.

As there is no general understanding on the wear of rough surfaces with random topologies by the experiments and simulation results, the debris characteristics from the statistical results are analyzed. The proposed method takes advantages in providing a simulative information of each particles in detail. Quantity, size, shape and composition are believed to be the key characteristics of wear debris that are related to the wear status of rough surfaces. A common result [113] shown in Figure. 15 displays the qualitative relationship between debris generation and wear process. Wear debris generation rate increases with increasing time. The sizes of wear debris obey different distributions in different wear stages. But in a certain wear stage, the characteristics of wear debris show regularity. A detailed analysis on the characteristics is given out by the following sections.

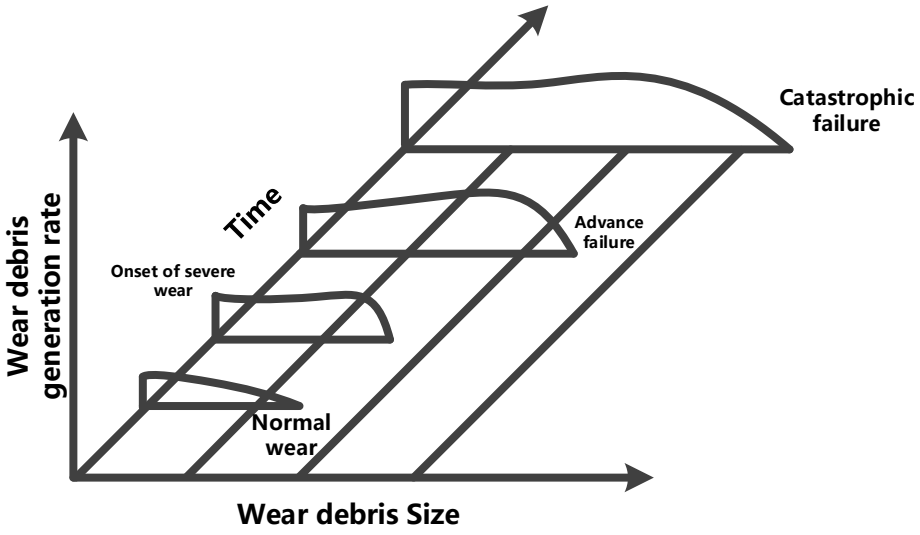

Figure. 15 Relationship between debris generation and wear process.

2.2.2 Quantity of wear debris

With the relative stable wear rate, quantity of wear debris increases as the results shown in Figure. 12. The counts of all the wear particles are shown in Figure. 16. Debris monitoring results by Miller et al. [114] show that in early stages of wear, the counts of wear debris follow a power function with respect to the sliding distance, which is consistent with the simulation result. A dynamic model for predicting debris generation presented by Hong [10] is used as a comparison in this thesis. Fitting curves using power function are plotted in Figure. 16. Since the dynamic model concerns also parameters related to power loss which is simplified by the proposed method, the dynamic model predicts less particles than the proposed method. We should also notice that individual difference still exists. Whether the wear debris counts by a single surface simulation is consistent with experiments needs a further research. The fitting function for the statistical result is

$$f(x) = 41.29x^{1.383} - 70.29 \tag{2-16}$$

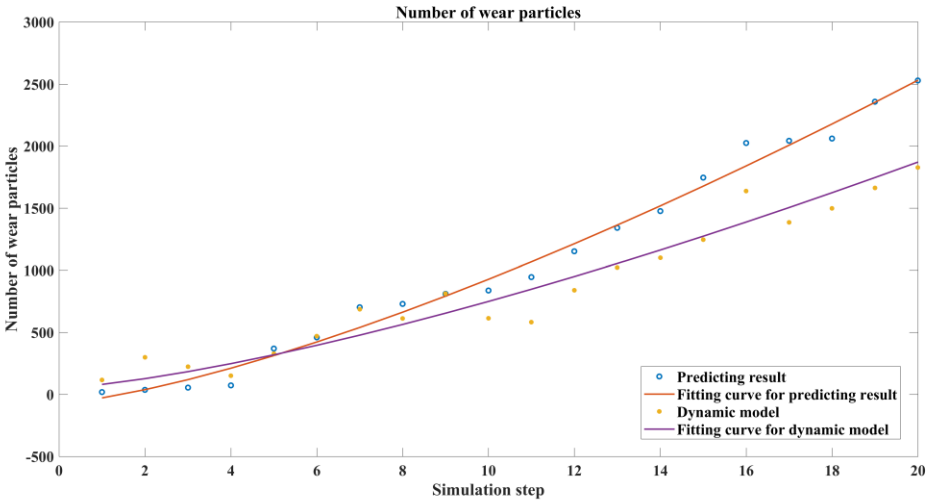

Figure. 16 Counts of wear debris particles.

2.2.3 Size distribution of wear debris

At running-in stage, the relative surface conformity of the rough surfaces increases with increasing simulation duration [115]. With smaller conformity, loads will distribute unevenly which will lead to a larger probability of large wear debris. Because the very large debris may not appear considering the three-body abrasion in practice, only debris particles whose equivalent diameters are within 500 μm are counted into the statistical data. It is suggested that Weibull distribution may be used to fit the debris distribution [116, 117]. Several studies also found that their experiment results obeyed Weibull distribution [17, 118, 119]. The size distribution of wear debris generated by the 100 pairs of surfaces is shown in Figure. 17. Experiments with same parameters shown in Figure. 18 was conduction by Akchurin et al. [48, 49] but in a much smaller scale. They got a similar shaped distribution by AFM measurements. Similar distribution was found in Catelas's metal–metal hip testing [120]. The mean value is 178.52 μm for the Weibull distribution which is given by

$$f(x)=\frac{2.718}{200.698}\left(\frac{x}{200.698}\right)^{1.718} e^{-\left(\frac{x}{200.698}\right)^{2.718}} \tag{2-17}$$

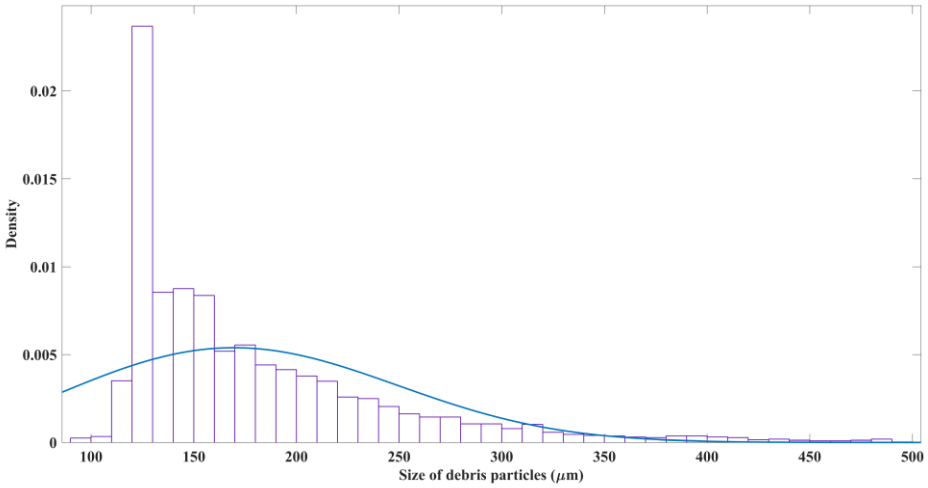

Figure. 17 Size distribution of wear debris.

The distribution results of simulation step 2 to simulation step 9 are shown in Figure. 18. The size bin is established for every 10 μm. The fitting distribution matches the statistical data well for the first two steps. From step 4, the amount of specimens shows a dramatic increasing around 120 μm and the peak appears sustainably. This peak actually cannot be represented by the suggested Weibull distribution. Same phenomenon occurs in Akchurin's research. This may be ascribed to the coarse size bin which is used for the particle recognition, since the simulative resolution of wear particles is not very high considering the large computational costs. A highly refined size bin may reduce the fit error.

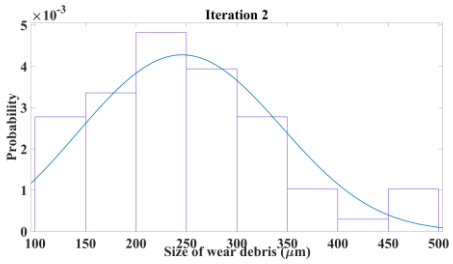

(a)

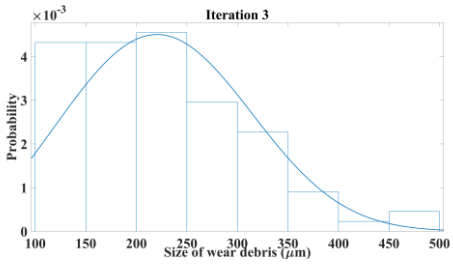

(b)

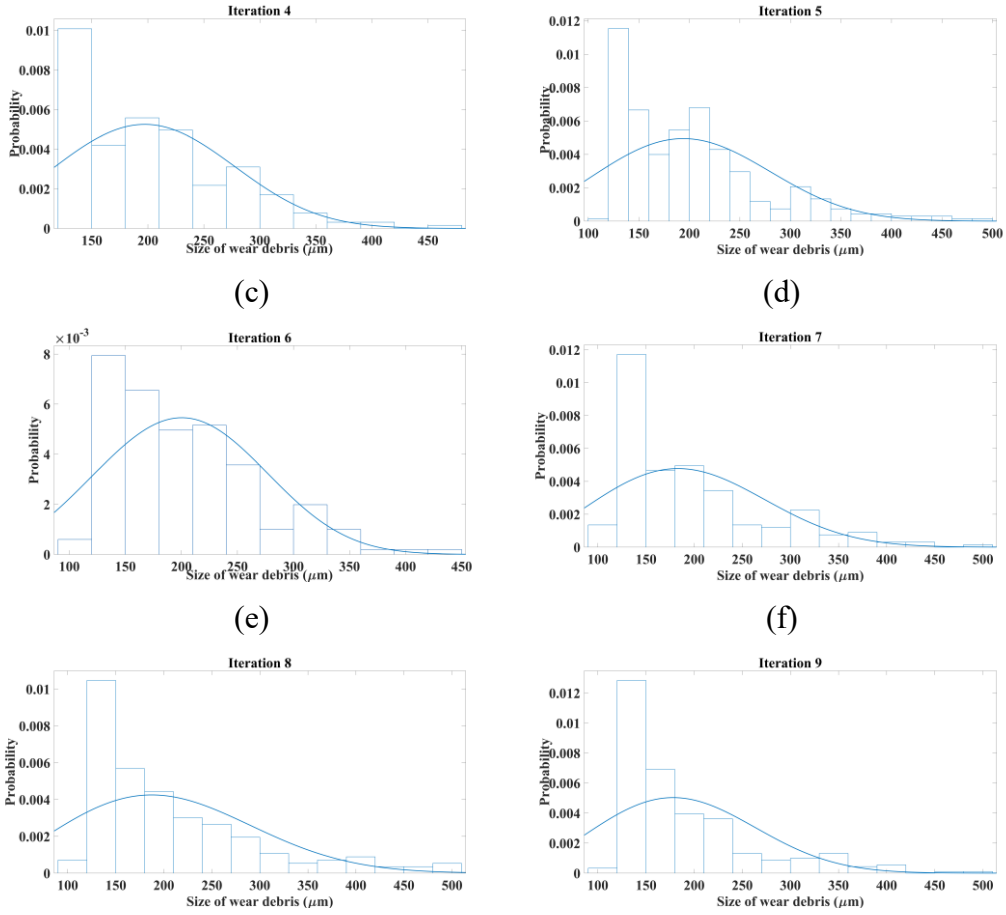

Figure. 18 Distribution results of wear debris size in each iteration.

2.2.4 Shape of wear debris

The shape of wear debris is usually qualitatively evaluated because of the expensive cost by microscopy methods. Several indicators like area, length, convexity and elongation were investigated to establish the relationship with wear mechanisms and severity, among which aspect ratio [121] that denotes the ratio of the largest diameter of the particle to the largest perpendicular diameter is regarded as a more effective one [14, 122]. The result of the Monte Carlo simulation is shown in Figure. 19. Actually, only 0.3% of all the data drop into the field of larger than 13. To avoid the influence of very thin particles which is seldom seen in matallic debris and may not exist if we take reentering into consideration, only data with aspect ratio smaller than

13 is shown. From Figure. 19 (a) to Figure. 19 (g), the results of simulation step 2 to simulation step 9 are displayed in order. In the beginning, the debris particles with low aspect ratio takes 53%, as is shown in Figure. 19 (a), which means ball-like particles account for major percentage. The difference between the particles with low aspect ratio and that with high aspect ratio becomes smaller with simulatioin duration. The aspect ratios are close to a uniform distribution at step 9.

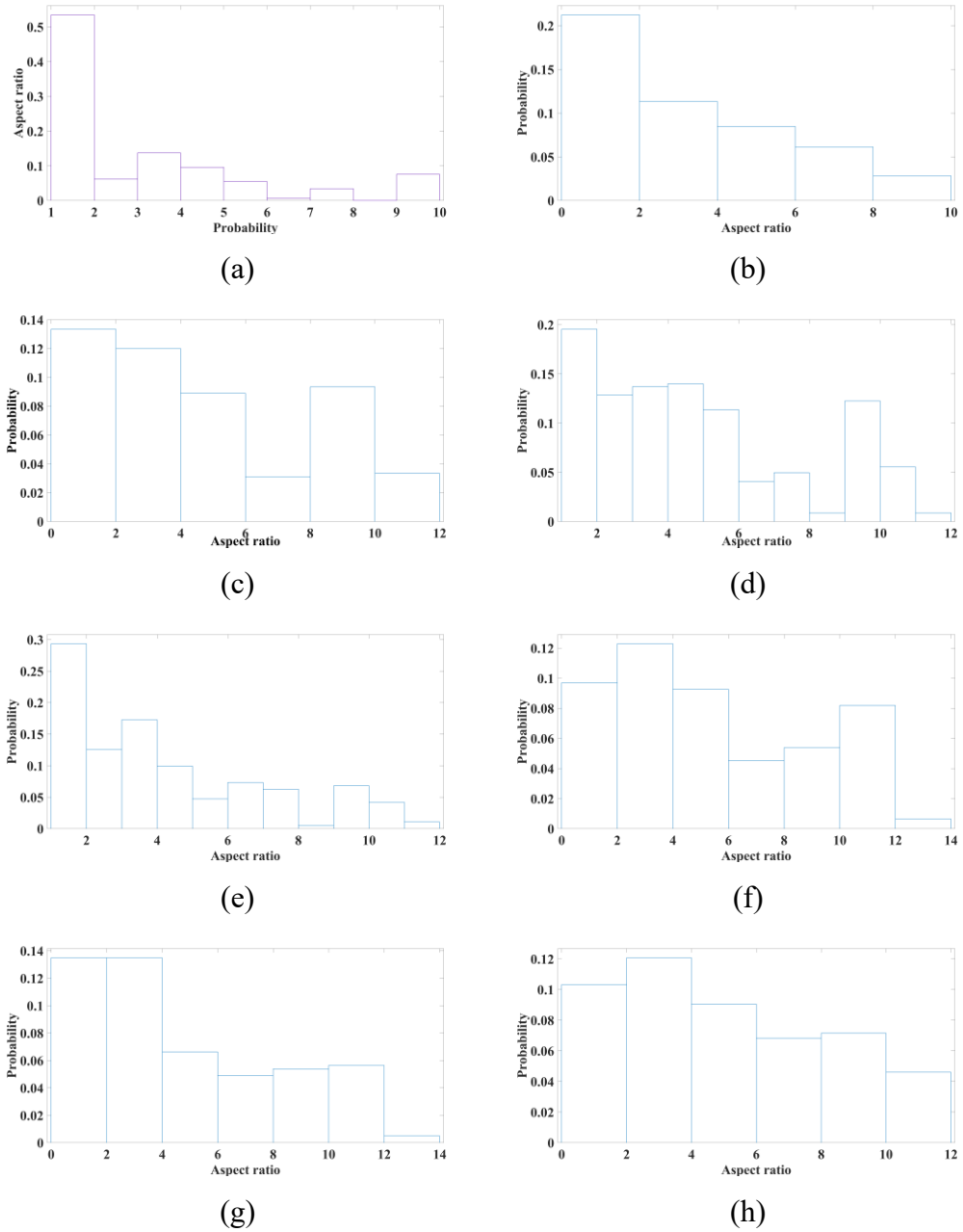

Figure. 19 Aspect ratio distribution of wear debris.

2.3 Conclusion

In this section, a predictive simulation method is proposed for modeling the wear debris generation procedure between rough surfaces at mesoscale. The wear model is based on the atomic attrition mechanism which was found in microscale. The proposed method takes advantage in giving out the information of wear debris in detail, by which the characteristics of wear debris in each step can be obtained.

The numerical prediction procedure is presented by a case study and results are compared with existing models quantitatively or qualitatively. A Monte Carlo simulation is carried out on 100 pairs of rough surfaces to avoid the effect of random topologies. Non-linear wear volume is found in several worn surfaces which also occurs in other microscale researches. The statistical characteristics are analyzed and the predictions of wear volume are in good accordance with results by finite element method. The amount of wear debris is well fitted by a power function with respect to simulation steps and predicts an acceptable more debris comparing with the dynamic model. The distribution of wear debris size follows a Weibull distribution in the mass, while a peak appears around $120\,\mu m$ which cannot be well fitted. It is also found that particles with high aspect ratios increase during the wear process and the corresponding distribution of each steps is given out. It should be noted that the results presented by the case study can only be used when the work conditions are exactly the same, otherwise, one should go through the process with customized parameters to get specific predictions.

This work provides an available method for predicting the generation of wear debris with multidimensional information, which may help the readers with enhanced prognostic result by wear debris from multiple perspectives. Further works will concentrate on building the relationship between the simulation steps with the physical temporal meaning and giving out a usable degradation model by using the detailed information of wear debris.

3. Monitoring abrasive debris online

Contents of the Chapter have been adapted from:

2[J] Tongyang Li, Shaoping Wang, Enrico Zio, Jian Shi and Wei Hong. Aliasing signal separation of superimposed abrasive debris based on degenerate unmixing estimation technique. Sensors, 2018, 18(3): 866.

9[J] Wei Hong, Tongyang Li, Shaoping Wang, Enrico Zio and Zebing Zhou. A General Correction Framework for Aliasing Error of Inductive Oil Debris Detection Based on Artificial Neural Network. Measurement Science and Technology.

2[C] Tongyang Li, Shaoping Wang, Jian Shi and Zhonghai Ma. Simulation on neural networks for DUET-based delay estimation of abrasive debris signal separation, CSAA/IET International Conference on Aircraft Utility Systems 2018 (AUS2018).

4[C] Tongyang Li, Shaoping Wang, Enrico Zio, Jian Shi and Zhe Yang. Aliasing Signal Separation for Superimposition of Inductive Debris Detection Using CNN-Based DUET, IEEE Conference on Industrial Electronics and Applications 2019 (ICIEA 2019).

5[C] Tongyang Li, Shaoping Wang, Enrico Zio, Jian Shi and Wei Hong. Experimental Study on Inductive Method for Online Material Loss Detection with High Debris Concentration, The 2nd International Conference on Material Strength and Applied Mechanics (MSAM 2019)

Accurate and real-time data are needed for online state estimation. In recent years, online detection methods have been widely studied for real-time monitoring [123]. Among the debris detection methods, those based on inductive principles have shown advantages in non-invasion, insensitivity to oil quality, capacity to differentiate ferrous and non-ferrous wear debris, and easy installation on non-transparent pipes, as compared with other methods including optics, capacitance, resistance, ultrasonic, and X-ray approaches [13]. However, high throughput of debris in aviation hydraulic system makes the inductive sensors fail to identify the aliasing signals. To address the

serious mixing of pipe abrasive debris, in Section 3.1, the aliasing problem is analyzed and the serial layout of detection sensors is proposed to simulate an anechoic condition with phase differences of wear particles. Section 3.2 describes the degenerate unmixing estimation technique used to separate the aliasing signals. An improved convolutional neural network (CNN) combined with degenerate unmixing estimation technique (DUET) is proposed in Section 3.3 which offers an online solution for the aliasing signal separation. In Section 3.4, an experiment is conducted for practical aliasing signals separation and the results are discussed. In Section 3.5, some conclusions and remarks are presented.

3.1 Aliasing Signal Separation Detection Structure

Although there may exist several kinds of inductive debris detection sensors with different parameters and performance, the principles of these sensors should be the same. We employ radial magnetic field (RMF) sensor which is based on the inductive principle [13] as the leading role in our research, since this type of sensor is developed by the laboratory of the author independently and the experimental setup is complete. The prototype of the inductive debris detection sensor based on dual excitation sources [57] is shown in Figure. 20. For details of the sensor, see [13, 57].

Figure. 20 radial magnetic field debris detection sensor

The coil is wound along the iron core and the magnetic field is perpendicular to the pipe. This kind of sensor shows good performance with magnetic uniformity, and the output voltage is calculated as follows:

$$u = -2NN_D IS_x S_y S_z \frac{\mu(\mu_r - 1)}{\mu_r} \frac{l'(x)}{l^3(x)} v \tag{3-1}$$

where N and N_D are the numbers of turns of the inductive coil, I is the current in the inductive coil, S_x, S_y, and S_z are the sizes of the particles, μ and μ_r are the permeability of the vacuum and the relative permeability of the debris, $l(x)$ is the location of the debris, and v is the debris speed along the *x* axis.

The size of the debris can be estimated if the output voltage is measured. The size of the debris is one of the key indicators for the wear prognosis. During normal operation, the debris size is in the 1~20 μm range. With an increase in the severity of wear, larger debris in the 50~100 μm range is generated more frequently, and at the stoppage a large number of debris above 200 μm are produced. The poles of the output voltages are related to the debris sizes, and the poles are the solutions of the following equation:

$$ul^4(x) = -2NN_D IS_x S_y S_z \frac{\mu(\mu_r - 1)}{\mu_r} (l''(x)l(x) - 3(l'(x))^2)v. \tag{3-2}$$

For a certain sensor, the intrinsic parameters are confirmed. Assuming that each particle has a d diameter sphere, the value for the measured particle can then be obtained by substituting the measured poles:

$$d = \sqrt[3]{\frac{3\mu_r u l^4(x)}{-NN_D I\mu(\mu_r - 1)(l''(x)l(x) - 3(l'(x))^2)v\pi}} \tag{3-3}$$

by which the sizes of the particles can be estimated. The values of the poles and the relative locations where the poles appear are the key parameters for the size estimation.

When the aliasing appears, a large peak value is measured rather than two real small measured induced voltages. Under this circumstance, the measured aliasing signal could not truly reflect the actual abrasive debris condition. So, an effective aliasing signal separation algorithm of superimposed abrasive debris is urgently needed. For speech separation, usually two or more microphones are arranged in the

environment to collect the speech signals. The limitation of using one microphone is that an infinite number of solutions can be obtained from only one aliasing signal. By using two or more microphones, the same sound travels and arrives at different microphones with different delays and attenuations, resulting in different signals. The signals with different delays and attenuations are the observations of the sound from different perspectives in the time-frequency domain, which gives opportunities for the separation of the sounds. As for the abrasive debris detection, if the debris induces voltages with different delays or attenuations when going through different sensors, the aliasing signals can be separated into several estimated sources from the time-frequency domain. The time-frequency domain method for the debris detection signals separation is more suitable compared with the speech signals separation. The debris in the oil will only go through the sensors once, while the sound will be reflected by the walls and arrive at one microphone several times, forming the so-called echoic system. Besides, because of the viscosity of the oil, particles transfer in the oil with different velocities, which leads to different phase displacements of two particles at two different locations in the oil pipe. The inherent characteristics of the debris detection guarantee that most of the superimposed abrasive debris will show different delays and attenuations after moving for some distance.

Based on the analysis above, a serial layout of detection sensors is proposed in this thesis. The layout of the sensors is shown in Figure. 21. Two sensors with similar performances are installed in series on an oil pipe. When the i_{th} particle passes through the oil pipe, the output of sensor 1 is $s_{i1}(t)$ and the output of sensor 2 is $s_{i2}(t)$. Since the two sensors should have a similar output for the same passing particle, the output of sensor 1 is simplified to be $s_i(t)$ and the output of sensor 2 is $a_i s_i(t-\delta_i)$, where a_i and δ_i are the amplitude and the phase difference of the induced signal in comparison to sensor 1. Assuming that M particles pass through the sensors with a constant speed, in a period of time t, the output of the two sensors is:

$$y_1(t) = \sum_{i=1}^{M} s_i(t) \tag{3-4}$$

$$y_2(t) = \sum_{i=1}^{M} a_i s_i(t - \delta_i) \tag{3-5}$$

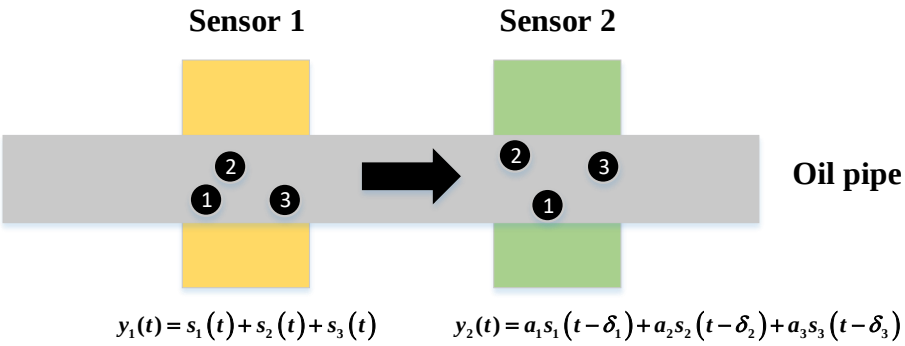

Figure. 21 Detection layout based on two radial magnetic field (RMF) sensors.

For the layout shown in Figure. 21, there are three possible kinds of output signals. Firstly, if the debris remains relative static from sensor 1 to sensor 2, the output of sensor 1 will be equal to that of sensor 2 by shifting the signal of sensor 2 ahead. In this situation, one of the two signals is superfluous and if aliasing occurs, the following aliasing signals separation algorithm cannot provide the correct result but will recognize that there is no signal mixing. Secondly, if there are relative motions of the debris and the three particles cause aliasing in one sensor's output signal but no aliasing in the other sensor's output signal, no more algorithms need to be employed for separation. However, because this situation cannot be recognized, the algorithms will still be conducted and give out the right solution. The third situation arises when aliasing occurs in both sensors' output signals and the signals are different. The following algorithm is intended to be employed in this situation.

3.2 Aliasing Signals Separation Based on the Degenerate Unmixing Estimation Technique

The sensor output is composed of debris signals and interferences which come from random noise and specific frequency interferences. The band pass filter is firstly used to improve the SNR [72]. Then, the processed signals are used for the separation.

The aliasing signal originates when particles are very close, in which the induced voltages are superimposed in the time domain. According to the principle of the RMF sensor shown in Eq. (3-1), the outputs of the sensor are different when two different particles pass through the same sensor. So, it is possible to separate the sources in the time-frequency domain if one point is dominated only by one source, which is also called W-Disjoint Orthogonality. The Short Time Fourier Transform (STFT) of a signal $s_i(t)$ is defined as:

$$\hat{s}_i(\tau,\omega) := F^W[s_i](\tau,\omega) := \frac{1}{\sqrt{2\pi}}\int_{-\infty}^{\infty} W(t-\tau)s_i(t)e^{-j\omega t}\mathrm{d}t \tag{3-6}$$

by which the aliasing signals are then transformed into the time-frequency domain using a Hamming window. If the two sources satisfy:

$$\hat{s}_i(\tau,\omega)\hat{s}_j(\tau,\omega) = 0 \quad \tau > 0, \ \ \omega > 0, \quad \forall i \neq j, \tag{3-7}$$

then the two sources can be separated. Separating the sources from the aliasing signals is thus a problem of classifying the points from a mixed signal in the time-frequency domain. For sensor 1, the i_{th} source is:

$$\hat{s}_i(\tau,\omega) = M_i(\tau,\omega)\hat{y}_1(\tau,\omega), \quad \forall \tau,\omega \tag{3-8}$$

where M is the mask function:

$$M_i(\tau,\omega) := \begin{cases} 1 & \hat{s}_i(\tau,\omega) \neq 0 \\ 0 & otherwise. \end{cases} \tag{3-9}$$

According to Reference [124], to apply the DUET method to solve a blend source separation problem, three additional assumptions should be satisfied:

(1) Two measured sensors are locally stationary, which means that the two sensors should not be moved during detection to avoid the error of the phase shift.

(2) Phase ambiguity may arise if two sensors are close enough, which is determined by:

$$\left|\omega\delta_i\right| < \pi, \quad \forall\omega, \forall i. \tag{3-10}$$

For the detection sensors, the limitation becomes:

$$D < \frac{\pi v}{\omega_{\max}} \tag{3-11}$$

where D is the distance between the two sensors, v is the oil flow speed, and $\omega_{\max}$ is the maximum frequency of sources.

(3) The two sources should have different spatial signatures, which are given as:

$$\left(a_i \neq a_j\right) or \left(\delta_i \neq \delta_j\right), \quad \forall i \neq j. \tag{3-12}$$

For the inductive debris detection method, the assumptions can be met by installing the sensors under the serial layout proposed in Section 2. The aliasing signals can be rewritten as:

$$\begin{bmatrix} \hat{y}_1(\tau,\omega) \\ \hat{y}_2(\tau,\omega) \end{bmatrix} = \begin{bmatrix} 1 & \cdots & 1 \\ a_1 e^{-j\omega\delta_1} & \cdots & a_M e^{-j\omega\delta_M} \end{bmatrix} \begin{bmatrix} \hat{s}_1(\tau,\omega) \\ \vdots \\ \hat{s}_M(\tau,\omega) \end{bmatrix} \tag{3-13}$$

where $\hat{y}(\tau,\omega)$ is the STFT of $y(t)$ and for each (τ,ω)

$$\begin{bmatrix} \hat{y}_1(\tau,\omega) \\ \hat{y}_2(\tau,\omega) \end{bmatrix} = \begin{bmatrix} 1 \\ a_i e^{-j\omega\delta_i} \end{bmatrix} \hat{s}_i(\tau,\omega) \quad \text{for some } i \tag{3-14}$$

At each time-frequency point we can obtain a pair of aliasing parameters, $\tilde{a}_i(\tau,\omega)$ and $\tilde{\delta}_i(\tau,\omega)$.

$$\tilde{a}(\tau,\omega) = \left|\frac{\hat{y}_2(\tau,\omega)}{\hat{y}_1(\tau,\omega)}\right| \tag{3-15}$$

$$\tilde{\delta}(\tau,\omega) = \left(\frac{1}{\omega}\right) \angle \left(\frac{\hat{y}_2(\tau,\omega)}{\hat{y}_1(\tau,\omega)}\right) \tag{3-16}$$

These parameters are the attenuation estimator and delay estimator, respectively, which denote the amplitude ratio and the phase difference of the sources detected by sensor 2 relative to those of sensor 1. In fact, only M pairs of parameters are the actual aliasing parameters, which means we need to determine the real values (a_i, δ_i) from the estimators sets. The sources can be demixed by:

$$M_i(\tau,\omega) := \begin{cases} 1 & \left(\tilde{a}(\tau,\omega), \tilde{\delta}(\tau,\omega)\right) = (a_i, \delta_i) \\ 0 & \textit{otherwise.} \end{cases} \tag{3-17}$$

and, then, the sources are converted to the time domain and the separated sources are obtained.

Usually, a two-dimensional weighted histogram is employed to obtain the actual aliasing parameters [125]. The weight $W(a,\delta)$ is calculated by:

$$W(a,\delta) = \left|\hat{y}_1(\tau,\omega)\,\hat{y}_2(\tau,\omega)\right|. \tag{3-18}$$

The entire process of separating the sources from the aliasing signals of two sensors is shown in Figure. 22.

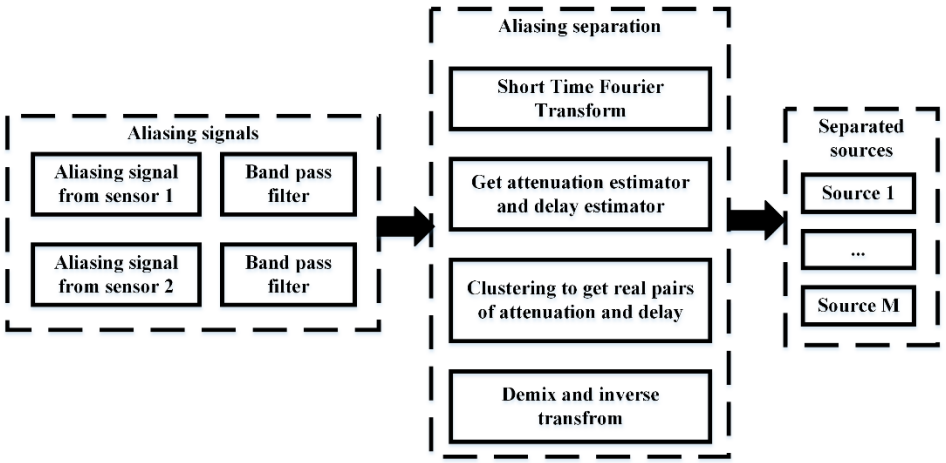

Figure. 22 Flow chart of aliasing signals separation.

3.3 Convolutional neural network Based degenerate unmixing estimation technique

3.3.1 The disordering features in networks for debris signals

There are three main shortcomings using the original DUET [68, 69] method for debris aliasing signal separation, which converge on the two-dimensional weighted histogram method. Firstly, being different from the original application on the speech signals, real time processing is needed for debris signals. Secondly, instead of one-time separation for a speech signal, large amount of debris signal segments is queued up for being processed. Thirdly, manual operation of the two-dimensional weighted histogram may introduce human errors into the method.

Neural networks have been studied a lot as machine learning methods and widely used for the speech source separation [126-131]. Networks including the feedforward network, cascade forward network, auto-encoder, sparse auto-encoder and convolutional neural networks are attempted. Networks with the same type but with different parameters are also tried, like the two-layer convolutional neural networks. In fact, in the aliasing signal separation, the attenuation is a constant and the most important is to get an accurate parameter delay.

If the aliasing signals serve as the input and the output $s_{\text{label}} = \{\delta_1, \delta_2, ..., \delta_n\}$ is the set of the relative phase differences where n is the number of the particles, the labeled output can be any element in

$$S_{\text{label}} = \{(x_1, x_2, ..., x_n) \mid x_1, x_2, ..., x_n \in s_{\text{label}}, x_1 \neq x_2 \neq ...x_n\}. \tag{3-19}$$

Compared with the original networks, the schematic structure of the network with disordering features is shown in Figure. 23.

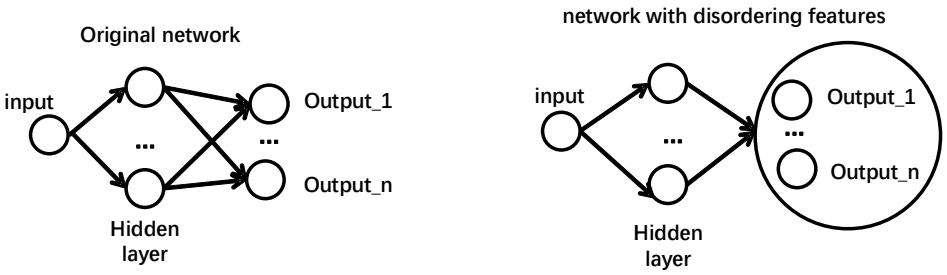

Figure. 23 Schematic structure of the networks.

The original training target for the regression networks is to minimize the loss function where mean square error (MSE) is usually used. By minimizing the MSE, the difference between the output of the network and the labeled value can be decreased effectively. However, when the structure becomes the network with disordering features, the original one-one corresponding training target will lead to an indistinguishable result. The training target is then to minimize the loss function

$$\frac{\sum_{i=1}^{n}(\sum_{j=1}^{n} x_j{}^{i} - \sum_{j=1}^{n} \hat{x}_j{}^{i})^{\frac{2}{i}}}{n} + \lambda\varphi(x,\hat{x}),\ x \in s_{\text{label}}, \hat{x} \in s_{\text{out}} \tag{3-20}$$

where φ is the penalty function which is defined as the difference of the variance of the predicted values and the variance of the labeled values and λ is its coefficient.

The original method which can only be used to evaluate the one-one corresponding training performance is modified as the minimum of

$$\frac{\sum_{i=1}^{n}(x_i - \hat{x}_i)^2}{n},(\hat{x}_1,\hat{x}_2,\ldots\hat{x}_n) \in s_{\text{label}},(\hat{x}_1,\hat{x}_2,\ldots\hat{x}_n) \in s_{\text{out}}. \tag{3-21}$$

With the modified training target and accuracy, the output layer of the network is regarded as a group instead of individual neurons, which is also the improvement of the network for debris feature extraction.

Neural network is a machine learning method based on large dataset. The first thing is to obtain the dataset for training. In fact, the data we got from the experiment are far away from the requirement and the experimental data cannot be separated perfectly for the training. Hence, the simulated data are used here for the training.

The simulated data are based on the sine wave. Each of the particles is described

as a sine section with period from $\frac{\pi}{2}$ to $\frac{3\pi}{2}$. The sine sections with random amplitude and phase are superimposed to be the first aliasing signal. Modify the amplitude and phase of each sine sections and add them together to get the second aliasing signal. The two signals can be obtained and their delay characteristics can also be calculated during the process, which composed the dataset for training.

As is shown in Figure. 24, the framework for the parameter estimation is displayed. The points of aliasing signals are the inputs and the outputs are the parameters.

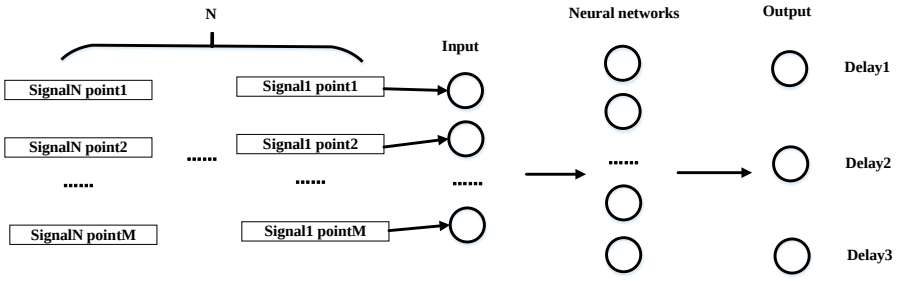

Figure. 24 Framework for the parameter estimation.

In fact, under the supervised learning, the number of the output should be confirmed firstly. In our framework, the output is relied on the number of sources which cannot be known. Fortunately, the DUET method provides a relative accurate number of the sources. So for each number of sources, a network is established and used only for the specified. For the debris sensors, because the attenuation is usually a constant, the estimation of the attenuation can be conducted by other method. The outputs of the proposed networks are only the delays.

Since CNN shows the best result for the test, we employ CNN combining with DUET as the online signal separation method. If an improved CNN is used as the feature extraction method instead of the original two-dimensional weighted histogram method, the flow chart of CNN based DUET is shown in Figure. 25. Because for two certain inductive sensors, the amplification coefficients can be regarded as constants, only the delays are extracted from the network. The simulation results are listed in next section.

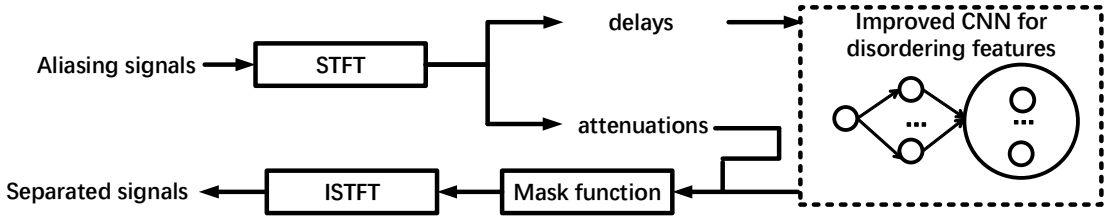

Figure. 25 Flow chart of CNN based DUET.

3.3.2 Simulation results

A. Feedforward networks

The simulation is conducted by using the Matlab neural network toolbox. One-layer and two-layer feedforward networks are tested and the structure is shown in Figure. 26. Different number of hidden nodes are tested and the results are shown in TABLE 2.

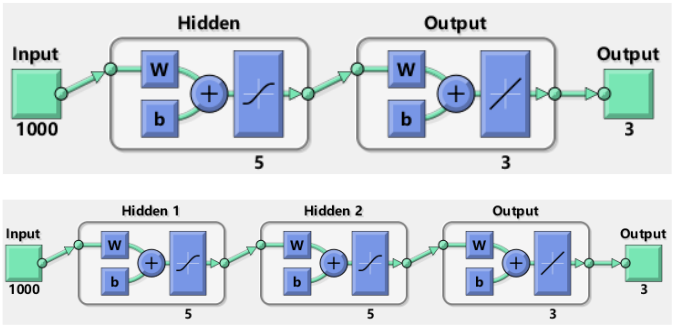

Figure. 26 Feedforward networks structure.

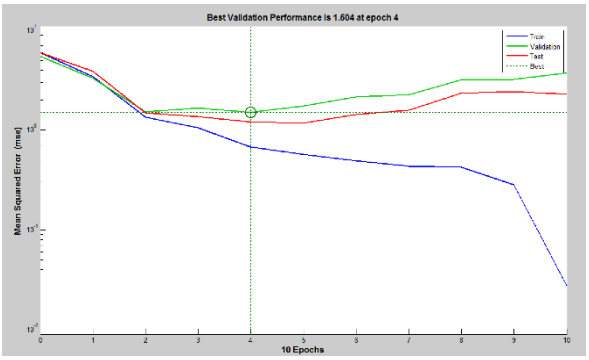

Figure. 27 Mean square error.

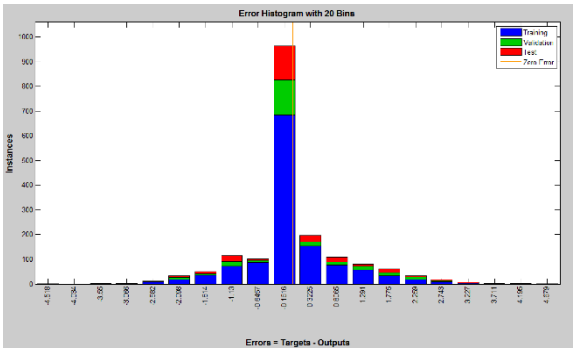

Figure. 28 Error distribution.

The inputs of the networks are the joint matrix of the two signals. Each signal has a length of 500 points data and the joint result is 1000 for the number of inputs. The outputs are three delays because we use three sources to generate the aliasing signals and the networks are only used to estimate the delays of three-source aliasing situation. Gradient descent is used for the training.

1000 groups of samples are used for training and 300 groups of samples are used for testing. Another 300 groups of samples with a noise of normal distribution whose mean value is zero and square error is 0.1 are also used for the test and the mean square error (MSE) are calculated for evaluation the performance of the networks. For each network structure, we can get the MSE of each training step which is shown in Figure. 27 and the error distribution which is shown in Figure. 28. The structure [5] means the feedforward network has one layer and the hidden nodes number is 5. The structure [5 5] means the feedforward network has two layers and the hidden nodes number of the first layer is 5, the number of the second layer is 5.

TABLE 2 Simulation results of Feedforward networks

Network structure	MSE	MSE of data with noise
[5]	0.1819	0.2321
[8]	0.1931	0.2393
[10]	0.1816	0.2306
[12]	0.1827	0.2911
[15]	0.1564	0.2822
[5 5]	0.2016	0.2240

Network structure	MSE	MSE of data with noise
[8 5]	0.1782	0.2412
[10 5]	0.1925	0.2287
[5 10]	0.2038	0.2727
[8 8]	0.1929	0.2553

Because the initial weight of the networks are random, the results shown in TABLE 2 is the mean value of 10 times training. From the results we can easily see that the different structure of a feedforward network has little influence on the estimation. Generally, the MSE of the data with noise is higher than the MSE of the clear data.

B. Cascade-forward networks

The setting of the inputs and outputs are the same as the feedforward networks'. The structure of the network is shown in Figure. 29. Both cascade-forward networks with one layer and two layers are tested. The results are listed in TABLE 3.

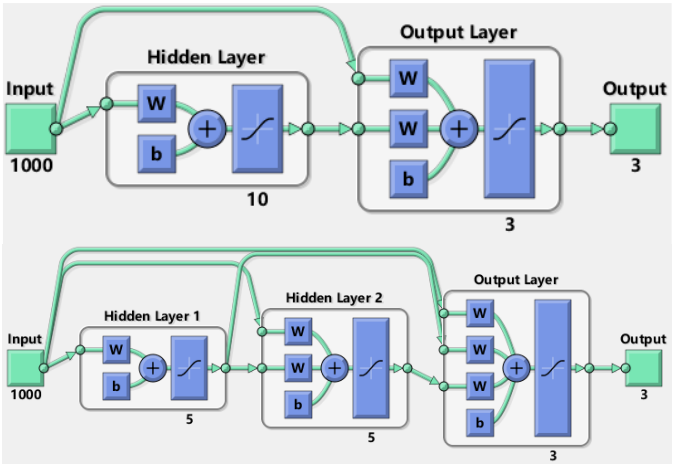

Figure. 29 Cascade-forward networks structure.

TABLE 3 Simulation results of cascadeforward networks

Network structure	MSE	MSE of data with noise
[5]	0.1394	0.2803
[8]	0.2036	0.2393
[10]	0.1795	0.2101
[5 5]	0.2084	0.1976
[8 8]	0.1953	0.2480

The cascade-forward networks show a similar result with the feedforward networks. However, the time cost of the training is about 10 times than that of the feedforward networks. Different structures show an analogous MSE for both the clear data and the data with noise.

C. Auto-encoder

By using the traditional training method, the scale of the networks cannot be very large. The feedforward and cascade-forward networks proposed above consist of about one or two layers and totally under 20 nodes. However, the cost of the time for the training is very large. The auto-encoder changes the training method and reduces the cost largely. The scale of the network by auto-encoder can be thousands of nodes and the cost of time is approximately equals to train a 20 nodes two-layer feedforward network, which makes it an important branch in deep learning. The structure of the auto-encoder is shown in Figure. 30.

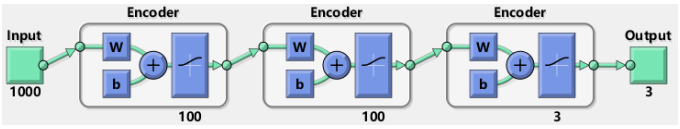

Figure. 30 Auto-encoder structure.

Because of the deep learning toolbox of the Matlab has stopped updated, the method is also tested by tensor-flow. The results of different node numbers are shown in TABLE 4.

TABLE 4 Simulation results of auto-encoder networks

Network structure	MSE	MSE of data with noise
[50 50]	0.1332	0.1295
[100 50]	0.1177	0.1221
[100 100]	0.1269	0.1227
[200 100]	0.1257	0.1265
[50 50 50]	0.1326	0.1220
[100 100 50]	0.1224	0.1260
[100 100 100]	0.1337	0.1365

The result of auto-encoder is obviously better than the feedforward and cascade-forward networks. Less than 20 nodes may not fit the relation well. We can also see that the result is not better and better with the increasing of the number of the nodes. The best result is shown at [100 50]. The increasing of nodes does not promote the accuracy but only increases the cost of time. Deep network actually shows a better result.

D. Sparse auto-encoder

The sparse auto-encoder is a modified auto-encoder method with sparse constraint. This kind of method makes most nodes inactive compared with the auto-encoder. The structure of the sparse auto-encoder is the same as the auto-encoder shown in Figure. 30.

The sparsity regularization of the tested networks is set as 4 and the sparsity proportion is set as 0.05. Purelin is chosen as the decoder transfer function. The testing result is shown in TABLE 5.

TABLE 5 Simulation results of sparse auto-encoder networks

Network structure	MSE	MSE of data with noise
[50 50]	0.0412	0.3673
[100 50]	0.0372	0.3691
[100 100]	0.0373	0.3585
[200 100]	0.0375	0.3538

Different from the auto-encoder, result of the sparse auto-encoder shows that it has a higher accuracy in the test of clear data but a lower accuracy in that of data with noise instead of a more accurate result.

E. Convolutional neural networks

The CNN simulation is under the tensor-flow environment. Generally, the structure of CNN is shown in Figure. 31. The input signals are reshaped to a matrix of 2 rows and 500 columns. Convolutional core with different numbers and shapes are tested. Then, the max pooling layer is used. After the full connection layer, three outputs are obtained.

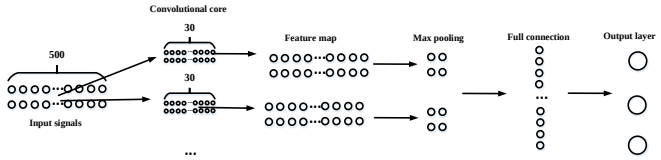

Figure. 31 CNN structure.

The two-layer CNN is after the first max pooling layer, there are another convolutional layer and max pooling layer. The number of nodes for the full connection layer is 256 in one-layer CNN and 1024 in two-layer CNN. Different structure of the CNNs are tested and the results are listed in TABLE 6.

TABLE 6 Simulation results of Convolutional neural networks

Network structure		MSE	MSE of data with noise
10conv20*2	pool2*2	0.1297	0.1183
20conv20*2	pool2*2	0.1150	0.1169
30conv20*2	pool2*2	0.1251	0.1226
10conv30*2	pool2*2	0.1181	0.1136
20conv30*2	pool2*2	0.1177	0.1190
30conv30*2	pool2*2	0.1216	0.1159
10conv30*2	pool2*2 and 10conv15*1 pool2*1	0.0824	0.0841
20conv30*2	pool2*2 and 10conv15*1 pool2*1	0.0854	0.0852
30conv30*2	pool2*2 and 10conv15*1 pool2*1	0.0841	0.0859
10conv30*2	pool2*2 and 20conv10*1 pool2*1	0.0826	0.0881
20conv30*2	pool2*2 and 20conv10*1 pool2*1	0.0851	0.0827
30conv30*2	pool2*2 and 20conv10*1 pool2*1	0.0862	0.0865

3.4 Experiment

To verify the effectiveness of the proposed method for separating the aliasing signals, we conducted an experiment. A larger concentration of particles was injected into the pipe as a proxy of a large flow rate to simulate the actual aliasing environment of the outlet flow of an aviation pump. To satisfy the requirement of the two sensors, the tested part of pipe was slimmed for a high flow speed under the same flow rate. According to Eq. (3-11), the larger the flow speed is, the longer the distance between the two sensors can be. The layout of the experimental system is shown in Figure. 32.

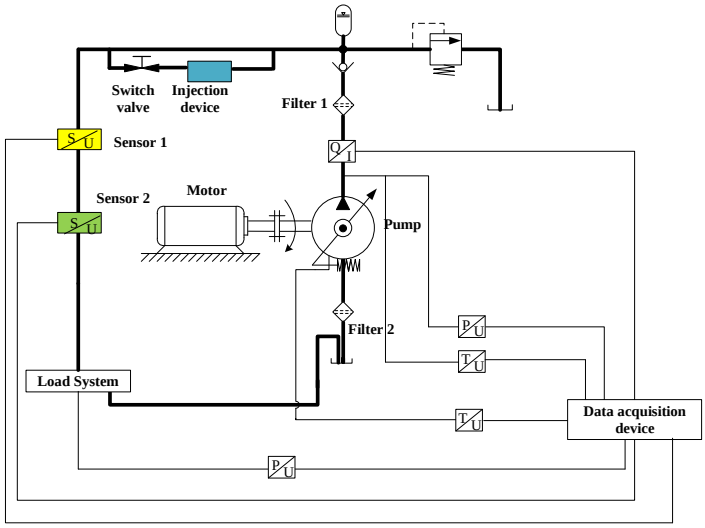

Figure. 32 Experiment layout.

Two oil filters were installed on the input pipe and the output pipe was connected to the pump. The one installed on the input pipe was used to protect the pump from real wear by the contaminant and the other was employed to make sure that the tested part of the pipe contained only the injected tested particles. On the tested part of the pipe, a particle injection device was installed and two similar inductive debris detection sensors were installed in series. The real experimental system is shown in Figure. 33.

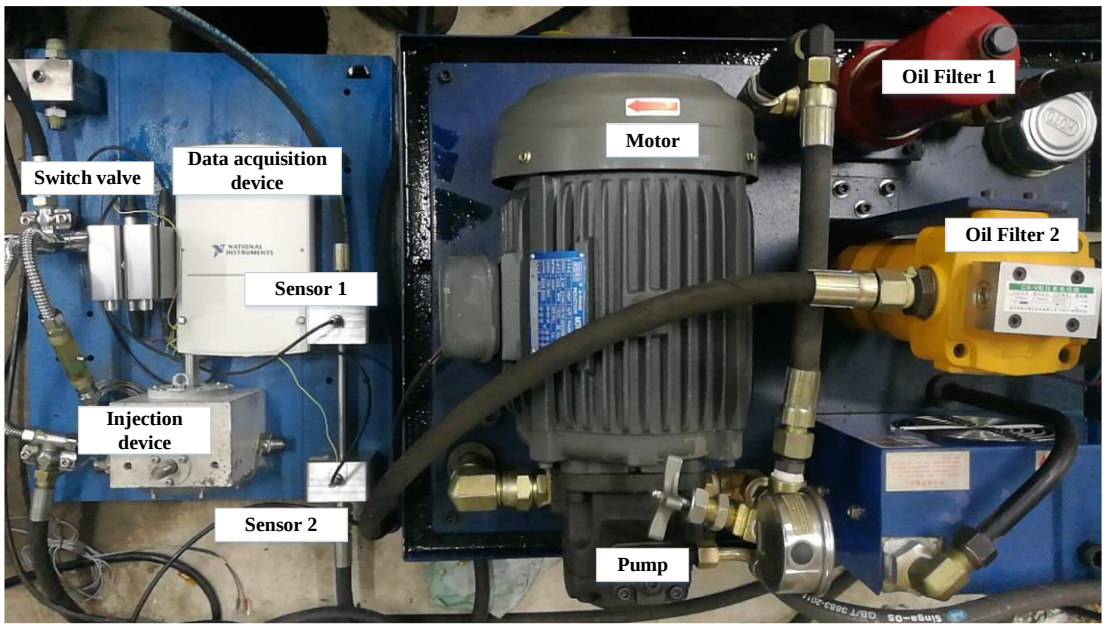

Figure. 33 Experiment system.

By using the injector, particles were injected into the transparent section of the pipe. Without opening the switch valve, particles will not flow with the oil. By opening the switching valve, the particles flow into the tested part of the pipe, gradually generating aliasing signals. When particles pass through the sensors, the induced voltages are collected by the signal acquisition system. Key parameters of the experiment system are listed in TABLE 7.

TABLE 7 Parameters of the experiment system

Parameters	**Values**
Output pressure	0.7 Mpa
Flow rate	60 L/min
Tested pipe diameter	1 cm
Distance between the two sensors	25 cm
Sampling frequency	10 kHz
Size of particles	50~150 μm
Total weight of particles	1 g

Iron powders were employed to replace real abrasive debris. For the first test group, the pump was not started, signals from the two sensors were collected as shown in Figure. 34 (a) displays the signal from sensor 1. By converting the time domain data into frequency domain data, the frequency spectrum can be obtained as shown in Figure. 34 (b). It can be seen that the time domain data are noisy, but there are two strong peaks at 50Hz and 150Hz in the frequency domain. Obviously, the peak at 50Hz is caused by the electromagnetic interference from commercial electrical power. Since no other device runs during the test, 150Hz is caused by the harmonic interference from three-phase electric. Weak peaks can be found at each harmonic frequency like 250Hz. Figure. 34 (c) displays the signal from sensor 2 and the corresponding converting result by discrete Fourier transformation can be found in Figure. 34 (d).

For the second test group, the pump started running but no powders were injected

to the system. Signals measured by sensor 1 can be seen in Figure. 35 (a) and the corresponding frequency spectrum is shown in Figure. 35 (b). Compared with the first group, strong peaks occur at higher frequency near 2000Hz, which is caused by the periodic rotation of the piston pump. Its harmonic interference occurs near 4000Hz. Figure. 35 (c) displays the signal from sensor 2 and the corresponding convert result by discrete Fourier transformation can be found in Figure. 35 (d). Obviously, the method is sensitive to the vibration which is commonly seen in practical conditions.

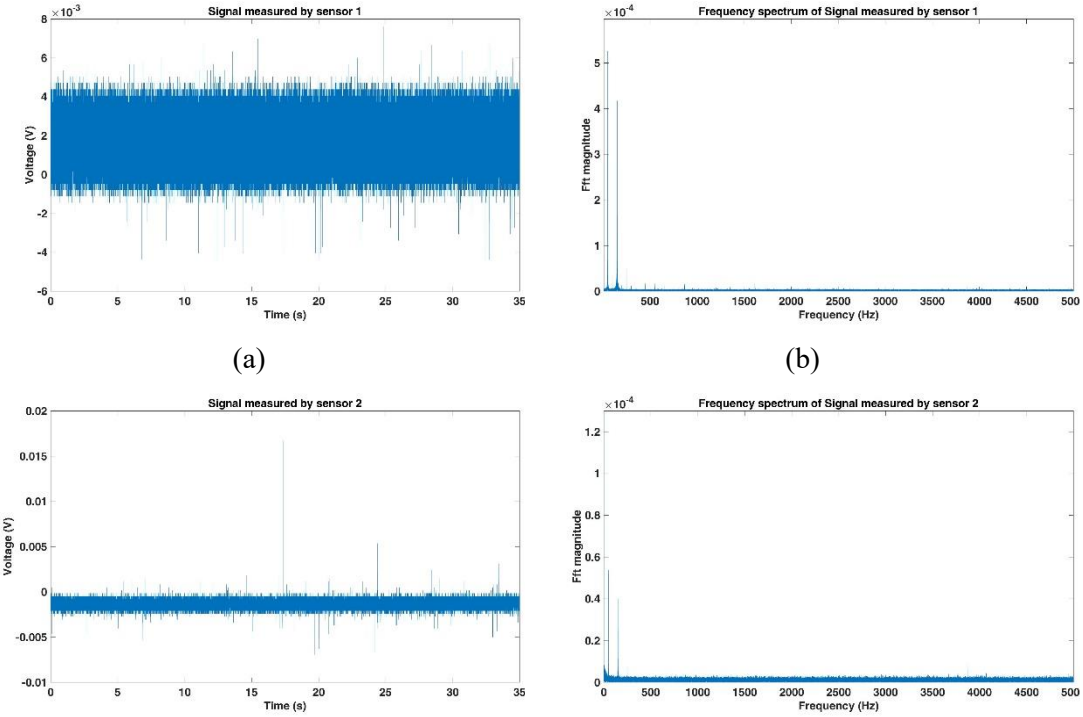

(a) (b)

(c) (d)

Figure. 34 Experiment results when the pump stops.

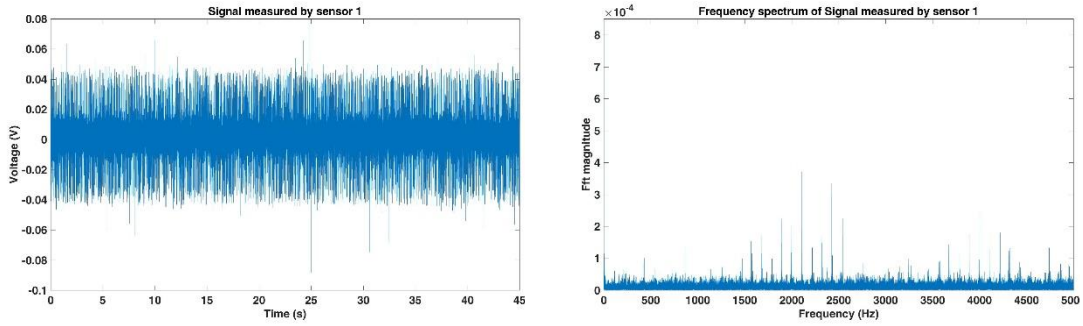

(a) (b)

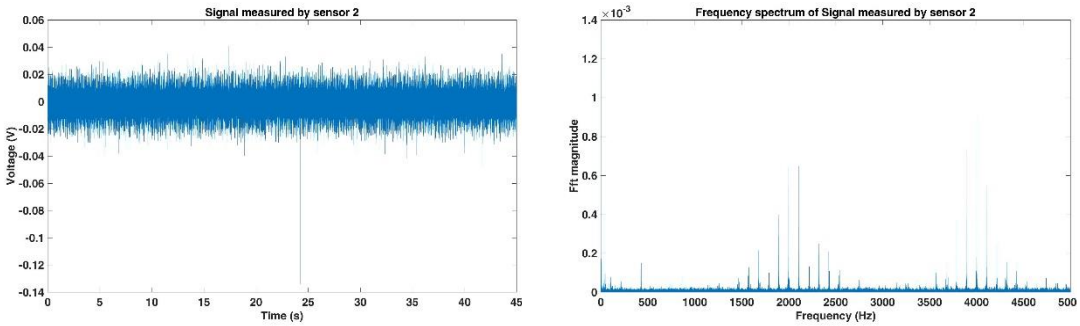

(c) (d)

Figure. 35 Experiment results without debris.

For group 3 to group 10, iron powders with different amounts were injected into the system. The parameters for each group are listed in TABLE 8. In group 3 to group 6, medium powders were tested and in group 7 to group 10, coarse powders were tested. The theoretical amount of powders is estimated by assuming that the density of the iron powders is 3g/cm^3. The results of group 7 are shown in Figure. 36. Unlike the results collected in laboratory conditions, all that can be seen is a noisy waveform that conveys little information. From the frequency domain, no evident difference can be found compared with the result shown in Figure. 35.

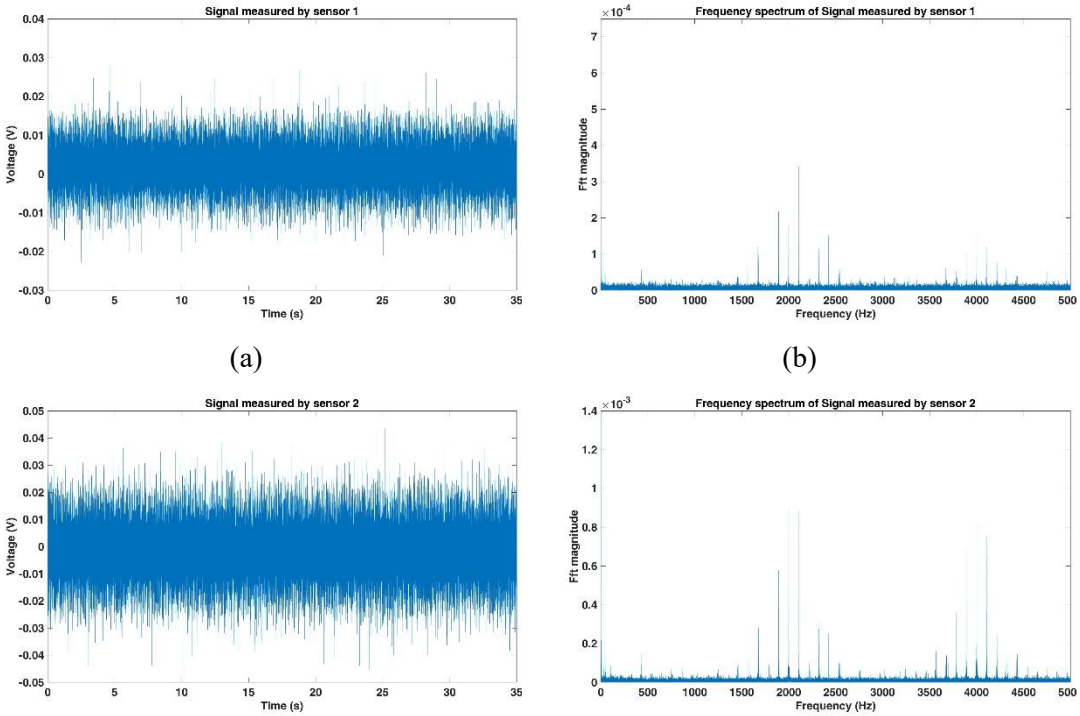

(a) (b)

(c) (d)

Figure. 36 Experiment results with debris.

The induced voltages by debris are aperiodic sine-like waveforms whose frequency is around 100Hz. According to the aforementioned methods, a 200-order digital band-pass filter using hamming window is designed as is shown in Figure. 37. The range of the pass band is from 70Hz to 130Hz. The filter is implemented by MATLAB Filter Designer. The filtered results of the signals shown in Figure. 36 (a) and Figure. 36 (c) are shown in Figure. 38 (a) and (b), respectively. The filtered results are much distinct than the unfiltered results. It can be seen that at 10s, the powders were injected into the oil and about 2 seconds later, both the two sensors detected the debris. Obviously, some induced voltages are superimposed and noise by the harmonic interference still exists. By counting the peaks, the amount of debris can be obtained directly.

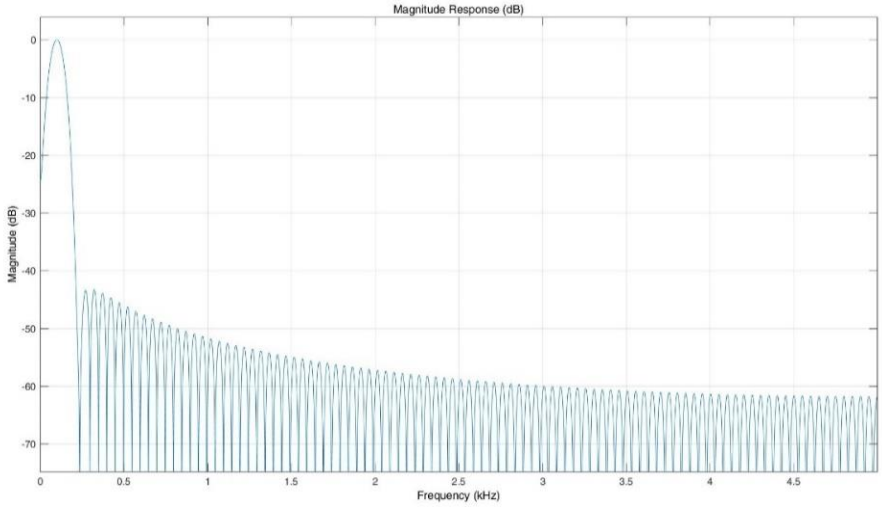

Figure. 37 The designed band-pass filter.

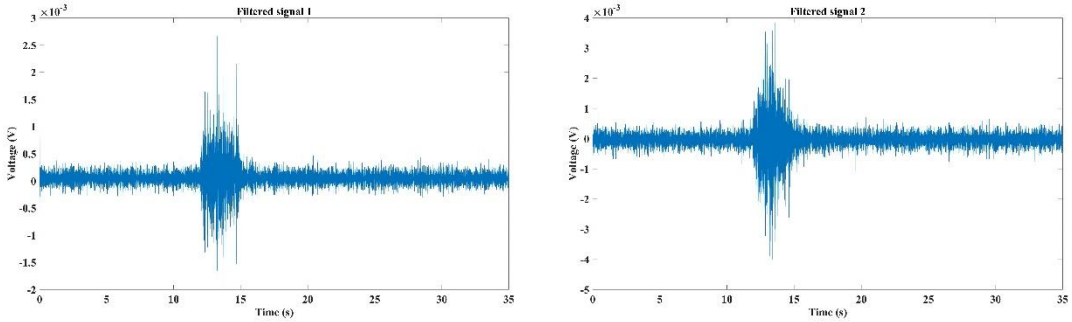

(a) (b)

Figure. 38 Filtered signals.

TABLE 8 Experiment results

Group	Debris	Concentration	Reference	Sensor 1	Sensor 2
3	1g Medium	250mg/L	1.6×10^4	5893	5416
4	2g Medium	500mg /L	3.2×10^4	6798	6545
5	4g Medium	1g/L	6.4×10^4	15890	16341
6	10g Medium	2.5g/L	1.6×10^5	25621	26848
7	1g Coarse	250mg/L	600	436	401
8	2g Coarse	500mg /L	1200	726	792
9	4g Coarse	1g/L	2400	1489	1450
10	10g Coarse	2.5g/L	6000	4256	4534

Six replicates of the experiment were carried out and signals were extracted from the original signals. The signals collected by sensor 2 were shifted in time 0.0196 s ahead to eliminate the error caused by the distance. We can easily find that there are several aliasing sections in the signals which can be extracted from the signals collection, as shown in Figure. 39. The whole extracted signals were first divided into several sections. On each section, the DUET method was conducted. Two of the aliasing sections are labeled in Figure. 39 as a1 and a2, and serve as the examples for the demixing. The size of the Hamming window is 64 samples. We can also see that there are sections where no aliasing occurred (there was no signal mixing). For these sections, the clustering results of the DUET method were only one source and the debris sizes could be estimated without using the mask function.

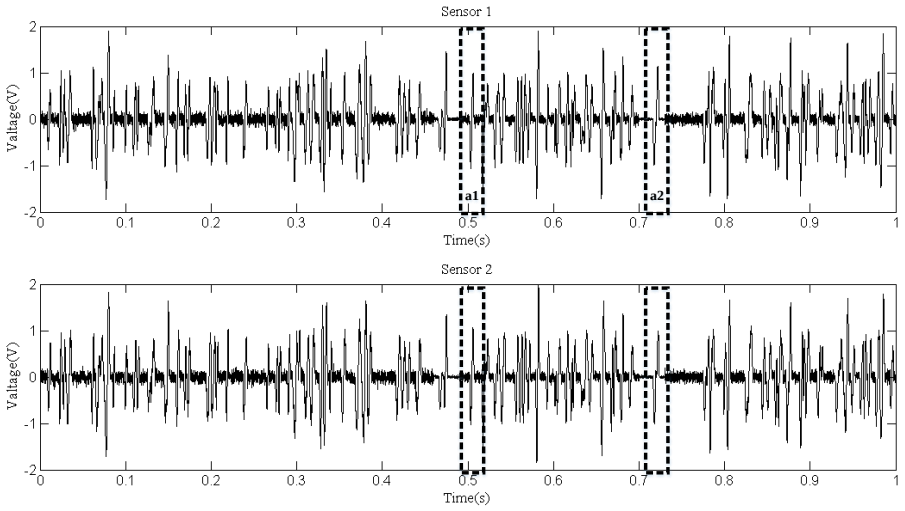

Figure. 39 Extracted signals.

Figure. 40 shows the zoomed image of the signals from sensor 1 and sensor 2, labeled as a1 in Figure. 39. The aliasing phenomenon can be seen intuitively from the curve, and it seems that the induced voltages caused by two particles with different phases and sizes are superimposed. From the two-dimensional weighted histogram shown in Figure. 41, the aliasing parameters were classified into two groups and the peaks of each group were labeled. One point is (2.121,0.909,2.151) and the other is (4.545,0.9091,1.174), which means the delay between the signal from sensor 1 and that from sensor 2 of the source of one particle is 2.121×10^{-4} s and that of the other particle is 4.545×10^{-4} s, because the sampling frequency is 10 kHz. The demixing results are shown in Figure. 42, although the sources are not perfectly separated due to the clustering error.

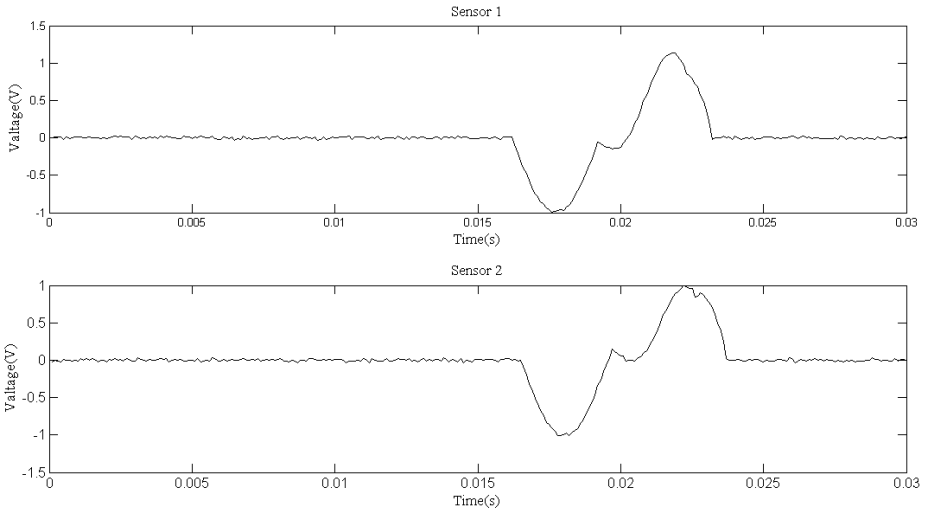

Figure. 40 Aliasing signals of section a1.

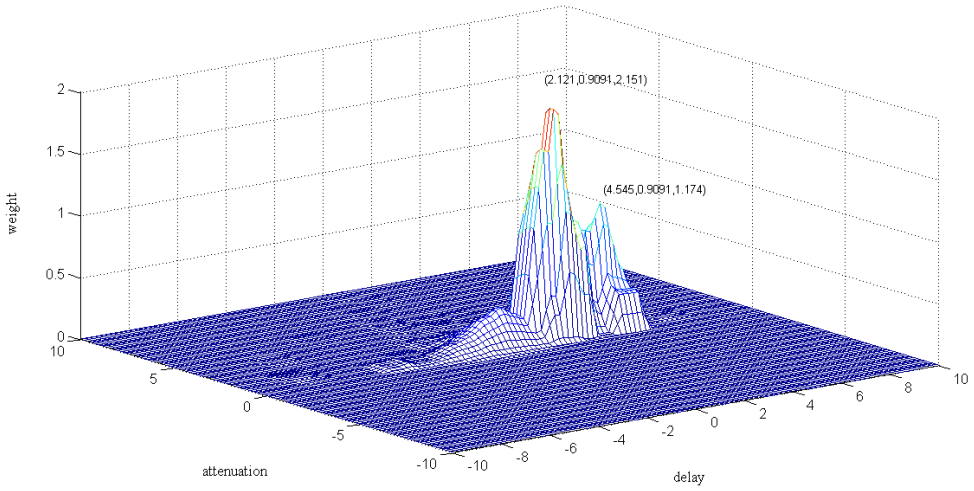

Figure. 41 Clustering result of section a1.

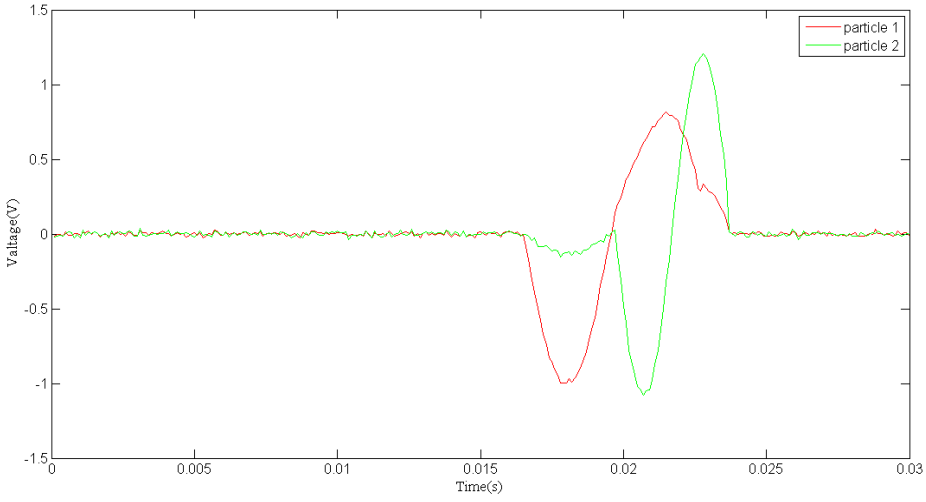

Figure. 42 Demixing result of section a1.

Another zoomed image is shown in Figure. 43, from which we can hardly figure out how many particles have passed through the sensors. If the original signals are used to conduct the particle counting or debris characteristics statistic, then a cumulative error may arise which may cause inaccuracy in the prognosis and diagnosis. In fact, for different accuracies, there may be different clustering results, as shown in Figure. 44 and Figure. 46. This is unavoidable because of the uncertainty of the aliasing parameters. When the phase differences of two sources are not significantly distinguished, the clustering may not give acceptable results. As for the signals shown in Figure. 43, we can never know the original sources, but merely try to obtain a good estimation. Comparing the two demixing results shown in Figure. 45 and Figure. 47, the result which contains four particles is more convincing than the three particles result.

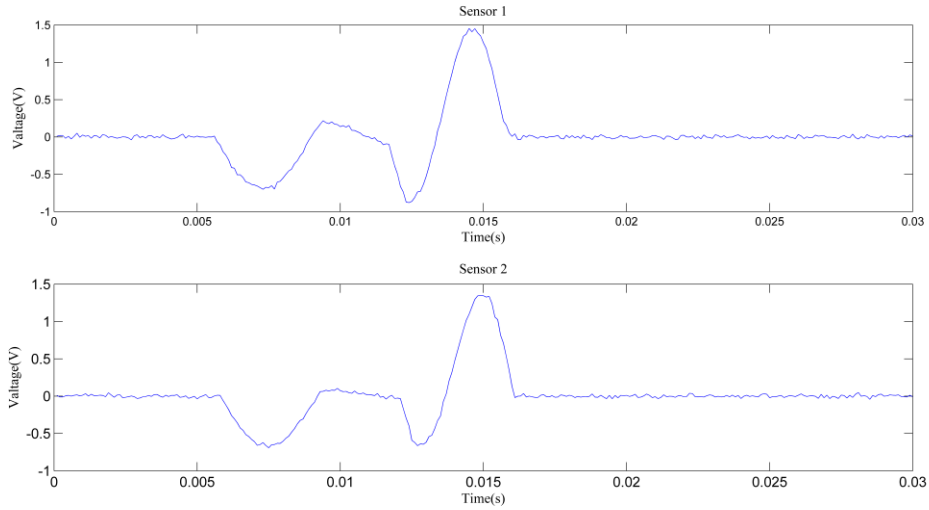

Figure. 43 Aliasing signals of section a2.

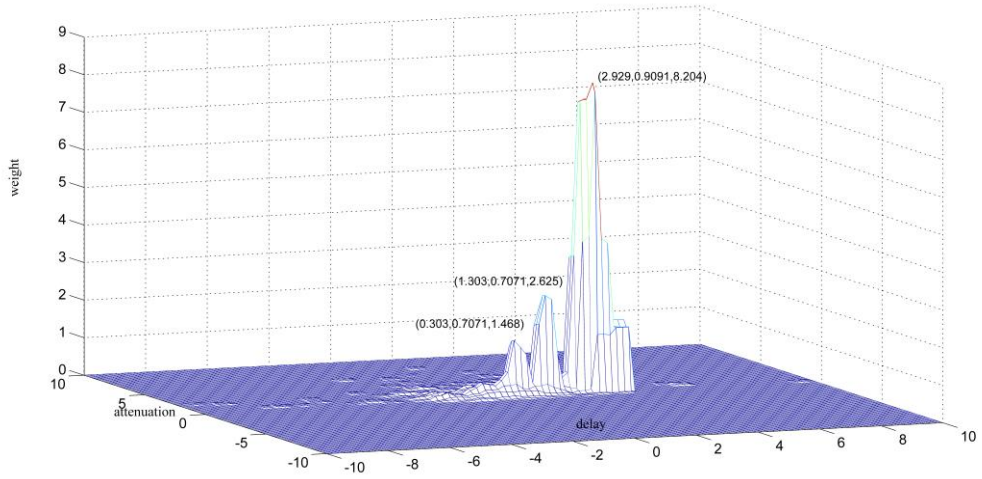

Figure. 44 Clustering result of section a2 into three particles.

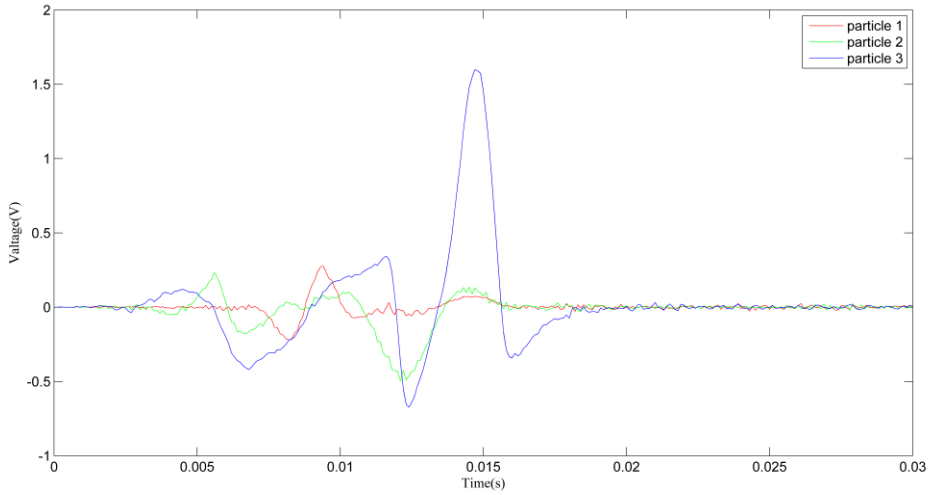

Figure. 45 Demixing result of section a2 into three particles.

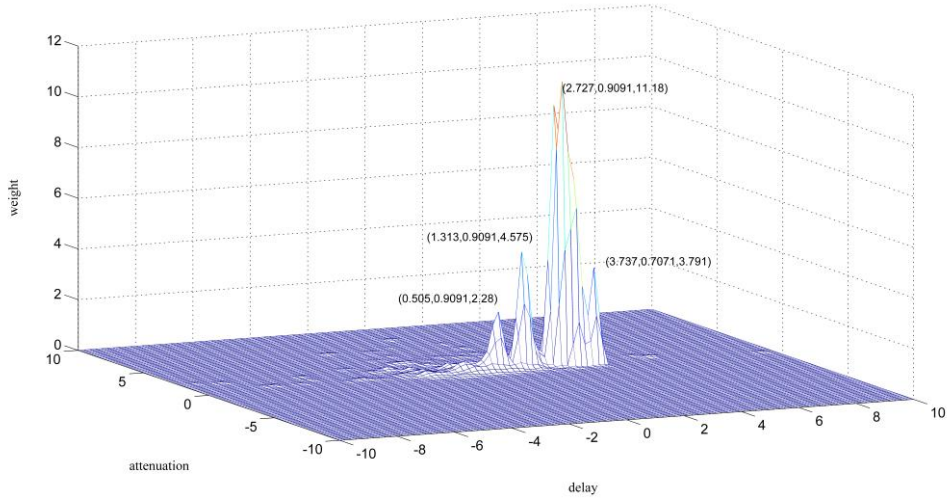

Figure. 46 Clustering result of section a2 into four particles.

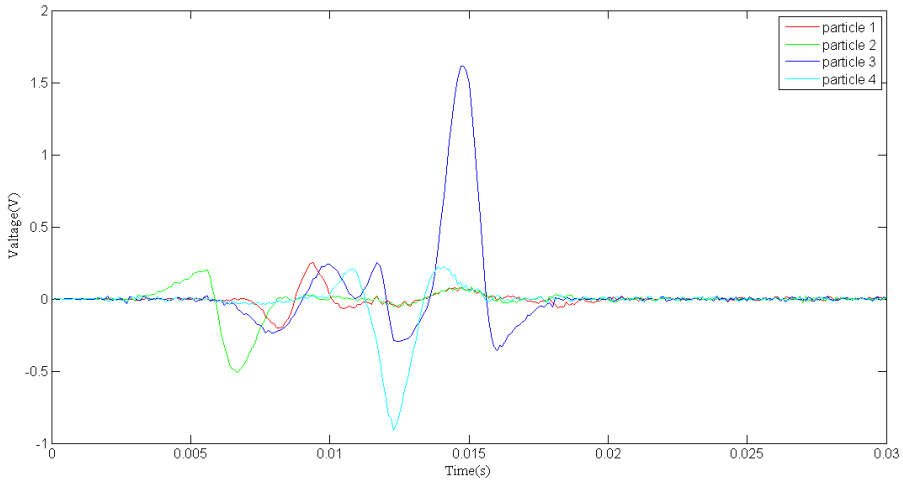

Figure. 47 Demixing result of section a2 into four particles.

To achieve a more satisfying result for section a2, several clustering methods were applied. The main task to solve the problem was to obtain a more accurate estimate of the aliasing parameters. Clustering methods such as k-means are not suitable; when the k-means method is applied, the clustering result does not have a physical interpretation because the clustering center should be around the highest point in the two-dimensional weighted histogram. By going through the close region and applying a combination of parameters, an acceptable result is obtained in Figure. 48.

An acceptable result cannot always be obtained. The sources can only be separated when the delay or the attenuation is different. When both the delay and the attenuation are the same, two sources are recognized as one. As can be seen from the clustering results, the attenuations of the sources are nearly the same, which means that the sensors maintain a stable output. So, the use of delay is an effective way to carry out the aliasing signals separation. In the hydraulic pump test rig, a smaller diameter pipe is adopted, which gives more opportunities for the delays to change.

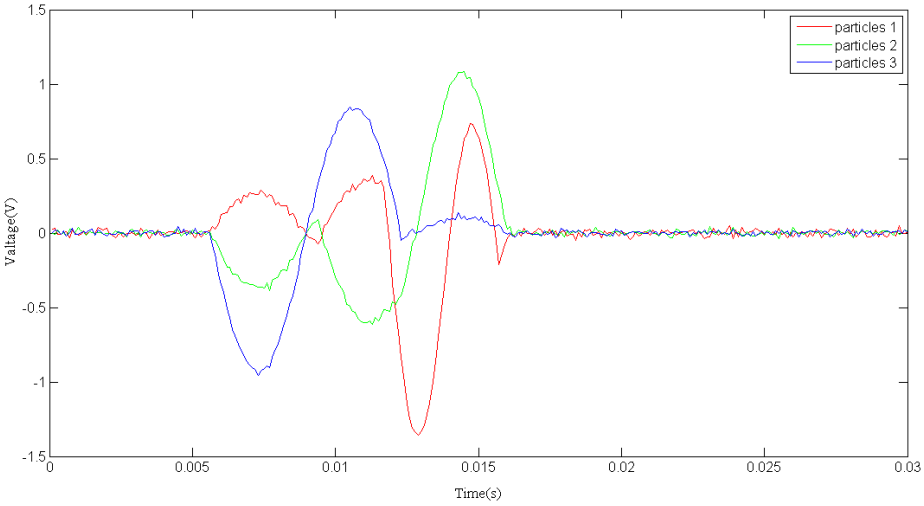

Figure. 48 Demixing result of section a2.

The demixing results of the proposed method cannot be proved directly because the induced voltages of each wear debris cannot be detected. Commonly, for a speech signal demixing result, the best way to confirm the effectiveness is to listen to the sources. Obviously, for the debris signals, we should use another method to verify the demixing accuracy.

For each particle, it is already known that each particle will induce a signal similar to the sine wave. The demixing result of section a1, shown in Figure. 42, and that of section a2, shown in Figure. 48, are apparently acceptable solutions as debris signals. However, we also know that from the aliasing signals we may obtain different demixing results, such as those achieved for section a2, which means the demixing result may have other solutions. To verify that the results reflect the real situation, statistics about the particles sizes are calculated and the results are shown in Figure. 49. From this figure we can see that without the separation, about 17.9% of all particles have sizes larger than 150 μm. Traditionally, the result without separation is believed to be the indicator for the evaluation of wear status. In fact, the particles injected into the injection device are particles ranging in size from 50 μm to 150 μm and that follow a uniform distribution, as listed in Table 1. After demixing, the separated result shows that the sizes of the particles follow a uniform distribution and the result is more

consistent with the real situation than that without separation. We believe that the 17.9% wrongly estimated particles are thus reevaluated reasonably and the accuracy is improved.

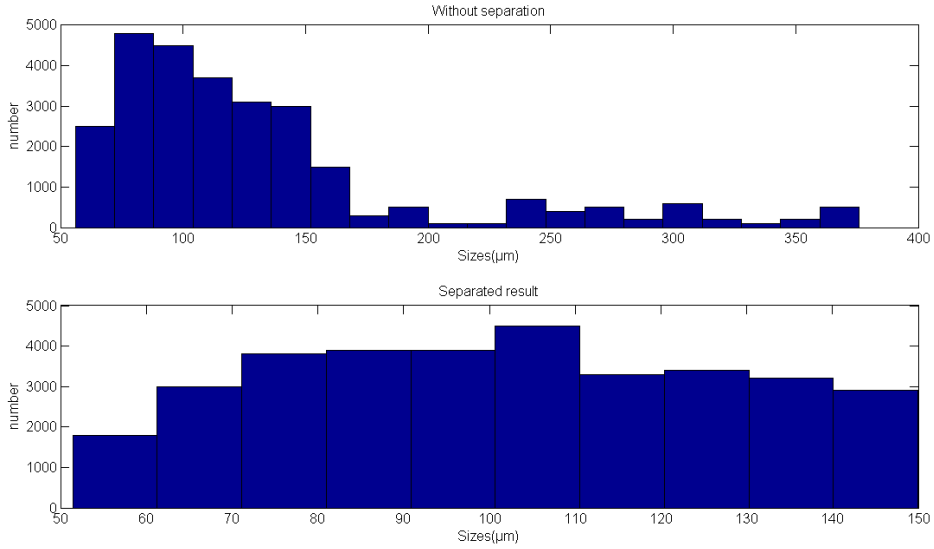

Figure. 49 Statistical result of the number of particle

3.5 Conclusions

Inductive debris detection sensors are designed to identify small wear particles. If the distance between two particles is very small, two small particles may be recognized as one large particle, which is known as the signal aliasing problem in debris detection. Large particles frequently appear only when the machine is severely degraded, which is too late in practice for effective maintenance. With aliasing, at the beginning of degradation, a group of small particles may be recognized as large particles, leading to a wrong estimation of the machine degradation state and maybe even its stoppage for maintenance. For an aviation pump system, the high speed oil flow makes it actually more prone to the aliasing problem, which, then, needs to be addressed.

In this section, the aliasing problem was analyzed and a serial setup of sensors was installed for data acquisition. A band pass filter combined with DUET was employed

to separate the sources from the aliasing signals. To evaluate the performance of the method, a real experiment was conducted. Using the signal pieces extracted from the real signals, the method was shown to be effective in demixing the signals. The result shows that the count of the number of particles is more accurate than the traditional pulse counting method. Statistically, 17.9% particles that are considered to be larger ones are separated to be smaller, and the distribution is more consistent with the real situation. However, two problems were found during the verification. One is that the weight peaks caused by the noise may affect the accuracy of the classification, which prevents the aliasing signals from being well separated. The other is that not all signals can be separated by the proposed method because when the phase displacements of a group of particles are similar, the particles are recognized as one.

Future works will address, on one hand, the evaluation of the capability of the proposed method compared with other possible methods on the aliasing problem, and, on the other hand, eliminating the interferences coming from random noise and specific frequency interferences. In particular, a potential layout of sensors may also be proposed to provide different phase displacements for the method.

4. Matching the model and data for remaining wear life prediction

Contents of the Chapter have been adapted from:

3[J] Tongyang Li, Shaoping Wang, Jian Shi and Zhonghai Ma. An adaptive-order particle filter for remaining useful life prediction of aviation piston pumps. Chinese Journal of Aeronautics, 2018, 31(5): 941-948.

5[J] Zhonghai Ma, Shaoping Wang, Chao Zhang, Tomovic, M. M and Tongyang Li. A Load Sequence Design Method for Hydraulic Piston Pump Based on Time-Related Markov Matrix. IEEE Transactions on Reliability, 2018, 67(3): 1237-1248.

8[J] Tongyang Li, Jian Shi, Shaoping Wang, Enrico Zio and Zhonghai Ma. A Numerical Approach for Predicting the Remaining Useful Life of an Aviation Hydraulic Pump Based on Monitoring Abrasive Debris Generation. Mechanical Systems and Signal Processing.

1[C] Tongyang Li, Shaoping Wang, Jian Shi and Zhonghai Ma. Degrading process simulation of aviation hydraulic pump with lifetime experiment data based on hidden semi-Markov model, 12th IEEE Conference on Industrial Electronics and Applications (ICIEA). IEEE, 2017: 624-629.

Compared with service life prediction or whole life prediction, the characteristic of residual service life prediction is that the research object may have experienced unknown service process and experienced unknown degradation process. Therefore, the premise of residual service life prediction is accurate current state estimation. Due to various uncertainties that may lead to the degradation of the system during the use of the system, these uncertainties affect the matching accuracy of the model and data used for the prediction of the remaining service life. The core of state estimation is to eliminate the impact of these uncertainties. In the research, the uncertainty is usually summarized as model uncertainty and measurement uncertainty, and it is assumed that the uncertainty obeys the known definite distribution.

In this chapter, firstly, a state estimation method based on adaptive order particle filter is proposed based on particle filter, and the life of a certain type of hydraulic pump is predicted based on the existing empirical model and data. Then, combined with the abrasive debris particle generation model and aliasing signal detection method proposed in the previous chapters, a prediction framework for the remaining wear life of hydraulic pumps based on monitoring debris particle detection was proposed, and combined with the state estimation method proposed in this chapter, the prediction results of hydraulic pump wear life were obtained.

4.1 Adaptive-order particle filter based prognostics

4.1.1 Basic algorithm of particle filter based prognostics

Particle filter has become an attractive state estimation method for its capability of accounting for the randomness of the process and the noise affecting measurements. The main idea of PF is that particles are used to describe a probability distribution instead of an analytical expression. To define a system, consider a state sequence $x_{0:k} = \{x_0, x_1, ..., x_k\}$ and its corresponding measurement sequence $y_{0:k} = \{y_0, y_1, ..., y_k\}$, where k denotes a time metric. The state space model is commonly defined as

$$x_k = f(x_{k-1}, u_k) \tag{4-1}$$

$$y_k = h(x_k, v_k) \tag{4-2}$$

where f and h represent the state transition function and measurement function, respectively. $x_k \in \mathrm{R}^{n_x}$ is the state to be estimated, and $y_k \in \mathrm{R}^{n_y}$ is the observation, where n_x and n_y are the dimensions of the states and the observations. $u_k \in \mathrm{R}^{n_x}$ and $v_k \in \mathrm{R}^{n_y}$ are independent, identically distributed noises with known probability densities.

According to the Bayes' rule, the posterior probability density can be described as

$$p(x \mid y) = \frac{p(y \mid x)p(x)}{p(y)} = \frac{p(y \mid x)p(x)}{\int p(y \mid x)p(x)\mathrm{d}x} \tag{4-3}$$

where the requirement is that $p(y) > 0$, and $p(x)$ is the probability of x. The state estimation problem is to solve the probability density function (PDF) $p(x_k \mid y_{0:k})$. $p(x_k \mid y_{0:k})$ contains all the information about the state x_k, which is inferred from the observations $y_{0:k} = \{y_0, y_1, ..., y_k\}$. $p(x_0) = p(x_0 \mid y_0)$ is the initial distribution of the states and is known previously. The PDF $p(x_k \mid y_{0:k})$ is obtained recursively from the prediction step and the update step.

In the prediction step, the system model is used to obtain the prior PDF of the state at time k by the Chapman–Kolmogorov equation as follows:

$$\begin{aligned} p(x_k \mid y_{0:k-1}) &= \int p(x_k \mid x_{k-1}, y_{0:k-1})p(x_{k-1} \mid y_{0:k-1})\mathrm{d}x_{k-1} \\ &= \int p(x_k \mid x_{k-1})p(x_{k-1} \mid y_{0:k-1})\mathrm{d}x_{k-1} \end{aligned} \tag{4-4}$$

in which $p(x_k \mid x_{k-1})$ is defined by the system model Eq. (4-1). $p(x_{k-1} \mid y_{0:k-1})$ has been obtained by the update step in last loop, and $p(x_0) = p(x_0 \mid y_{0:0})$ is known previously.

In the update step, a new observation y_k is available and can be used to update the prior PDF of the state via Bayes' rule as follows:

$$p(x_k \mid y_{0:k}) = \frac{p(y_k \mid x_k)p(x_k \mid y_{0:k-1})}{p(y_k \mid y_{1:k-1})} \tag{4-5}$$

where $p(y_k \mid y_{1:k-1})$ is the normalizing constant,

$$p(y_k \mid y_{0:k-1}) = \int p(y_k \mid x_k)p(x_k \mid y_{0:k-1})\mathrm{d}x_k \tag{4-6}$$

and $p(y_k \mid x_k)$ can be obtained by Eq. (4-2).

For the system defined by Eqs. (4-1) and (4-2), f and h are usually nonlinear, which leads to a difficulty in obtaining an analytic solution for the posterior distribution $p(x_k \mid y_{0:k})$. A PF approximates it with a set of samples (particles) $\{x_{0:k}^i, i = 1, 2, ..., N\}$

where N is the particle number. The initial particles are drawn from $p(x_0)$. To address the problem of sampling from the posterior distribution, importance sampling is employed. Samples can be easily drawn from an importance distribution $q(x_{0:k} \mid y_{0:k})$, and the importance weight for each particle can be calculated by

$$\omega_k^i = \frac{p(x_{0:k} \mid y_{0:k})}{q(x_{0:k} \mid y_{0:k})} \propto \omega_{k-1}^i \frac{p(y_k \mid x_k^i)\, p(x_k^i \mid x_{k-1}^i)}{q(x_k^i \mid x_{k-1}^i, y_k)} \tag{4-7}$$

where ω_k^i denotes the weight of particle i at time k. Thereby, the posterior distribution $p(x_k \mid y_{0:k})$ can be approximated by particles as

$$p(x_k \mid y_{0:k}) \approx \sum_{i=1}^{N} \omega_k^i \delta(x_k - x_k^i) \tag{4-8}$$

where δ is the Dirac function.

4.1.2. Particle filter with a high-order model

Note that the state space model given by Eqs. (4-1) and (4-2) is described by a Markov model of first order. Actually, the system model may be given by

$$x_k = f(x_{k-1}, x_{k-2}, ..., x_{k-p}, u_k) \tag{4-9}$$

in which the system is described as a p-order model. The PF framework still takes hold and is proven as follows.

In the prediction step, the prior PDF of the state at time k is

$$\begin{aligned} p(x_k \mid y_{0:k-1}) &= \int\int ... \int p(x_k, x_{k-1}, ..., x_{k-p} \mid y_{1:k-1}) \mathrm{d}x_{k-1} \mathrm{d}x_{k-2} ... \mathrm{d}x_{k-p} \\ &= \int\int ... \int p(x_k \mid x_{k-1}, x_{k-2}, ..., x_{k-p}, y_{0:k-1})\, p(x_{k-1} \mid y_{0:k-1}) ... p(x_{k-p} \mid y_{0:k-1}) \mathrm{d}x_{k-1} \mathrm{d}x_{k-2} ... \mathrm{d}x_{k-p} \\ &= \int\int ... \int p(x_k \mid x_{k-1}, x_{k-2}, ..., x_{k-p})\, p(x_{k-1} \mid y_{0:k-1}) ... p(x_{k-p} \mid y_{0:k-p}) \mathrm{d}x_{k-1} \mathrm{d}x_{k-2} ... \mathrm{d}x_{k-p} \end{aligned} \tag{4-10}$$

where $p(x_k \mid x_{k-1}, x_{k-2}, ..., x_{k-p})$ can be obtained by Eq. (4-9), and $p(x_{k-p} \mid y_{0:k-p})$ is obtained by the update step in loop $k-p$. $p(x_0) = p(x_0 \mid y_{0:0})$ is known previously.

In the update step, with a new observation y_k, the posterior PDF of the state can be calculated by Eqs. (4-5) and (4-6). Thus, the Bayesian solution is capable to be

used in a high-order model. The proof of the applicability of importance sampling is as follows.

The original definition of the importance weight of a particle is

$$\omega_k^i = \frac{\sigma(x_{0:k})}{q(x_{0:k})} \tag{4-11}$$

where $\sigma(x_{0:t})$ is the joint probability distribution as

$$\sigma(x_{0:t}) = p(x_{0:t}, y_{0:t}) \tag{4-12}$$

which means that the importance weight is the ratio between two distributions. It can be deduced as

$$\begin{aligned} \omega_k = \frac{\sigma(x_{0:k})}{q(x_{0:k})} &= \frac{\sigma(x_{0:k})}{q(x_k \mid x_{0:k-1}) q(x_{0:k-1})} \times \frac{\sigma(x_{0:k-1})}{\sigma(x_{0:k-1})} \\ &= \omega_{k-1} \times \frac{\sigma(x_{0:k})}{q(x_k \mid x_{0:k-1}) \sigma(x_{0:k-1})} \end{aligned} \tag{4-13}$$

Substitute Eq. (4-12) into Eq. (4-13), and then

$$\begin{aligned} \omega_k &= \omega_{k-1} \times \frac{p(x_{0:k}, y_{0:k})}{q(x_k \mid x_{0:k-1}) \sigma(x_{0:k-1})} \\ &= \omega_{k-1} \times \frac{p(y_k \mid x_{0:k}, y_{0:k-1}) p(x_{0:k}, y_{0:k-1})}{q(x_k \mid x_{0:k-1}) \sigma(x_{0:k-1})} \\ &= \omega_{k-1} \times \frac{p(y_k \mid x_{0:k}) p(x_k \mid x_{0:k-1}, y_{0:k-1}) p(x_{0:k-1}, y_{0:k-1})}{q(x_k \mid x_{0:k-1}) \sigma(x_{0:k-1})} \\ &= \omega_{k-1} \times \frac{p(y_k \mid x_{0:k}) p(x_k \mid x_{0:k-1})}{q(x_k \mid x_{0:k-1})} \end{aligned} \tag{4-14}$$

Take an optimal of $q(x_k \mid x_{0:k-1})$ as $q(x_k \mid x_{0:k-1}) = p(x_k \mid x_{0:k-1}, y_k)$, and then Eq. (4-14) can be described as

$$\omega_k = \omega_{k-1} \times \frac{p(y_k \mid x_{0:k}) p(x_k \mid x_{0:k-1})}{p(x_k \mid x_{0:k-1}, y_k)} \tag{4-15}$$

For each particle, the importance can be obtained by

$$\omega_k^i = \omega_{k-1}^i \times \frac{p(y_k \mid x_{0:k}^i) p(x_k \mid x_{0:k-1}^i)}{q(x_k^i \mid x_{0:k-1}^i, y_k)} \tag{4-16}$$

Then the importance sampling process is proven to be effective in a high-order

model. The resampling step changes the importance sampling weight to be equal by adjusting the number of the particles like

$$x_{k-1}^{ij} \sim \omega_{k-1}^{i} q(x_k^i \mid x_{0:k-1}^i, y_k) \tag{4-17}$$

where j is the new particle index after resampling, and $x^{ij} \in \{x^i, i = 1, 2, ..., N\}$. Substituting Eq. (4-17) into Eq. (4-16) yields

$$\omega_k^i = \frac{p(y_k \mid x_{0:k}^i) p(x_k \mid x_{0:k-1}^{ij})}{q(x_k^i \mid x_{0:k-1}^{ij}, y_k)} \tag{4-18}$$

By a condensation filter, take a sub-optimal of q as $q(x_k^i \mid x_{0:k-1}^{ij}, y_k) \approx p(x_k^i \mid x_{0:k-1}^{ij})$. The weighting function would be like

$$\omega_k^i = p(y_k \mid x_{0:k}^i) \tag{4-19}$$

The posterior distribution can be approximated by Eq. (4-8).

4.1.3 Adaptive-order particle filter prediction framework

A general PF uses a fixed dynamic model to estimate system states. In fact, it is difficult to build a dynamic model for a piston pump analytically. The complicated system's degrading mechanism is still unknown whose model is usually built empirically or built by data-driven models. Models built like these might not be guaranteed to accord with the actual degrading process, which means that updating the model is necessary under such a circumstance.

According to the return oil flow data shown in Figure. 50, the curves of return oil flow are not monotonously increasing so that sometimes a decline appears and lasts for a few hours. The most importance in a PF is to ensure the accuracy of the prior distribution. However, a first-order data-driven model could not deal with such unsmooth data. Take the hypothetical sequence shown in Figure. 51 for an example. If the dynamic model is first-order, the estimated value is more likely to show at x_{k+1}. If a second-order model is taken into consideration, x'_{k+1} seems to be a more reasonable

value. A high-order model could contain more recent information. A short-term trend by the latest states is more likely to reflect the possible states of next time steps. Note that when the parameters of all the high-order variables are equal to zero, the model is a first-order model.

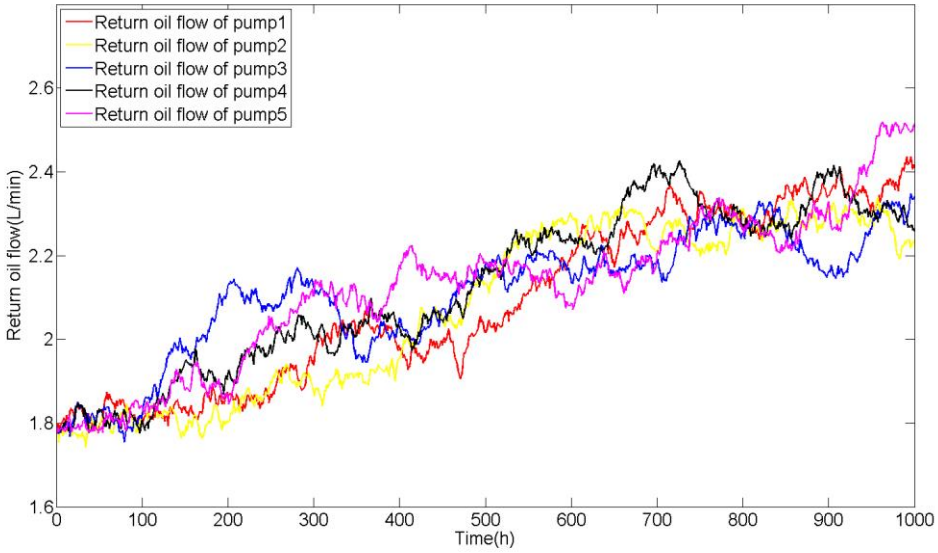

Figure. 50 Return oil flow.

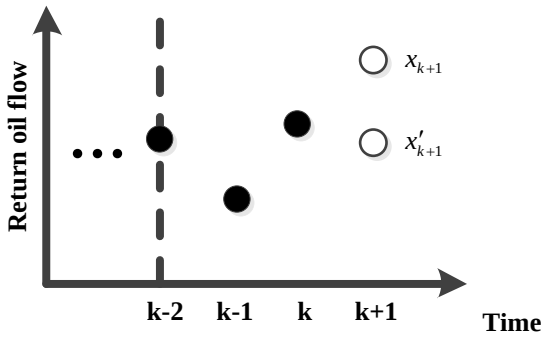

Figure. 51 Hypothetical sequence.

Based on the theory mentioned above, we propose an adaptive-order particle filter method, which can be applied to a dynamic model with a current time state related to the states at not only last time step but also several time steps previously which can be described by Eqs. (4-9) and (4-2). The adaptive order means that the order number of the dynamic model is updated at each time step adaptively. The main difference between a general PF and a high-order particle filter is the prediction step during that

to predict the state at time k, if the order of the dynamic model is $O_k = p$, then the states of the particles $\{x_{k-p+1}^i, x_{k-p+2}^i, ..., x_{k-1}^i\}$ should be stored without a resampling step. $\{O_{0:k}\}$ is the order sequence of the updated dynamic model. Thus a recursive function instead of a one-step function is applied to sampling particles from the sub-optimal of q, which is

$$x_k^i \sim p(x_k^i \mid x_{k-1}^i, x_{k-2}^i, ..., x_{k-p+1}^i) \tag{4-20}$$

An empirical or data-driven model is built according to the historical data firstly. To fit a new observation sequence, parameters of the model are usually modified accordingly. The model may already be accurate enough to describe the trend until time k, when a new data comes. Without changing the form of the original model, the adaptive-order framework re-determines the order number of the model by calculating the accumulated errors. If a higher-order model is calculated to be more fitted, the order number is then updated. By rebuilding the model in a higher-order form, the short-term trend is likely to be more accurate. The adaptive-order framework is shown in Figure. 52.

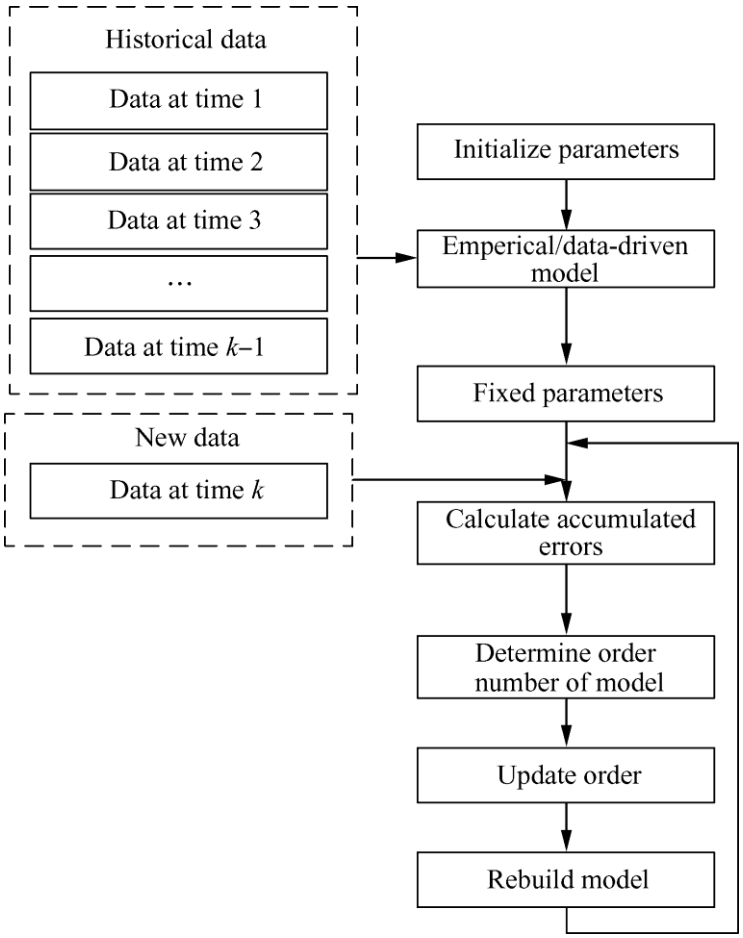

Figure. 52 Adaptive-order framework.

In the proposed model, the adaptive-order model is embedded in the PF measurement equation. The flow chart of the proposed updated-order particle filter is depicted in Figure. 53, and its main steps are as follows:

(1) Initialization step. The initial model $x_k = f_0(x_{k-1}, x_{k-2}, ..., x_{k-p_0}, u_k)$ is built by the historical data, in which p_0 is the order number of the model. The number of particles N is set. The particles and their weights are initialized as $\{x_i^0 = x_0 + u_0, \omega_i^0 = \frac{1}{N}\}_{i=1}^N$, where u_0 is the obeyed uniform distribution.

(2) For $k = p, p+1, \cdots$

a) Calculate the prior estimation by the current model $x_k = f_{k-1}(x_{k-1}, x_{k-2}, ..., x_{k-p_{k-1}}, u_k)$, which is described by the particles: x_k^i. f_{k-1} is the

updated state model.

b) When a new observation y_k arrives, update the weight of each particle: $\omega_k^i = p(y_k \mid x_{0:k}^i)$.

c) Normalize the weight of each particle: $\omega_k^i = \omega_k^i / \sum_{j=1}^{N} \omega_k^j$.

d) Resampling the particles by the weight.

e) Update the order number of the model and get a new current model $x_k = f_k(x_{k-1}, x_{k-2}, ..., x_{k-p_k}, u_k)$.

(3) Output the predicted states sequence: $\hat{x}_k = \sum_{i=1}^{N} \hat{x}_k^i / N$, where $\hat{x}_k^i$ is the estimated value of x_k^i.

The parameters of the initial model will not be as important as the form of the model for that the parameters from the historical data will be replaced by the parameters for the new data sequence by the model updating procedure. The model form $f_{0:k}$ is not modified and will be used in the prediction step. When there is no observation arriving at time $k+1$, the model is fixed, and the weights of the particles will not change. To get the remaining wear life, the current dynamic model is the only dependence, which means that the recursive state in the future x_{k+t} is obtained by

$$p(x_{k+t} \mid x_{0:k+t-1}) = p(x_{k+t} \mid x_{0:k}, y_{0:k}) = \int\int ... \int \prod_{i=k+1}^{k+t} p(x_i \mid x_{i-1}) p(x_k \mid y_{0:k}) dx_k dx_{k+1} ... dx_{k+t-1} \tag{4-21}$$

where t is the step of time that $x_{k+t} \geq \text{Threshold(return oil flow)}$. The distribution of a piston pump's Remaining wear life T_{RWL} is defined as

$$p(T_{\text{RWL}} \mid y_{0:k}) = p(t \mid y_{0:k}) \tag{4-22}$$

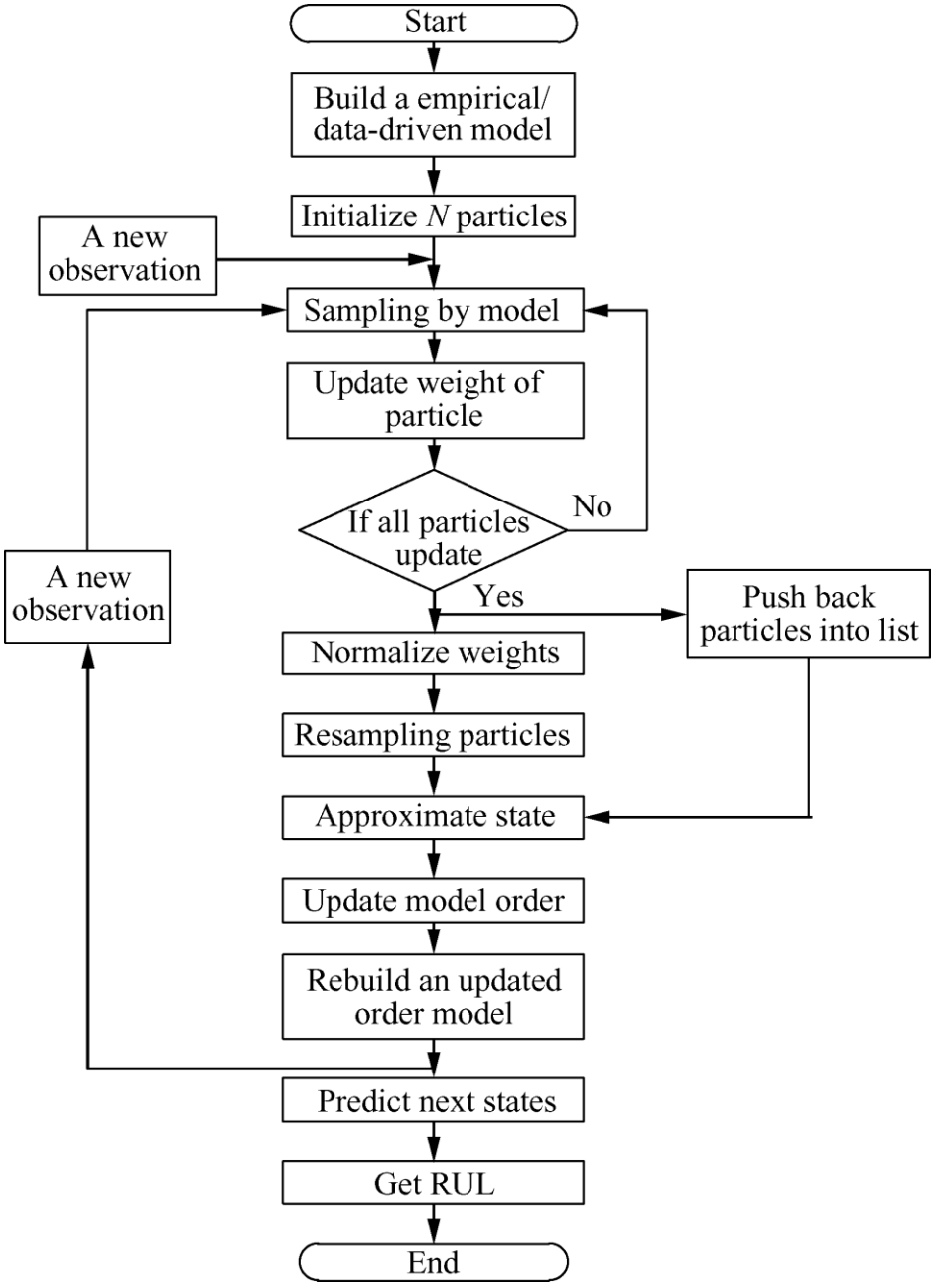

Figure. 53 Flow chart of the AOPF.

4.1.4 Example verification

In this section, data collected by a full-life experiment for a certain type of piston pump are used to demonstrate the forecasting performance of the proposed AOPF algorithm. The return flow data were measured by a turbine flow sensor installed on the return oil pipe of a pump. The work operation of the pump was full output flow by

which an accelerated wear process was adopted so that the cost could be reduced. The flow data were recorded every hour by the same measurement system.

Based on the historical data, a gray model GM (1,1) is commonly used as the data-driven model for a prediction of the piston pump. At least four points are needed to initial the model which means that the minimum order number of a GM (1,1) is 4. By accumulating the raw sequence $X^{(0)}=\{x_0,x_1,...,x_k\}$, the accumulated sequence $X_k^{(1)}=\sum_{i=0}^{k}x_i, k=0,1,2,...$ is used to fit $\frac{\mathrm{d}x_k^{(1)}}{\mathrm{d}t}+ax_k^{(1)}=b$ by

$$\begin{bmatrix} a \\ b \end{bmatrix}=(\boldsymbol{B}^{\mathrm{T}}\cdot\boldsymbol{B})^{-1}\cdot\boldsymbol{B}^{\mathrm{T}}\cdot\boldsymbol{Y} \tag{4-23}$$

where

$$\boldsymbol{B}=\begin{bmatrix} -0.5\times(x_1^{(1)}+x_0^{(1)}) & 1 \\ -0.5\times(x_2^{(1)}+x_1^{(1)}) & 1 \\ \vdots & \vdots \\ -0.5\times(x_k^{(1)}+x_{k-1}^{(1)}) & 1 \end{bmatrix} \tag{4-24}$$

and

$$\boldsymbol{Y}=[x_1^{(1)} \quad x_2^{(1)} \quad ... \quad x_k^{(1)}]^{\mathrm{T}} \tag{4-25}$$

The data shown in Figure. 54 are the experimental results of the return oil flow of a certain pump. When the return oil flow reaches 2.8 L/min, the wear condition of the pump is considered to be the threshold of the failure of wear according to the design parameters. The trend of the return oil flow is increasing except some parts of reduction, which means that the leakage of the pump is increasing and gradually leads to an incapability for the pump to provide high-pressure hydraulic power for the actuation system.

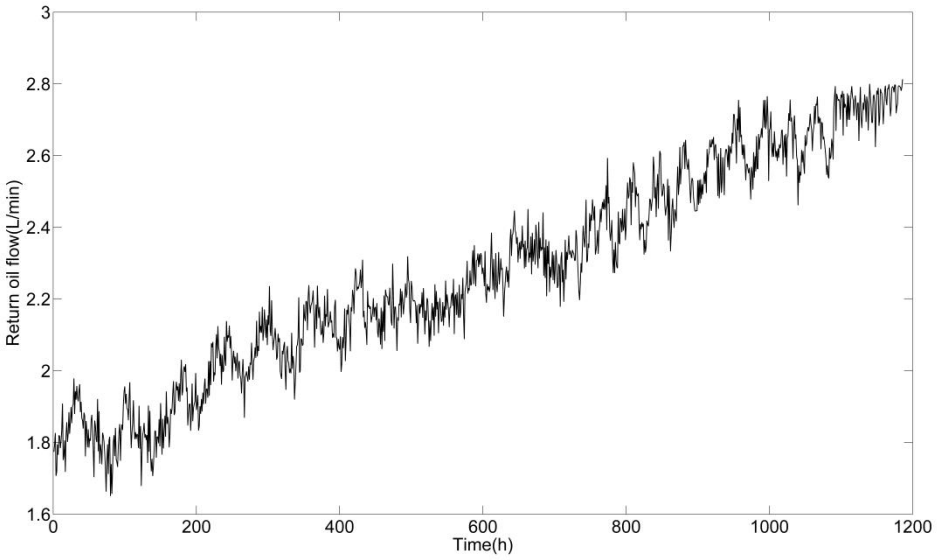

Figure. 54 Experimental results of the return oil flow.

Figure. 55 shows the short-term prediction results by the GM (1,1) and the proposed AOPF method. Both of the algorithms show good performance in the one-step prediction. Each point of the curves stands for a prediction obtained by the prior data. The gray method fits well while the AOPF shows a better result which is demonstrated in Figure. 56. The red curve and the blue curve indicate the mean square errors (MSEs) of gray prediction and AOPF prediction, respectively. To get Figure. 56, each point is calculated by accumulating all the MSE of the previous points. Obviously, the MSE of the AOPF prediction is lower than that of the gray prediction after 47 time steps. Raw data of the return oil flow illustrate a large fluctuation at the beginning during that from 20 hours the return oil flow continues to fail which impacts the performance of the method. However, after a few steps, the AOPF performs a good anti-interference characteristic. The blue curve keeps lower than the red curve, which means that the error of the AOPF prediction is smaller than that of the gray prediction and the noise is depressed after enough prior knowledge accumulated.

The adaptive-order number of each step is displayed in Figure. 57. The order numbers show a polarization that most of the order numbers are very small and large order numbers usually appear and last for some time. Comparing Figure. 55 to Figure.

57, a strong connection appears between the large order number and the decline of the raw data. When the trend is rising, the adaptive order number is stabilized at a low level. To adapt the unusual trend, the AOPF matches with a higher-order model adaptively.

The characteristics of the adaptive-order numbers shown in Figure. 57 provide an optimization strategy. In a rising stage, the best order number occurs between 0 and 40. Then if the trend of the sequence is determined, the computation burden can be largely declined. The strategy shows a greater significance with an increase of the time. In a later period, the resolving time is impacted mainly by the time on MSE calculation. The strategy could keep the computing time rise steadily.

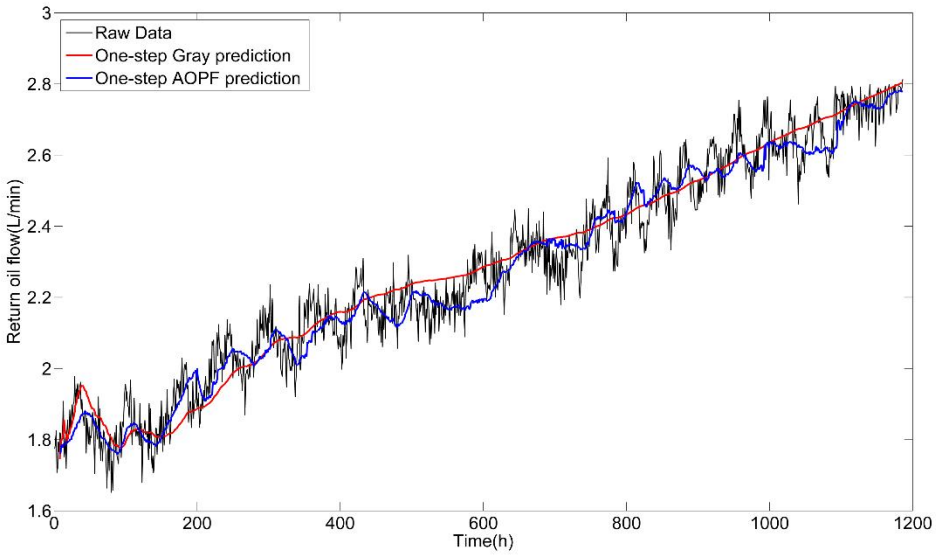

Figure. 55 Short-term prediction comparison.

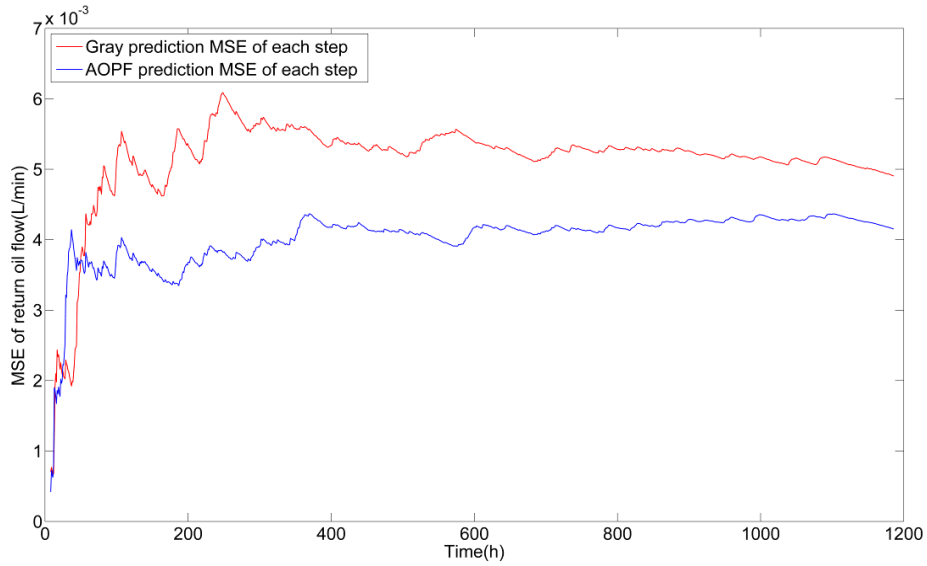

Figure. 56 MSEs of return oil flow comparison between grey prediction and AOPF prediction.

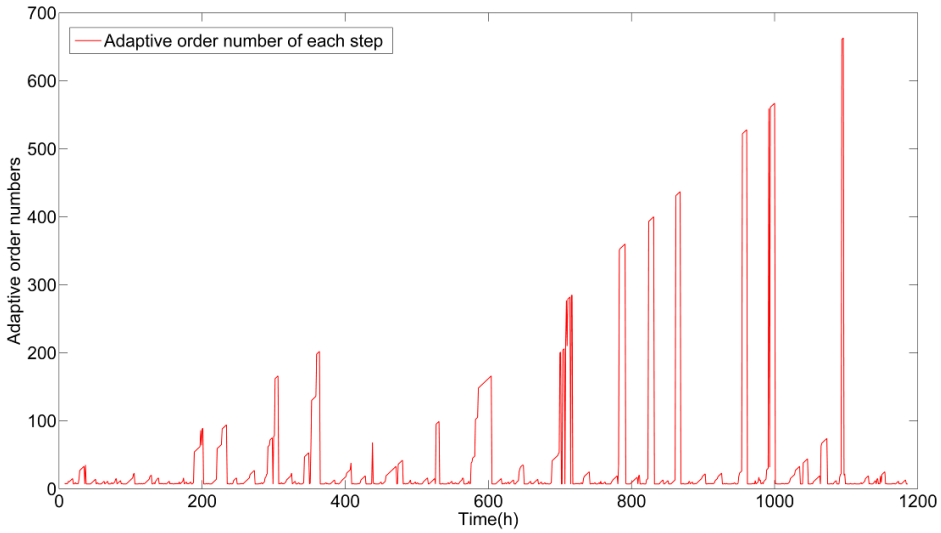

Figure. 57 Adaptive-order number of the AOPF.

However, many functions can provide a high precision in the short-term prediction. What challenges is the long-term prediction. In order to verify the performance of a long-term prediction, the raw data are divided into two sets. One is used for model adaption and the other for proving. Taking the first 600 points as the training data, a gray model sequence is generated. Meanwhile, a gray model initialized by the first 4 points are updated adaptively by the AOPF. Long-term prediction results by GM (1,1)

and the proposed AOPF method are shown in Figure. 58. The actual failure time of the pump is 1186 hours. By gray forecasting with GM (1,1), the time that reaches the threshold is 1103 hours, which means that the error is 73 hours. Whereas the life predicted by the AOPF is 1144 hours and the error is 42 hours, which means that the error is reduced by 42.5%. Note that the precision of the AOPF is affected by the number of particles. More particles lead to a heavier computation burden. In the proposed stage, the number of the particles is 300. In the long-term prediction, the measurement error and the system error are accumulated in the data-driven model. The AOPF can promote the long-term prediction accuracy through filtering the noise of each measurement point.

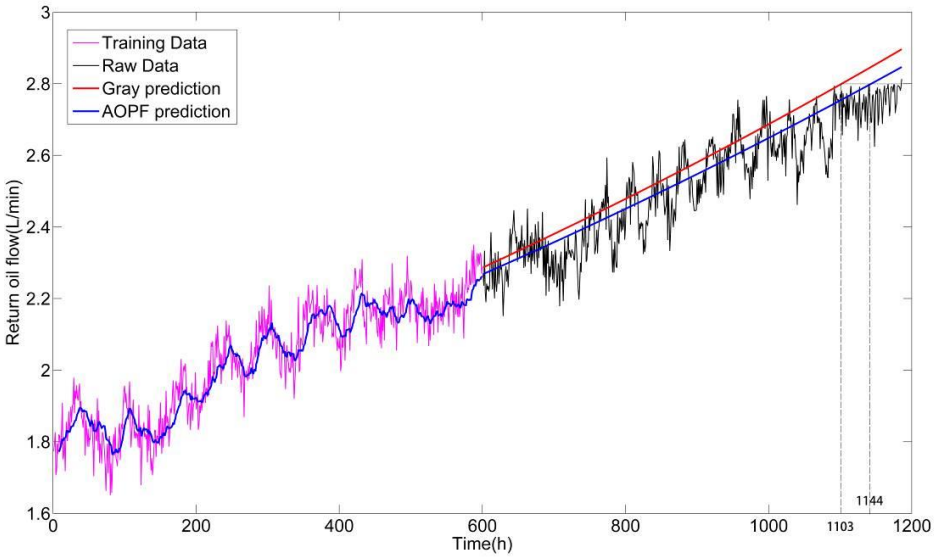

Figure. 58 Long-term prediction comparison.

The order number influences the accuracy of the prediction. Although the AOPF only takes the model which fits best, the relationship between the order number and the performance of that is expected to be known so that an optimization could be applied for a reduction of time cost. By fixing the order number of the AOPF, the results of a 7-order model and a 20-order model are shown in Figure. 59, and the performance is listed in TABLE 9. The 20-order model shows a better performance than that of the 7-

order model. The errors of the 7-order model and the 20-order model are 68 hours and 55 hours, respectively. As it is analyzed above, a higher-order model may fit the actual data better.

TABLE 9 Performances of 7-order and 20-order models

Type	7-order model	20-order model
MSE of return oil flow (L/min)	0.0091	0.0060
RMSE of return oil flow (L/min)	0.0953	0.0775

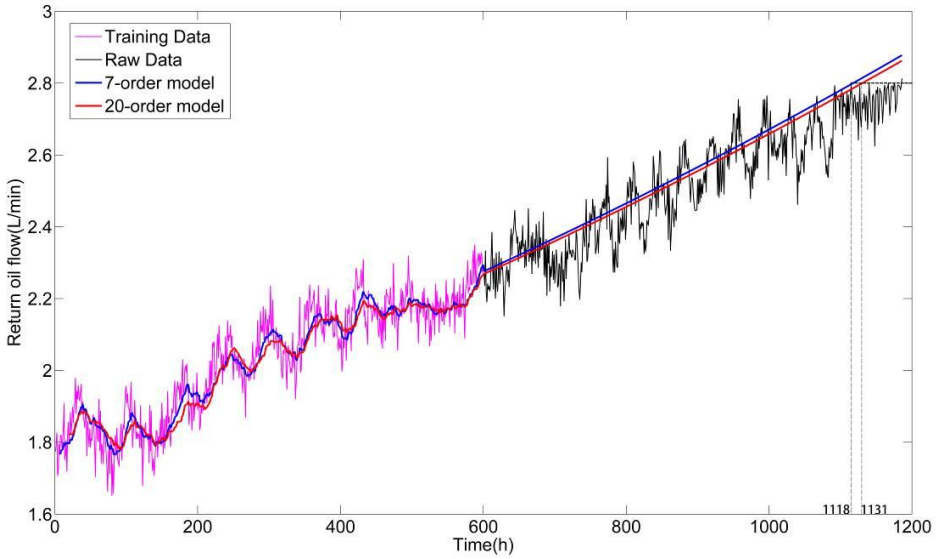

Figure. 59 Different order models' prediction results comparison.

For an intuitive understanding of the relationship between the order number and the performance, Figure. 60 shows the MSEs of different order number models at time 600 h. The order number is from 7 to 60. With the order number increasing, the trend of the MSE is decreasing. The lowest point of the curve occurs near 30 after which the curve shows a fluctuation around 5.5×10^{-3} L/min. It is not that the higher the order number is, the lower the error is. By taking an appropriate order, the error can be reduced by more than 50% which will increase the precision of the remaining wear life prediction accordingly.

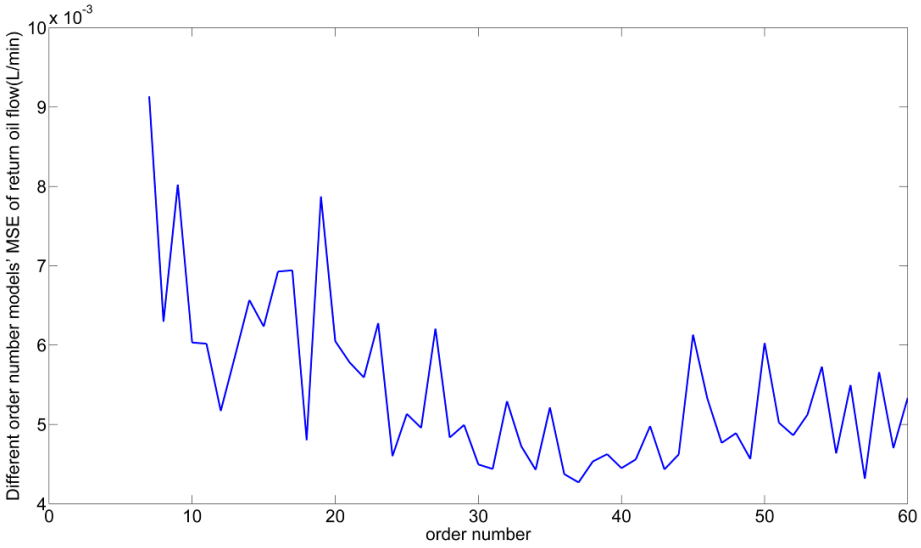

Figure. 60 Different order number models' MSEs of the return oil flow.

4.2 Remaining wear life prediction of hydraulic pump based on monitoring abrasive debris generation

4.2.1 Partition-integration remaining wear life prediction framework for aviation axial piston pumps

Wear of the friction pairs is considered the main degradation mechanism of an aviation piston pump, whose typical structure is shown in Figure. 61. The rotation of the piston barrel, which is driven by motors or engines through the shaft, actuates the suction and discharge movements of the pistons. The relative movements between the contact pairs unavoidably bring about material loss. As the material loss increases, the displacement between the two contact surfaces becomes larger, which results in leakage. After a period of degradation, the pump can no more provide the required pressure and, hence reaches the end of life.

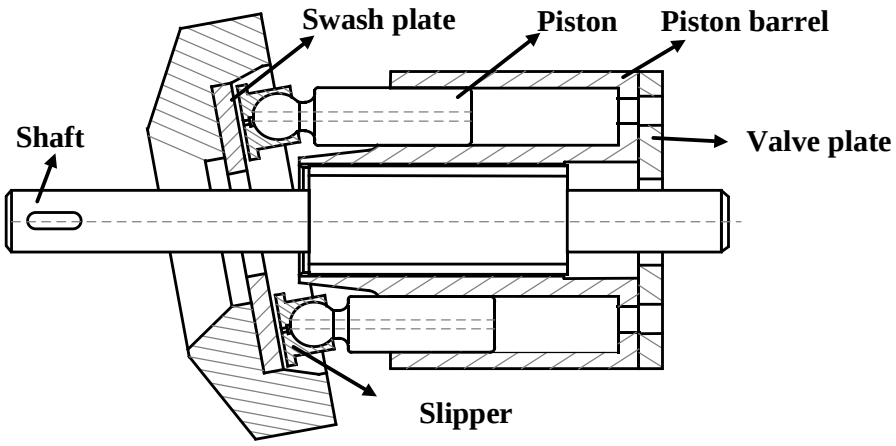

Figure. 61 A typical structure of axial piston pump

In practice, the degradation process is uncertain and, thus, it is typically modeled as a stochastic process. One source of uncertainty is the complex work conditions, since vibration, thermal factors and flow ripples may all influence the wear process. Another source is related to the randomness of the elements, specifically the rough surfaces of contact pairs: with same roughness, the profiles of the rough surfaces may still be different. In this work, abrasive debris is selected as the health indicator. Research studies [12, 132] indicate that features (quantity, size, shape and composition) of wear debris show a strong relationship with wear characteristics (severity, rate, mode and source). This relationship is modeled in this work by the ADGM presented in Chapter 2. To address uncertainty, a partition-integration method is employed. Each component of a friction pair, e.g. valve plate of the valve plate/piston barrel pair, is divided into small fragments. For each small fragment, the applied load is solved at macroscale and assumed constant, whereas the microscopic profiles are uncertain. For a small fragment with given microscopic profile, wear debris features can be estimated by ADGM. Global roughness of the contact surfaces is, then, estimated from local samples, artificial rough surfaces with same roughness but different profiles are generated and probabilistic wear debris features can be obtained by MC simulation. The probabilistic wear debris features of each small fragment are then sampled by MC to obtain an integrated function for the friction pair. The probabilistic model, then, serves to generate

degradation paths for remaining wear life prediction. The proposed framework is sketched in Figure. 62.

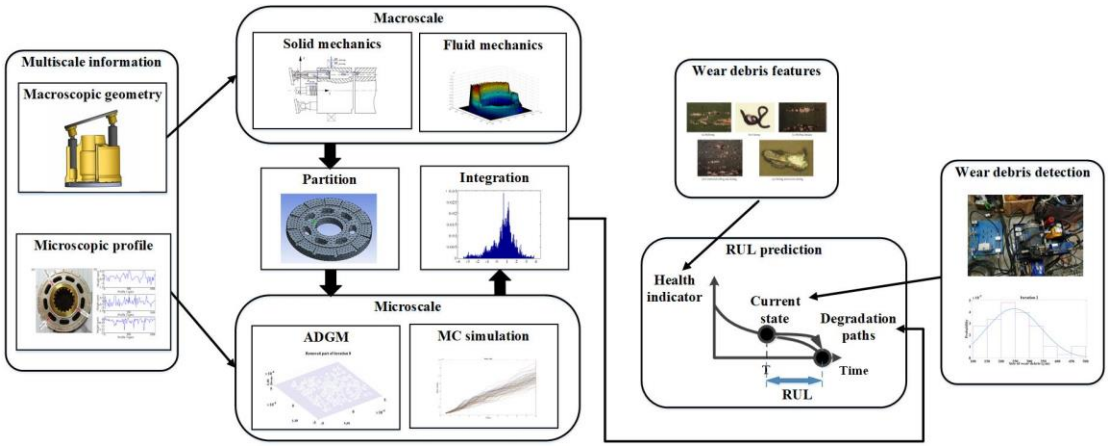

Figure. 62 Remaining wear life prediction framework with multiscale information.

A typical macroscale modeling method may start from analyzing the forces applied on each component. Combining the mechanical dynamics, the macroscale pressure distribution on each contact surface can be obtained. If the contact is under mixed lubrication, the fluid is Newtonian and the flow is assumed to be laminar flow; then, the film thickness and stress distribution can be described by Reynolds equation. Solving the equation numerically by methods like finite difference or finite element, the macroscale hydrodynamic stress distribution can be obtained. Since with different assumptions, the method to obtain macroscale stress might be different, the above macroscale modeling method is replaceable and may be replaced by other proper methods.

Similarly, a replaceable wear debris detection method is developed in this work to obtain the current state of the system. Wear debris features are obtained by a radial inductive debris detection method [13]. Measurement uncertainty may influence the accuracy of prediction. By using a hybrid method based on a band pass filter and a correlation algorithm, the signal-to-noise ratio can be improved by about 2.67 times [72]. The method is also capable of coping with potential aliasing problems, which

promotes the accuracy largely [15].

Assuming that both amount and sizes of debris can be accurately obtained by the debris detection methods, multi-dimensional information can be used for remaining wear life prediction. If the amount of debris reaches the failure threshold at $t = T_a$ and the amount of debris with size larger than the critical size s_F reaches the threshold at $t = T_s$, the real remaining wear life can be obtained

$$RWL_r = \min\left\{\left(t_k - T_a \mid t_k > T_a\right), \left(t_k - T_s \mid t_k > T_s\right)\right\} \tag{4-26}$$

where t_k is the observation time. For the proposed prediction framework, the exact failure time is not assumed known beforehand. If the debris particles are observed at $\left\{t^{(1)}, t^{(2)}, ..., t^{(k)}, ...\right\}$, where $t^{(k)}$ denotes the observed time of the k^{th} debris particle, and the probability density function (PDF) of size at $t = t^{(k)}$ is given by $f\left(S^{(k)}\right)$, where $S^{(k)} \in \left\{s^{(1)}, s^{(2)}, ...s^{(k)}\right\}$ is the set of debris sizes, then, the predicted remaining wear life RWL_p can be calculated by

$$RWL_p = \min\{\left(\frac{V_a - \sum_{i=1}^{k} s^k}{\dot{V}}\right), \left(t_l - t_k \mid (\int_{s_F}^{+\infty} f\left(S^{(l)}\right) ds \geq P_F\right)\} \tag{4-27}$$

where V_a is the failure threshold of total material volume loss, $\dot{V}$ is the wear rate and P_F is the critical probability of larger debris particles. Practically, the wear rate can be estimated by

$$\dot{V} = \frac{s^{(k)}}{t^k - t^{k-1}} \tag{4-28}$$

for good real-time performance. It may also be estimated by

$$\dot{V} = \frac{\sum_{i=1}^{k} s^k}{t^k} \tag{4-29}$$

for good stability during long-period prediction.

In this thesis, both the parameters are obtained by MC sampling from the abrasive debris features distribution of components. The abrasive debris features distribution of one component is sampled from the abrasive debris features distribution of each small fragment. In the next section, the numerical way to obtain the abrasive debris features distribution of each small fragment is introduced in detail.

4.2.2 Experimental result

In order to verify the effectiveness of the proposed method, a life cycle experiment result of a certain type of aviation piston pump [7] is tested and a grey model [87] is used as a comparison. According to the experiment result, approximately 70% of the pump leakage is caused by the wear between valve plate and piston barrel. In this case, the leakage ratio is assumed to be constant. A general structure of the friction pair is shown in Figure. 63 and its dimension parameters are listed in TABLE 10.

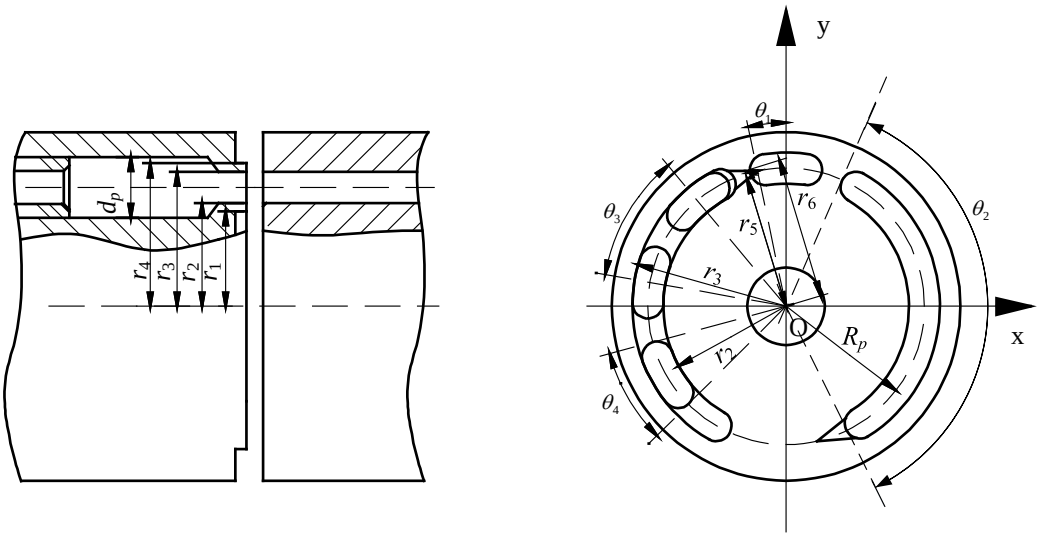

Figure. 63 Structure of the friction pair.

TABLE 10 Dimension parameters

Parameter	Value	Parameter	Value
r_1	0.0386 m	θ_1	12°
r_2	0.0436 m	θ_2	134°
r_3	0.0564 m	θ_3	40°
r_4	0.0614 m	θ_4	28°
r_5	0.0475 m	d_p	0.026 m
r_6	0.0525 m	R_p	0.0525 m

The pump works in full output flow condition. The inlet pressure is 0.15 MPa and the outlet pressure is 21 MPa. The rotation speed is 4000 r/min. Since to obtain the entire profile of the contact surfaces takes too much time, three specimens are sampled from both the piston barrel and the valve plate. The mean roughness of the specimens of the piston barrel is approximately 1.1 μm and that of the valve plate is about 1.5 μm. Then, the roughness of the initial contact surfaces is estimated according to the ISO 4287:1997 standard. For the piston barrel, the corresponding ISO grade number is N6, so the roughness is set to be 0.8 μm. Similarly, the roughness of the valve plate is set to be 1.6 μm.

According to the partition-integration framework, macroscale analysis needs to be carried out and the results are used as the input for microscale simulation. To ensure the macroscale correctness, an experimental result is employed [7]. The result shows that under steady state, the mean nominal contact area of one cycle is about 2346.3 mm^2. The macroscale stress of valve plate near inlet port and outlet port can be regarded as constant. For the part between the suction area and the extraction area, the stress follows a linear distribution from 0.15 MPa to 21 MPa. The microscale fragments with same

macroscale load generate debris following the same distribution. So all the fragments with the same macroscale pressure distribution can be regarded as one fragment with various surface profiles. However, to obtain the debris features from the remaining approximate 10% area, the computational cost is 10 times more. In order to reduce the computational cost, the condition is simplified. The macroscale pressure on half of the area is assumed to be $21\ \mathrm{MPa}$ and on the other half is assumed to be $0.15\ \mathrm{MPa}$. The relative velocities of all the fragments are set to be the mean value of boundary velocities and the temperature is assumed to be constant. Simulation parameters are listed in TABLE 11. Since the friction coefficient may be different with different surface roughness, hardness and applied loads, the value of dry friction coefficient is set to be higher than the condition of steel/steel contact based on the result of fitting the model to the experimental degradation data. It should be noted that macroscale analysis is very important and the simplification will influence the accuracy. The wear debris features are assumed to follow the same distributions when the work conditions are same. For each half area, 500 pairs of fragments with rough surfaces are sampled by ADGM. The sample results are shown in Figure. 64 (a) and the corresponding sampling distribution is shown in Figure. 64 (b). The surface area of each fragment is set to be $100\ \mu\mathrm{m}\times100\ \mu\mathrm{m}$, which contains 128×128 data points. So the radius of each DRU is approximately $0.39\mu\mathrm{m}$ and the minimum worn size is about $2.4\times10^{-19}\mathrm{m}^3$.

TABLE 11 Values of parameters for simulation

Parameter	Meaning	Value
μ_c	Dry friction coefficient	0.3
v_1	Poisson's ratio of valve plate	0.3
v_2	Poisson's ratio of piston barrel	0.3
E_1	Young's Modulus of valve plate	210GPa
E_2	Young's Modulus of piston barrel	210GPa
L_x	Length of simulation space in x direction	100 μm
L_y	Length of simulation space in y direction	100 μm
R_z	Resolution in z direction	0.39 μm
σ_{yield}	Yield stress of composite surface	355MPa
μ	Dynamic viscosity	0.013065Pa·s

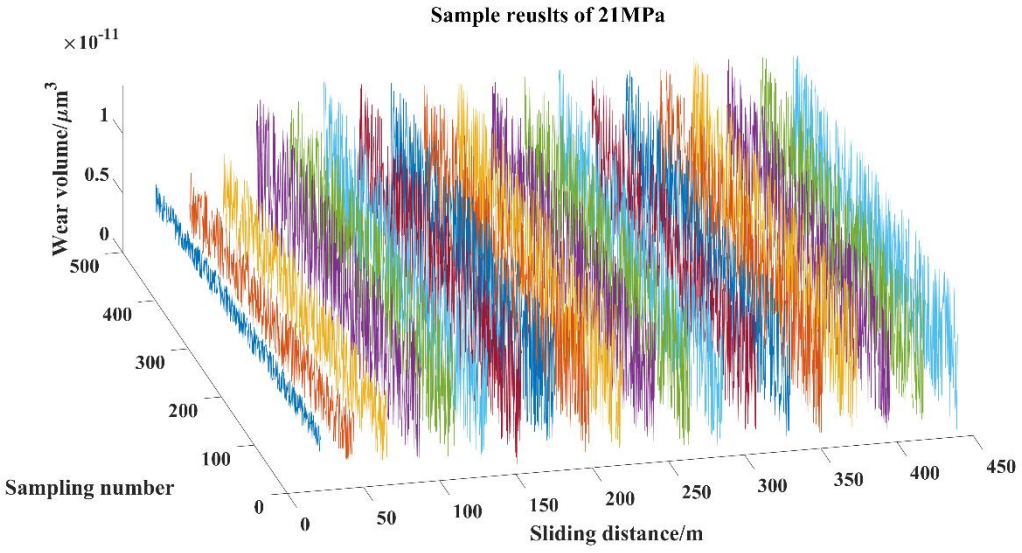

(a)

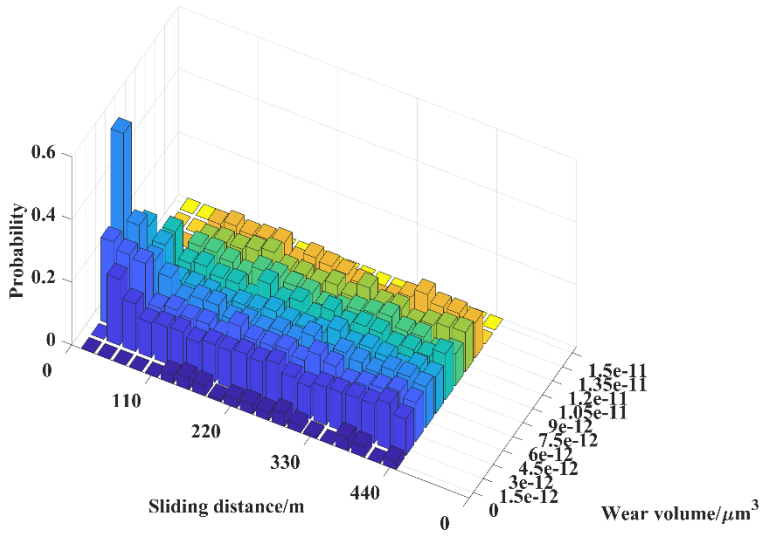

(b)

Figure. 64 Sampling results.

Then, the wear debris features of the friction pair are sampled from the fragments and the sample result for the entire friction pair is shown in Figure. 65. A simulation by finite element method (FEM) is conducted as a comparison. The simulation considers a dry sliding contact of two smooth contact surfaces. The material property and the work condition are set to be the same as those used for the partition-integration method. The simulation contains three load step. For the first step, ramped loads are applied. Wear is assumed to begin from the second step and the simulation interval is set to be twice from the third step. Archard's law is applied to calculate the total material loss. Figure. 66 (a) presents the loads and constraints of the simulation. From the total volume loss shown in Figure. 66 (b), a constant wear rate can be obtained. Generally, sliding contact under lubrication results in less material loss than dry sliding contact. So the dry sliding contact can be regarded as the upper bound of the estimation.

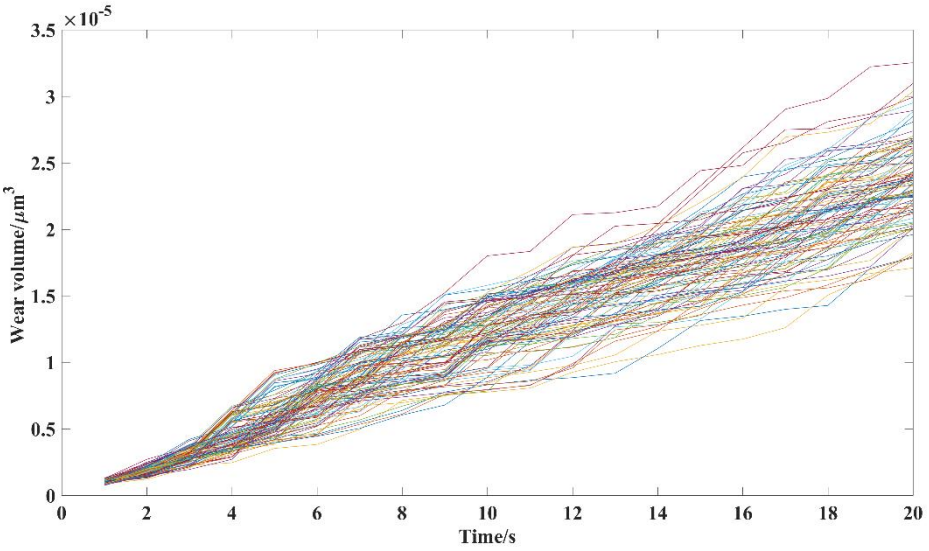

Figure. 65 Sampling result of wear volume.

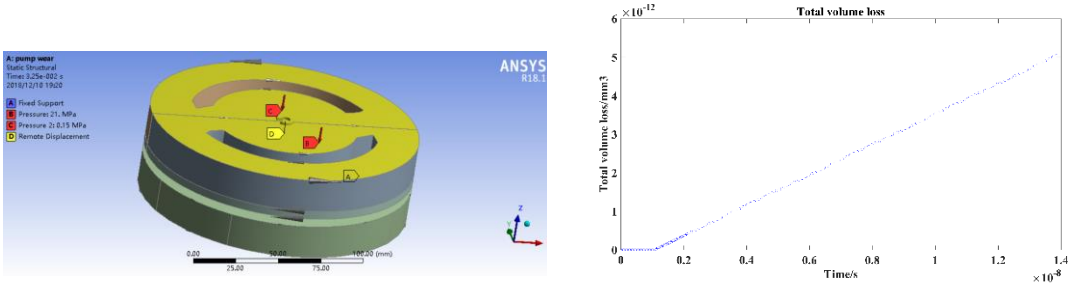

(a) (b)

Figure. 66 FEM simulation.

According to the partition-integration framework, current state needs to be obtained accurately by the measuring part. The state can be measured directly or estimated from the other signals. Due to lack of data by oil debris detection, the common used return oil flow is employed to obtain the current state. The state is assumed to be estimated accurately so that the predicting method can be verified. Here, we propose a simple method to transfer the signals to a perfectly estimated states. The return oil flow is assumed to be the total leakage of the pump. Since the leakage ratio is constant, the total leakage by the friction pair of barrel and valve plate can be obtained. If the barrel and the valve plate are parallel-shaped, the relationship between the leakage

Q_{bv} and the interval h_{bv} of the components can be described as

$$Q_{bv} = \frac{\alpha_0 h_{bv}^3 (P_{\text{out}} - P_{\text{in}})}{12\mu} \left[\frac{1}{\ln(r_2 / r_1)} + \frac{1}{\ln(r_4 / r_3)} \right] \tag{4-30}$$

where P_{in} is the inlet pressure, P_{out} is the outlet pressure and α_0 is the distribution angle of the pistons. For the FEM simulation, the wear volume is assumed to be uniformly distributed on the nominal contact area A, so the remaining wear life can be estimated by

$$RWL = \frac{h_{bv} - H_{bv}}{\tilde{\dot{V}} / A} \tag{4-31}$$

where H_{bv} is the failure threshold. If the maximum leakage is 2.8 L/min, the failure threshold is $16.79\mu\text{m}$. Similarly, the Remaining wear life prediction result by ADGM can be estimated.

GM is modeled directly by the return oil flow data, so the state is directly measured instead of estimation. In this case, GM (1,1) is used and the model can be described by

$$\frac{\mathrm{d}x_k^{(1)}}{\mathrm{d}t} + a x_k^{(1)} = b \tag{4-32}$$

where $x_k^{(1)}$ denotes the first-order accumulated sequence of the observed points. The first 200-hour data are used to train the model. The actual in-service time of the pump is 1186 hours.

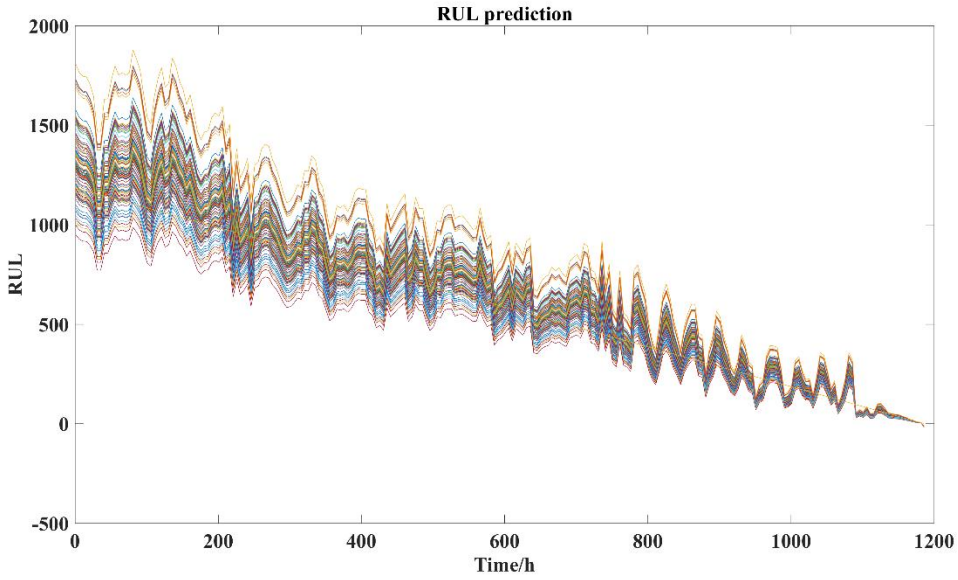

(a)

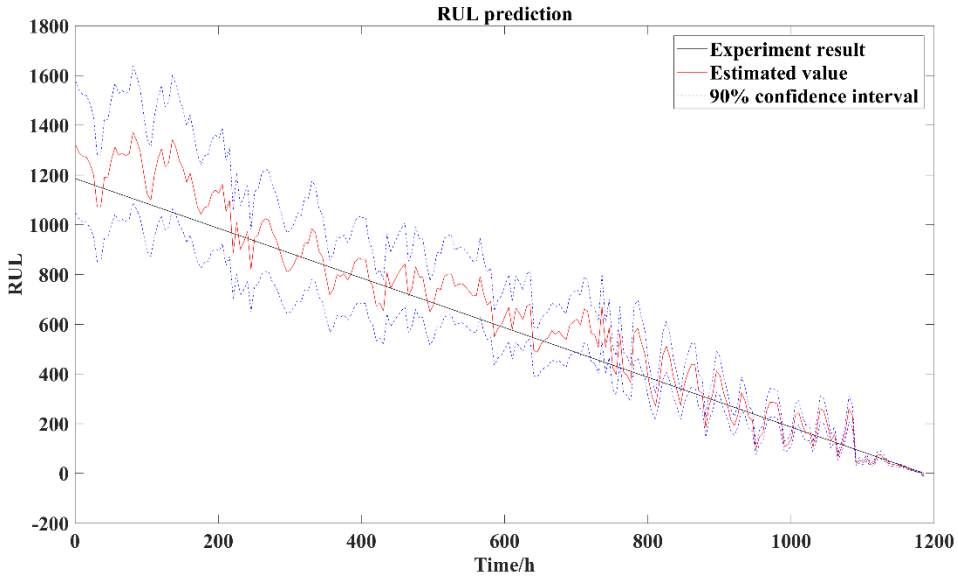

(b)

Figure. 67 Remaining wear life prediction result of ADGM.

Figure. 67 (a) shows the Remaining wear life prediction result using ADGM. We can see that ADGM provides a probabilistic prediction that at each prediction step, all possible results are presented with a certain distribution and the samples converge to the true value. In Figure. 67 (b), we show both the mean and 90% confidence interval of the Remaining wear life distribution. A comparison can be obtained as shown in

Figure. 68. As the FEM simulation considers a dry sliding contact, to compare ADGM with the extreme condition, upper and lower bounds of the prediction are plotted. The FEM result is close to the upper bound of ADGM. The upper and lower bounds cover the dry contact condition and the experiment result. Compared with GM, ADGM displays a better performance for the first 600 hours, while GM shows better performance as the data volumes grow. Because the state is estimated from the return oil flow instead of direct oil debris detection result, there is still room for improvement to the method.

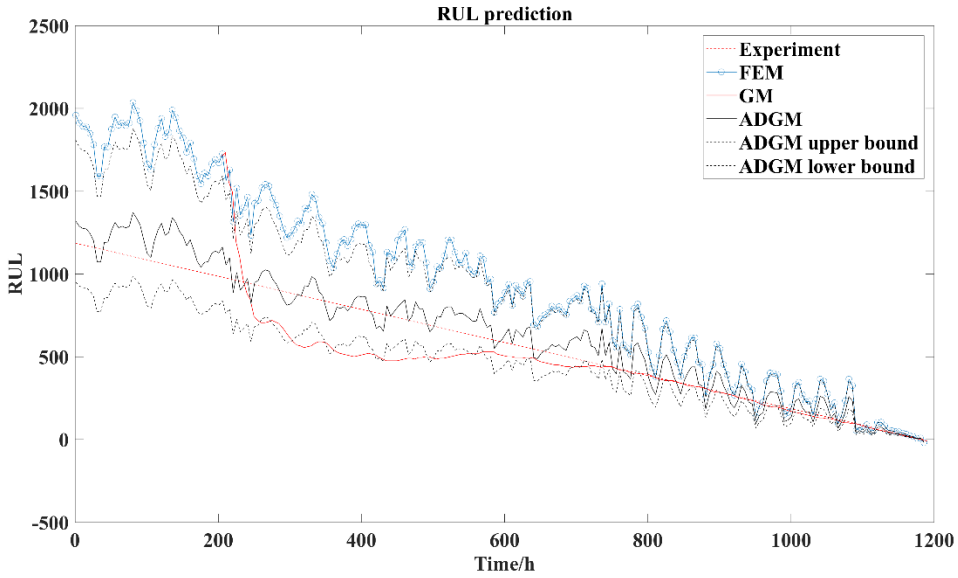

Figure. 68 Remaining wear life prediction results.

4.3 Conclusions

Degradation processes and failure mechanisms in aviation axial piston pump are complex and no analytical model exists. Meanwhile, the insufficient experimental data prevents the application of data-driven methods. Numerical modeling seems to a viable way for predicting the remaining wear life of aviation axial piston pumps. In this chapter, by ADGM, a microscale relationship is built between abrasive debris features and rough surfaces. To apply the microscale result at macroscale, a partition-integration remaining

wear life prediction framework based on MC sampling is proposed. The effectiveness of the method is verified by experimental data. The probabilistic model is able to cover the experiment result and predict the remaining wear life under extreme work conditions. At the early times, the proposed method performs better than FEM and GM. Combine with the non-intrusive and easily-installed oil debris detection method, the proposed framework is able to provide a potentially useful results in practice.

The proposed method works in a numerical way, so the accuracy is guaranteed by large computational cost. Currently, simplification has to be conducted, which limits the performance of the method. Future works concern the introduction of artificial intelligent methods to reduce the cost of computation.

5. Conclusions and future perspectives

Aiming at solving the difficulties and key problems of remaining wear life prediction of aviation piston pumps, the thesis proposed a complete approach by modeling the degradation paths, monitoring the degradation data and matching the model and data using uncertainty processing method. The thesis focuses on the mechanism of abrasive debris particles generation with given load and surface roughness, the aliasing problem of inductive debris detection sensor under high throughput and high concentration of hydraulic oil and studies the uncertainties of the state estimation using the model and data. The main research work and research conclusions can be summarized as follows:

(1) According to the elastic sliding contact mechanism of the aviation hydraulic pump under mixed lubrication condition, a numerical model was established to describe the characteristics (number, size distribution and morphology) of abrasive debris particles with given load and surface roughness. Based on conjugate gradient descent method, the numerical model was solved by solving the rough surface contact, and subsurface stress using Von-Mises fracture criterion. The abrasive debris generation model can be set at any concerning scale. The time-varying data model can be obtained by Monte-Carlo method and the accuracy of the data model was verified by qualitative and quantitative methods.

(2) For the debris detection method based on electromagnetic induction principle, when the distance of the two debris particles is very small, the induced voltage will be superimposed, which influences the detecting accuracy. In this thesis, with the help of underdetermined blind source separation method which is named degenerate unmixing estimation technique, the experiment signals are firstly processed by band-pass filter to eliminating the effect by pump vibration, electromagnetic interference from commercial electrical power and harmonic interference from three-phase electric. Then, the filtered signals are short-time Fourier transformed into time-frequency domain and

the signal separation points are estimated using two-dimensional energy histogram clustering method. By mask method the aliasing signals are separated in time-frequency domain and restored by inverse short-time Fourier transformation. Aiming at achieving the online detection, the two-dimensional energy histogram clustering method is combining with the convolution neural network. The effectiveness of the online debris particle detection method is verified by experimental data.

(3) Aiming at eliminating the matching uncertainties caused by machining process, various working conditions and measuring noises during the debris particle detection, as well as improving the accuracy of one-step state estimation and long-term life prediction, an adaptive order particle filter method was proposed based on the traditional particle filter method. The Bayesian method predict and update process using high order Markovian models are derived. Then the importance sampling and resampling particle filter method are proved to be the applicable for the high order models. By solving mean square error (MSE) of the different order models, both the model and particles distribution are updated in each iteration. The method is verified by experimental data.

5.1 Original contributions of the Ph.D. work

The main original contribution of the research lies in the development of a complete method for predicting remaining wear life of aviation axial piston pumps. Specifically, we have developed novel methods for addressing the following three issues: 1) modeling abrasive debris generation given arbitrary concerning scale and working load with fixed initial roughness, 2) restoring aliasing signals for debris feature statistics with limited detecting sensors, 3) processing uncertainties caused by modeling and measuring for a comprehensive matching result.

5.2 Future perspectives

Although the difficulties and key problems of remaining wear life prediction of

aero-hydraulic pump are presented in this thesis, the uncertainties caused by the life prediction process is deeply studied by combining the online detection method of wear debris particles, and based on these, the remaining wear life prediction framework based on monitoring abrasive debris particles detection are established, the following problems are still worth further study:

(1) The proposed numerical model does not take into account the effects of three-body abrasion of wear process. In fact, after the generation of abrasive debris, abrasive debris will continue abrading the two rough surfaces in the form of three-body wear, the subsequent wear process may lead to further changes in the wear state and the statistical characteristics of the debris.

(2) Concerning the remaining wear life prediction method based on the abrasive debris, although this thesis utilized the equivalent of experimental data to verify the proposed method, there is no full-life degradation data of hydraulic pump with distribution of the debris particles number, size distribution and morphology experimental results. The potential accuracy promotion of the proposed method for the remaining wear life remains to be mining.

SECTION III: REFERENCES

This Section lists all the references cited in Sections I and II of this dissertation.

References

[1] L. Han, S. Wang, and C. Zhang, "A partial lubrication model between valve plate and cylinder block in axial piston pumps," *ARCHIVE Proceedings of the Institution of Mechanical Engineers Part C Journal of Mechanical Engineering Science 1989-1996 (vols 203-210),* vol. 229, 2015.

[2] H. Gao, C. Fei, G. Bai, and L. Ding, "Reliability-based low-cycle fatigue damage analysis for turbine blade with thermo-structural interaction," *Aerospace Science & Technology,* vol. 49, pp. 289-300, 2016.

[3] Z. Ma, S. Wang, C. Zhang, M. M. Tomovic, and T. Li, "A Load Sequence Design Method for Hydraulic Piston Pump Based on Time-Related Markov Matrix," *IEEE Transactions on Reliability,* vol. PP, pp. 1-12, 2018.

[4] J. Bergada, S. Kumar, D. L. Davies, and J. Watton, "A complete analysis of axial piston pump leakage and output flow ripples," *Applied Mathematical Modelling,* vol. 36, pp. 1731-1751, 2012.

[5] S. Guo, J. Chen, Y. Lu, Y. Wang, and H. Dong, "Hydraulic piston pump in civil aircraft: current status, future directions and critical technologies," *Chinese Journal of Aeronautics,* 2019.

[6] J. Ma, J. Chen, J. Li, Q. Li, and C. Ren, "Wear analysis of swash plate/slipper pair of axis piston hydraulic pump," *Tribology International,* vol. 90, pp. 467-472, 2015.

[7] L. Han, S. Wang, and C. Zhang, "A partial lubrication model between valve plate and cylinder block in axial piston pumps," *Proceedings of the Institution of Mechanical Engineers, Part C: Journal of Mechanical Engineering Science,* vol. 229, pp. 3201-3217, 2015.

[8] L. Du, X. Zhu, Y. Han, L. Zhao, and J. Zhe, "Improving sensitivity of an inductive pulse sensor for detection of metallic wear debris in lubricants using parallel LC resonance method," *Measurementence & Technology,* vol. 24, pp. 660-664, 2013.

[9] X. Zhu, D. Li, and Z. Jiang, "A 3×3 wear debris sensor array for real time lubricant oil conditioning monitoring using synchronized sampling," *Mechanical Systems & Signal Processing,* vol. 83, pp. 296-304, 2017.

[10] W. Hong, S. Wang, M. M. Tomovic, H. Liu, J. Shi, and X. Wang, "A Novel Indicator for Mechanical Failure and Life Prediction Based on Debris Monitoring," *IEEE Transactions on Reliability,* vol. PP, pp. 1-9, 2017.

[11] B. J. Roylance, "Ferrography—then and now," *Tribology International,* vol. 38, pp. 857-862, 2005.

[12] D. P. Anderson, "Wear Particle Atlas. Revised," *FOXBORO ANALYTICAL*

BURLINGTON MA, 1982.

[13] W. Hong, S. Wang, M. Tomovic, L. Han, and J. Shi, "Radial inductive debris detection sensor and performance analysis," *Measurement Science & Technology,* vol. 24, p. 5103, 2013.

[14] W. Hong, W. Cai, S. Wang, and M. M. Tomovic, "A Review for Mechanical Wear Debris Feature, Detection and Diagnosis," *Chinese Journal of Aeronautics,* vol. 31, 2017.

[15] T. Li, S. Wang, E. Zio, J. Shi, and W. Hong, "Aliasing Signal Separation of Superimposed Abrasive Debris Based on Degenerate Unmixing Estimation Technique," *Sensors,* vol. 18, p. 866, 2018.

[16] S. Wang, T. Wu, H. Wu, and N. Kwok, "Modeling Wear State Evolution Using Real-Time Wear Debris Features," *Tribology Transactions,* vol. 60, 2016.

[17] A. Kumar and S. K. Ghosh, "Size Distribution Analysis of Wear Debris Generated in HEMM Engine Oil for Reliability Assessment: A Statistical Approach," *Measurement,* 2018.

[18] M. Kovochich, E. S. Fung, E. Donovan, K. M. Unice, D. J. Paustenbach, and B. L. Finley, "Characterization of wear debris from metal-on-metal hip implants during normal wear versus edge-loading conditions," *Journal of Biomedical Materials Research Part B Applied Biomaterials,* vol. 106, 2017.

[19] M. Alemani, S. Gialanella, G. Straffelini, R. Ciudin, U. Olofsson, G. Perricone, *et al.*, "Dry sliding of a low steel friction material against cast iron at different loads: Characterization of the friction layer and wear debris," *Wear,* vol. s 376–377, pp. 1450-1459, 2017.

[20] H. C. Meng and K. C. Ludema, "Wear models and predictive equations: their form and content," *Wear,* vol. 181, pp. 443-457, 1995.

[21] R. Holm and E. Holm, "Electric contacts : theory and application," 1981.

[22] J. F. Archard, "Contact and Rubbing of Flat Surfaces," *Journal of Applied Physics,* vol. 24, pp. 981-988, 1953.

[23] R. L. Deuis, C. Subramanian, and J. M. Yellup, "Dry sliding wear of aluminium composites—A review," *Composites Science & Technology,* vol. 57, pp. 415-435, 1997.

[24] S. C. Lim and M. F. Ashby, "Overview no. 55 Wear-Mechanism maps," *Acta Metallurgica,* vol. 35, pp. 1-24, 1987.

[25] K. Hokkirigawa and K. Kato, "An experimental and theoretical investigation of ploughing, cutting and wedge formation during abrasive wear," *Tribology International,* vol. 21, pp. 51-57, 1988.

[26] T. D. Jacobs and R. W. Carpick, "Nanoscale wear as a stress-assisted chemical reaction," *Nature Nanotechnology,* vol. 8, pp. 108-112, 2013.

[27] B. Gotsmann and M. A. Lantz, "Atomistic Wear in a Single Asperity Sliding Contact," *Phys.rev.lett,* vol. 101, p. 125501, 2008.

[28] T. D. B. Jacobs, B. Gotsmann, M. A. Lantz, and R. W. Carpick, "On the Application of Transition State Theory to Atomic-Scale Wear," *Tribology Letters,* vol. 39, pp. 257-271, 2010.

[29] L. Pastewka, S. Moser, P. Gumbsch, and M. Moseler, "Anisotropic mechanical amorphization drives wear in diamond," *Nature Materials,* vol. 10, pp. 34-8, 2011.

[30] J. Zhong, R. Shakiba, and J. B. Adams, "Molecular dynamics simulation of severe adhesive wear on a rough aluminum substrate," *Journal of Physics D Applied Physics,* vol. 46, p. 055307, 2013.

[31] M. R. So/Rensen, K. W. Jacobsen, and P. Stoltze, "Simulations of atomic-scale sliding friction," *Physical Review B Condensed Matter,* vol. 53, p. 2101, 1996.

[32] A. Schirmeisen, "Wear: One atom after the other," *Nature Nanotechnology,* vol. 8, p. 81, 2013.

[33] R. Aghababaei, D. H. Warner, and J. F. Molinari, "Critical length scale controls adhesive wear mechanisms," *Nature Communications,* vol. 7, p. 11816, 2016.

[34] Z. D. Sha, V. Sorkin, P. S. Branicio, and Q. X. Pei, "Large-scale molecular dynamics simulations of wear in diamond-like carbon at the nanoscale," *Applied Physics Letters,* vol. 103, pp. 1174-1180, 2013.

[35] R. Aghababaei, T. Brink, and J. F. Molinari, "Asperity-Level Origins of Transition from Mild to Severe Wear," *Physical review letters,* vol. 120, p. 186105, 2018.

[36] P. Spijker and J. F. Molinari, "Dry Sliding Contact Between Rough Surfaces at the Atomistic Scale," *Tribology Letters,* vol. 44, pp. 279-285, 2011.

[37] K. Holmberg, A. Laukkanen, A. Ghabchi, M. Rombouts, E. Turunen, R. Waudby*, et al.*, "Computational modelling based wear resistance analysis of thick composite coatings," *Tribology International,* vol. 72, pp. 13-30, 2014.

[38] T. Yue and M. A. Wahab, "Finite element analysis of fretting wear under variable coefficient of friction and different contact regimes," *Tribology International,* vol. 107, 2017.

[39] L. Gui, X. Wang, Z. Fan, and F. Zhang, "A simulation method of thermo-mechanical and tribological coupled analysis in dry sliding systems," *Tribology International,* vol. 103, pp. 121-131, 2016.

[40] Kartini, E. Saputra, R. Ismail, J. Jamari, and A. P. Bayuseno, "Analysis of the Contact Area of Smooth and Rough Surfaces in Contact with Sphere Indenter Using Finite Element Method," in *MATEC Web of Conferences*, 2016, p. 04007.

[41] F. Kosior, N. Guyot, and G. Maurice, "Analysis of frictional contact problem

using boundary element method and domain decomposition method," *International Journal for Numerical Methods in Engineering,* vol. 46, pp. 65-82, 2015.

[42] S. Mainardi, "Adhesive contact of rough surfaces: comparison between numerical calculations and analytical theories," *European Physical Journal E Soft Matter,* vol. 30, p. 65, 2009.

[43] V. A. Yastrebov, G. Anciaux, and J. F. Molinari, "From infinitesimal to full contact between rough surfaces: Evolution of the contact area," *International Journal of Solids & Structures,* vol. 52, pp. 83-102, 2015.

[44] S. Li, "A boundary element model for near surface contact stresses of rough surfaces," *Computational Mechanics,* vol. 54, pp. 833-846, 2014.

[45] J. Allwood, "Survey and Performance Assessment of Solution Methods for Elastic Rough Contact Problems," *Journal of Tribology,* vol. 127, pp. 10-23, 2005.

[46] I. A. Polonsky and L. M. Keer, "A numerical method for solving rough contact problems based on the multi-level multi-summation and conjugate gradient techniques," *Wear,* vol. 231, pp. 206-219, 1999.

[47] S. Liu, Q. Wang, and G. Liu, "A versatile method of discrete convolution and FFT (DC-FFT) for contact analyses," *Wear,* vol. 243, pp. 101-111, 2000.

[48] A. Akchurin, R. Bosman, and P. M. Lugt, "A Stress-Criterion-Based Model for the Prediction of the Size of Wear Particles in Boundary Lubricated Contacts," *Tribology Letters,* vol. 64, p. 35, 2016.

[49] A. Akchurin, R. Bosman, and P. M. Lugt, "Generation of Wear Particles and Running-In in Mixed Lubricated Sliding Contacts," *Tribology International,* vol. 110, pp. 201-208, 2017.

[50] V. Done, D. Kesavan, K. R. Murali, T. Chaise, and D. Nelias, "Semi analytical fretting wear simulation including wear debris," *Tribology International,* vol. 109, pp. 1-9, 2017.

[51] T. Li, S. Wang, J. Shi, and Z. Ma, "An adaptive-order particle filter for remaining useful life prediction of aviation piston pumps," *Chinese Journal of Aeronautics,* 2017.

[52] T. Wu, Y. Peng, H. Wu, X. Zhang, and J. Wang, "Full-life dynamic identification of wear state based on on-line wear debris image features," *Mechanical Systems & Signal Processing,* vol. 42, pp. 404-414, 2014.

[53] I. El-Thalji and E. Jantunen, "Dynamic modelling of wear evolution in rolling bearings," *Tribology International,* vol. 84, pp. 90-99, 2015.

[54] J. Zhu, J. M. Yoon, D. He, and E. Bechhoefer, "Online particle-contaminated lubrication oil condition monitoring and remaining useful life prediction for

wind turbines," *Wind Energy,* vol. 18, pp. 1131-1149, 2015.

[55] J. Zhu, D. He, and E. Bechhoefer, "Survey of lubrication oil condition monitoring, diagnostics, prognostics techniques and systems," *Journal of Chemical Science & Technology,* vol. 2, pp. 100-115, 2012.

[56] W. Hong, W. Cai, S. Wang, and M. M. Tomovic, "Mechanical wear debris feature,detection,and diagnosis:A review," *Chinese Journal of Aeronautics,* vol. 31, 2018.

[57] W. Hong, S. Wang, M. M. Tomovic, H. Liu, and X. Wang, "A new debris sensor based on dual excitation sources for online debris monitoring," *Measurement Science & Technology,* vol. 26, 2015.

[58] L. Du and J. Zhe, "A high throughput inductive pulse sensor for online oil debris monitoring," *Tribology International,* vol. 44, pp. 175-179, 2011.

[59] X. Zhu, C. Zhong, and J. Zhe, "A high sensitivity wear debris sensor using ferrite cores for online oil condition monitoring," *Measurement Science & Technology,* vol. 28, p. 075102, 2017.

[60] L. Du, X. Zhu, Y. Han, and J. Zhe, "High Throughput Wear Debris Detection in Lubricants Using a Resonance Frequency Division Multiplexed Sensor," *Tribology Letters,* vol. 51, pp. 453-460, 2013.

[61] H. Zhan, Y. Song, H. Zhao, J. Gu, H. Yang, and S. Li, "Study of the sensor for on-line lubricating oil debris monitoring," *Sensors & Transducers,* vol. 175, pp. 214-219, 2014.

[62] Z. Zhong, S. Wang, W. Hong, and M. Tomovic, "Aliasing signal separation of oil debris monitoring," in *Industrial Electronics and Applications*, 2016, pp. 1682-1687.

[63] C. Li, J. Peng, and M. Liang, "Enhancement of the wear particle monitoring capability of oil debris sensors using a maximal overlap discrete wavelet transform with optimal decomposition depth," *Sensors,* vol. 14, p. 6207, 2014.

[64] J. Luo, D. Yu, and M. Liang, "Enhancement of oil particle sensor capability via resonance-based signal decomposition and fractional calculus," *Measurement,* vol. 76, pp. 240-254, 2015.

[65] D. Wang, W. Guo, and P. W. Tse, "An enhanced empirical mode decomposition method for blind component separation of a single-channel vibration signal mixture," *Journal of Vibration & Control,* vol. 22, 2015.

[66] J. H. Mcdermott, "The cocktail party problem," *Neural Computation,* vol. 17, pp. 1875-1902, 2009.

[67] L. Han, C. W. Li, S. L. Guo, and X. W. Su, "Feature extraction method of bearing AE signal based on improved FAST-ICA and wavelet packet energy," *Mechanical Systems & Signal Processing,* vol. s 62–63, pp. 91-99, 2015.

[68] A. Jourjine, S. Rickard, and O. Yilmaz, "Blind separation of disjoint orthogonal signals: demixing N sources from 2 mixtures," in *Acoustics, Speech, and Signal Processing, 2000. on IEEE International Conference*, 2000, pp. 2985-2988.

[69] O. Yilmaz and S. Rickard, "Blind separation of speech mixtures via time-frequency masking," *Signal Processing IEEE Transactions on,* vol. 52, pp. 1830-1847, 2004.

[70] A. Hussain, K. Chellappan, and M. S. Zamratol, "Speech enhancement using degenerate unmixing estimation technique and adaptive noise cancellation technique as a post signal processing," in *Biomedical Engineering and Sciences*, 2017, pp. 280-285.

[71] N. Chong, S. Nordholm, T. V. Ba, and I. Murray, "Tracking and separation of multiple moving speech sources via cardinality balanced multi-target multi Bernoulli (CBMeMBer) filter and time frequency masking," in *International Conference on Control, Automation and Information Sciences*, 2017, pp. 88-93.

[72] W. Hong, S. Wang, H. Liu, M. M. Tomovic, and Z. Chao, "A hybrid method based on Band Pass Filter and Correlation Algorithm to improve debris sensor capacity," *Mechanical Systems & Signal Processing,* vol. 82, pp. 1-12, 2016.

[73] J. Sun, H. Li, and B. Xu, "Prognostic for hydraulic pump based upon DCT-composite spectrum and the modified echo state network," *SpringerPlus,* vol. 5, p. 1293, 2016.

[74] Z. Zangenehmadar and O. Moselhi, "Assessment of remaining useful life of pipelines using different artificial neural networks models," *Journal of Performance of Constructed Facilities,* vol. 30, p. 04016032, 2016.

[75] M. Dong and Y. Peng, "Equipment PHM using non-stationary segmental hidden semi-Markov model," *Robotics and Computer-Integrated Manufacturing,* vol. 27, pp. 581-590, 2011.

[76] M. Dong and D. He, "Hidden semi-Markov model-based methodology for multi-sensor equipment health diagnosis and prognosis," *European Journal of Operational Research,* vol. 178, pp. 858-878, 2007.

[77] M. Dong and D. He, "A segmental hidden semi-Markov model (HSMM)-based diagnostics and prognostics framework and methodology," *Mechanical Systems & Signal Processing,* vol. 21, pp. 2248-2266, 2007.

[78] Y. Geng, S. Wang, and C. Zhang, "Life estimation based on unbalanced data for hydraulic pump," in *Ieee/csaa International Conference on Aircraft Utility Systems*, 2016, pp. 796-801.

[79] Z. He, S. Wang, K. Wang, and K. Li, "Prognostic analysis based on hybrid prediction method for axial piston pump," in *IEEE International Conference on Industrial Informatics*, 2012, pp. 688-692.

[80] Y. Liu, G. Ji, J. Li, and D. Zhao, "Physics-of-failure based approach for

predicting reliability of mechanical products," in *International Conference on Reliability, Maintainability and Safety*, 2014, pp. 878-881.

[81] B. Lamoureux, J. R. Massé, and N. Mechbal, "An Approach to the Health Monitoring of a Pumping Unit in an Aircraft Engine Fuel System," in *Chez proceedings of first European conference of the prognostics and health management society*, Dresden, 2012, pp. 1-7.

[82] J. Chen, C. Ma, D. Song, and B. Xu, "Failure prognosis of multiple uncertainty system based on Kalman filter and its application to aircraft fuel system," *Advances in Mechanical Engineering,* vol. 8, 2016.

[83] Y. Qian, R. Yan, and S. Hu, "Bearing degradation evaluation using recurrence quantification analysis and kalman filter," *IEEE Transactions on Instrumentation & Measurement,* vol. 63, pp. 2599-2610, 2014.

[84] D. Mba and L. C. K. Reuben, "Diagnostics and prognostics using switching Kalman filters," *Structural Health Monitoring,* vol. 13, pp. 296-306, 2014.

[85] Y. Liu, K. Dong, H. Wang, J. Liu, Y. He, and L. Pan, "Adaptive Gaussian sum squared-root cubature Kalman filter with split-merge scheme for state estimation," *Chinese Journal of Aeronautics,* vol. 27, pp. 1242-1250, 2014.

[86] X. Wang, S. Lin, S. Wang, Z. He, and C. Zhang, "Remaining useful life prediction based on the Wiener process for an aviation axial piston pump," *Chinese Journal of Aeronautics,* vol. 29, pp. 779-788, 2016.

[87] L. I. Tongyang, S. Wang, J. Shi, and M. A. Zhonghai, "An adaptive-order particle filter for remaining useful life prediction of aviation piston pumps," *Chinese Journal of Aeronautics,* vol. 31, pp. 941-948, 2018.

[88] C. Shi, S. Wang, X. Wang, and J. Wang, "Remaining useful life prediction based on particle filtering for high-speed pump in load sensing electro-hydrostatic actuator," in *CSAA/IET International Conference on Aircraft Utility Systems (AUS 2018)*, Guiyang, China, 2018, p. 6.

[89] H. Li, J. Sun, H. Ma, Z. Tian, and Y. Li, "A novel method based upon modified composite spectrum and relative entropy for degradation feature extraction of hydraulic pump," *Mechanical Systems and Signal Processing,* vol. 114, pp. 399-412, 2019.

[90] G. Xu, C. Ma, Z. Gao, X. Hu, and Y. Luo, "Modeling and simulation of aero-hydraulic pump wear failure," in *2017 Prognostics and System Health Management Conference (PHM-Harbin)*, 2017, pp. 1-7.

[91] E. Zio and G. Peloni, "Particle filtering prognostic estimation of the remaining useful life of nonlinear components," *Reliability Engineering & System Safety,* vol. 96, pp. 403-409, 2011.

[92] X. Liu, Z. Chen, C. Zhang, and J. Wu, "A novel temperature-compensated model for power Li-ion batteries with dual-particle-filter state of charge

estimation," *Applied Energy,* vol. 123, pp. 263–272, 2014.

[93] S. Yin and X. Zhu, "Intelligent particle filter and its application to fault detection of nonlinear system," *IEEE Transactions on Industrial Electronics,* vol. 62, pp. 3852-3861, 2015.

[94] Q. Miao, L. Xie, H. Cui, W. Liang, and M. Pecht, "Remaining useful life prediction of lithium-ion battery with unscented particle filter technique," *Microelectronics Reliability,* vol. 53, pp. 805-810, 2013.

[95] M. Rigamonti, P. Baraldi, E. Zio, and D. Astigarraga, "Particle filter-based prognostics for an electrolytic capacitor working in variable operating conditions," *IEEE Transactions on Power Electronics,* vol. 31, pp. 1-1, 2015.

[96] Y. Hu, P. Baraldi, F. D. Maio, and E. Zio, "A particle filtering and kernel smoothing-based approach for new design component prognostics," *Reliability Engineering & System Safety,* vol. 134, pp. 19–31, 2015.

[97] P. Baraldi, F. Mangili, and E. Zio, "Investigation of uncertainty treatment capability of model-based and data-driven prognostic methods using simulated data," *Reliability Engineering & System Safety,* vol. 112, pp. 94-108, 2013.

[98] M. Rigamonti, P. Baraldi, E. Zio, D. Astigarraga, and A. Galarza, "A particle filtering-based approach for the prediction of the remaining useful life of an aluminum electrolytic capacitor," in *2nd European Conference of the Prognostics and Health Management Society (PHME)*, Nantes, 2014, pp. 8-10.

[99] C. Guan, Z. Jiao, and S. He, "Theoretical study of flow ripple for an aviation axial-piston pump with damping holes in the valve plate," *Chinese Journal of Aeronautics,* vol. 27, pp. 169-181, 2014.

[100] GUANChangbin and JIAOZongxia, "Modeling and optimal design of 3 degrees of freedom helmholtz resonator in hydraulic system," *Chinese Journal of Aeronautics,* vol. 25, pp. 776-783, 2012.

[101] G. Fagogenis, D. Flynn, and D. Lane, "Novel RUL prediction of assets based on the integration of auto-regressive models and an RUSBoost classifier," in *Prognostics and Health Management*, 2014, pp. 1-6.

[102] D. Zhou, Z. Yu, H. Zhang, and S. Weng, "A novel grey prognostic model based on Markov process and grey incidence analysis for energy conversion equipment degradation," *Energy,* vol. 109, pp. 420-429, 2016.

[103] F. Gascón and F. Salazar, "Simulation of Rough Surfaces and Analysis of Roughness by MATLAB," in *MATLAB-A Ubiquitous Tool for the Practical Engineer*, ed: InTech, 2011.

[104] Y. Hu and K. Tonder, "Simulation of 3-D random rough surface by 2-D digital filter and Fourier analysis," *International journal of machine tools and manufacture,* vol. 32, pp. 83-90, 1992.

[105] J. Greenwood and J. Tripp, "The contact of two nominally flat rough surfaces," *Proceedings of the institution of mechanical engineers,* vol. 185, pp. 625-633, 1970.

[106] K. Johnson, "Contact Mechanics Cambridge Univ," *Press, Cambridge,* 1985.

[107] S. Liu and Q. Wang, "Studying contact stress fields caused by surface tractions with a discrete convolution and fast Fourier transform algorithm," *Journal of tribology,* vol. 124, pp. 36-45, 2002.

[108] Bhargava, VEMAGANTI, and Kumar, "Estimation of statistical parameters of rough surfaces suitable for developing micro-asperity friction models," *Wear,* vol. 316, pp. 6-18, 2014.

[109] P. Pawlus and W. Zelasko, "The importance of sampling interval for rough contact mechanics," *Wear,* vol. 276-277, pp. 121-129, 2012.

[110] R. M. Patrikar, "Modeling and simulation of surface roughness," *Applied Surface Science,* vol. 228, pp. 213-220, 2004.

[111] G. Zavarise, M. Borri-Brunetto, and M. Paggi, "On the resolution dependence of micromechanical contact models," *Wear,* vol. 262, pp. 42-54, 2007.

[112] V. L. Popov and R. Pohrt, "Adhesive wear and particle emission: Numerical approach based on asperity-free formulation of Rabinowicz criterion," *Friction,* pp. 1-14, 2018.

[113] B. Bhushan, *Modern tribology handbook, two volume set*: CRC press, 2000.

[114] J. L. Miller and D. Kitaljevich, "In-line oil debris monitor for aircraft engine condition assessment," in *Aerospace Conference Proceedings, 2000 IEEE*, 2000, pp. 49-56.

[115] F.-X. Wang, P. Lacey, R. Gates, and S. Hsu, "A study of the relative surface conformity between two surfaces in sliding contact," *Journal of Tribology,* vol. 113, pp. 755-761, 1991.

[116] Z. Fang, B. R. Patterson, and M. E. Turner Jr, "Modeling particle size distributions by the Weibull distribution function," *Materials characterization,* vol. 31, pp. 177-182, 1993.

[117] B. Roylance and G. Pocock, "Wear studies through particle size distribution I: Application of the Weibull distribution to ferrography," *Wear,* vol. 90, pp. 113-136, 1983.

[118] A. Beerbower, "Wear Rate Prognosis Through Particle Size Distribution," *Tribology & Lubrication Technology,* vol. 74, pp. 56-65, 2018.

[119] A. Kobayashi, W. Bonfield, Y. Kadoya, T. Yamac, M. Freeman, G. Scott*, et al.*, "The size and shape of particulate polyethylene wear debris in total joint replacements," *Proceedings of the Institution of Mechanical Engineers, Part H: Journal of Engineering in Medicine,* vol. 211, pp. 11-15, 1997.

[120] I. Catelas, J. D. Bobyn, J. B. Medley, J. J. Krygier, D. J. Zukor, and O. L. Huk, "Size, shape, and composition of wear particles from metal–metal hip simulator testing: effects of alloy and number of loading cycles," *Journal of Biomedical Materials Research Part A: An Official Journal of The Society for Biomaterials, The Japanese Society for Biomaterials, and The Australian Society for Biomaterials and the Korean Society for Biomaterials,* vol. 67, pp. 312-327, 2003.

[121] E. F. Finkin, "The wear of copper, aluminum, mild steel, and zinc, and their wear particle shape factors," *ASLE TRANSACTIONS,* vol. 7, pp. 377-382, 1964.

[122] A. Momber and Y. Wong, "Geometrical features of wear debris," *Journal of materials science,* vol. 40, pp. 3517-3522, 2005.

[123] X. Zhu, C. Zhong, and J. Zhe, "Lubricating oil conditioning sensors for online machine health monitoring – A review," *Tribology International,* vol. 109, pp. 473-484, 2017.

[124] E. Hoffmann, D. Kolossa, and R. Orglmeister, "A batch algorithm for blind source separation of acoustic signals using ICA and time-frequency masking," in *International Conference on Independent Component Analysis and Signal Separation*, 2007, pp. 480-487.

[125] S. S. A. Zaidi, M. M. Ali, F. Aftab, Y. Shahid, and M. Khurram, "Name spotting over low signal-to-noise ratio (SNR) using Blind Source Separation and Connectionist Temporal Classification," in *International Conference on Communication, Computing and Digital Systems*, 2017, pp. 320-325.

[126] B. Freisleben, C. Hagen, and M. Borschbach, "A neural network for the blind separation of non-Gaussian sources," in *IEEE International Joint Conference on Neural Networks Proceedings, 1998. IEEE World Congress on Computational Intelligence*, 1998, pp. 837-842 vol.2.

[127] P. Huang and M. Kim, "Singing-Voice Separation From Monaural Recordings Using Deep Recurrent Neural Networks," 2014.

[128] P. S. Huang, M. Kim, M. Hasegawa-Johnson, and P. Smaragdis, "Deep learning for monaural speech separation," in *IEEE International Conference on Acoustics, Speech and Signal Processing*, 2014, pp. 1562-1566.

[129] F. Weninger, F. Eyben, and B. Schuller, *Single-channel speech separation with memory-enhanced recurrent neural networks*, 2014.

[130] H. Y. Lee, J. W. Cho, M. Kim, and H. M. Park, "DNN-Based Feature Enhancement Using DOA-Constrained ICA for Robust Speech Recognition," *IEEE Signal Processing Letters,* vol. 23, pp. 1091-1095, 2016.

[131] A. A. Nugraha, A. Liutkus, and E. Vincent, "Multichannel Audio Source Separation With Deep Neural Networks," *IEEE/ACM Transactions on Audio Speech & Language Processing,* vol. 24, pp. 1652-1664, 2016.

[132] T. Li, J. Shi, S. Wang, E. Zio, and Z. Ma, "Mesoscale Numerical Modeling for Predicting Wear Debris Generation," *Tribology Letters,* vol. 67, p. 38, 2019.

SECTION IV: PUBLICATIONS

This Section corrects the papers related to this Ph.D. research activity. The research activity has led to the acceptance (7) and the submission (2) of 9 manuscripts at international peer-reviewed journals and books (see TABLE 12), and the acceptance of 6 papers presented at the international academic conferences (see TABLE 13).

Four journal papers and Four conference papers which introduce the core techniques of this Ph.D. work are attached in this Section.

TABLE 12 Publications in international peer-reviewed journals

No.	Title	Authors	Status
1[J]	Mesoscale Numerical Modeling for Predicting Wear Debris Generation	**T. Li,** J. Shi, S. Wang, E. Zio, Z. Ma	*Tribology Letters*, 2019, 67(2): 38.
2[J]	Aliasing signal separation of superimposed abrasive debris based on degenerate unmixing estimation technique	**T. Li,** S. Wang, E. Zio, J. Shi W. Hong.	*Sensors*, 2018, 18(3): 866.
3[J]	An adaptive-order particle filter for remaining useful life prediction of aviation piston pumps	**T. Li,** S. Wang, J. Shi, Z. Ma	*Chinese Journal of Aeronautics*, 2018, 31(5): 941-948.
4[J]	An Energy Based Coupling Degradation Propagation Model and Its Application on Aviation Actuation System	**T. Li,** S. Wang, J. Shi, E. Zio, X. Cui	*Chinese Journal of Aeronautics*, 2019. (Accepted)
5[J]	A Load Sequence Design Method for Hydraulic Piston Pump Based on Time-Related Markov Matrix	Z. Ma, S. Wang, C. Zhang, M. Tomovic, **T. Li**	*IEEE Transactions on Reliability*, 2018, 67(3): 1237-1248.
6[J]	Fault diagnosis of an intelligent hydraulic pump based on a nonlinear unknown input observer	Z. Ma, S. Wang, J. Shi, **T. Li**	*Chinese Journal of Aeronautics*, 2018, 31(2): 385-394.
7[J]	System Reliability Assessment based on Energy Dissipation: Modeling and Application in Electro-Hydrostatic Actuation System	X. Cui, S. Wang, **T. Li,** J. Shi	*Energies*, 2019, 12(18): 3572.
8[J]	A Numerical Approach for Predicting the Remaining Useful Life of an Aviation Hydraulic Pump Based on Monitoring Abrasive Debris Generation	**T. Li,** J. Shi, S. Wang, E. Zio, Z. Ma	*Mechanical Systems and Signal Processing,* 2020, 136: 106519.

9[J]	A General Correction Framework for Aliasing Error of Inductive Oil Debris Detection Based on Artificial Neural Network	W. Hong, **T. Li,** S. Wang, E. Zio Z. Zhou	*Measurement Science and Technology, under review*

TABLE 13 Publications in international conferences

No.	Title	Authors	Status
1[C]	Degrading process simulation of aviation hydraulic pump with lifetime experiment data based on hidden semi-Markov model	**T. Li,** S. Wang, J. Shi, Z. Ma	IEEE Conference on Industrial Electronics and Applications (ICIEA 2017). IEEE, 2017: 624-629
2[C]	Simulation on neural networks for DUET-based delay estimation of abrasive debris signal separation	**T. Li,** S. Wang, J. Shi, E. Zio Z. Ma	CSAA/IET International Conference on Aircraft Utility Systems 2018 (AUS 2018), 230-6.
3[C]	Mechanical Wear Life Prediction Based on Abrasive Debris Generation	**T. Li,** S. Wang, J. Shi, E. Zio	2019 Prognostics and System Health Management Conference (PHM-Paris). IEEE, 2019: 79-84.
4[C]	Aliasing Signal Separation for Superimposition of Inductive Debris Detection Using CNN-Based DUET	**T. Li,** S. Wang, E. Zio J. Shi, Z. Yang	IEEE Conference on Industrial Electronics and Applications 2019 (ICIEA 2019)
5[C]	Experimental Study on Inductive Method for Online Material Loss Detection with High Debris Concentration	**T. Li,** S. Wang, E. Zio J. Shi, W. Hong	The 2nd International Conference on Material Strength and Applied Mechanics (MSAM 2019), IOP Conference Series: Materials Science and Engineering, Volume 629, Number 1
6[C]	A Delay-based Reliability Assessment for Multi UAV with Time-varying Topologies	X. Cui, S. Wang, J. Shi, **T. Li**	CSAA/IET International Conference on Aircraft Utility Systems 2018 (AUS2018)

PAPER 1[J]: MESOSCALE NUMERICAL MODELING FOR PREDICTING WEAR DEBRIS GENERATION

Tongyang Li, Jian Shi*, Shaoping Wang, Enrico Zio and Zhonghai Ma

Tribology Letters, 2019, 67(2): 38.

https://doi.org/10.1007/s11249-019-1150-2

PAPER 2[J]: ALIASING SIGNAL SEPARATION OF SUPERIMPOSED ABRASIVE DEBRIS BASED ON DEGENERATE UNMIXING ESTIMATION TECHNIQUE

Tongyang Li, Shaoping Wang, Enrico Zio, Jian Shi* and Wei Hong

Sensors, 2018, 18(3): 866.

https://doi.org/10.3390/s18030866

PAPER 3[J]: AN ADAPTIVE-ORDER PARTICLE FILTER FOR REMAINING USEFUL LIFE PREDICTION OF AVIATION PISTON PUMPS

Tongyang Li, Shaoping Wang, Jian Shi* and Zhonghai Ma.

Chinese Journal of Aeronautics, 2018, 31(5): 941-948.

https://doi.org/10.1016/j.cja.2017.09.002

PAPER 8[J]: A NUMERICAL APPROACH FOR PREDICTING THE REMAINING USEFUL LIFE OF AN AVIATION HYDRAULIC PUMP BASED ON MONITORING ABRASIVE DEBRIS GENERATION

Tongyang Li, Jian Shi*, Shaoping Wang, Enrico Zio and Zhonghai Ma

Mechanical Systems and Signal Processing, 2020, 136: 106519.

https://doi.org/10.1016/j.ymssp.2019.106519

PAPER 2[C]: SIMULATION ON NEURAL NETWORKS FOR DUET-BASED DELAY ESTIMATION OF ABRASIVE DEBRIS SIGNAL SEPARATION

Tongyang Li, Shaoping Wang, Jian Shi*, Enrico Zio and Zhonghai Ma

CSAA/IET International Conference on Aircraft Utility Systems 2018, 230-6

https://doi.org/10.1049/cp.2018.0304

PAPER 3[C]: MECHANICAL WEAR LIFE PREDICTION BASED ON ABRASIVE DEBRIS GENERATION

Tongyang Li, Shaoping Wang, Jian Shi* and Enrico Zio

2019 Prognostics and System Health Management Conference (PHM-Paris). IEEE, 2019: 79-84.

https://doi.org/10.1109/PHM-Paris.2019.00021

PAPER 4[C]: ALIASING SIGNAL SEPARATION FOR SUPERIMPOSITION OF INDUCTIVE DEBRIS DETECTION USING CNN-BASED DUET

Tongyang Li, Shaoping Wang, Enrico Zio, Jian Shi* and Zhe Yang

2019 14th IEEE Conference on Industrial Electronics and Applications (ICIEA)

https://doi.org/10.1109/ICIEA.2019.8834290

PAPER 5[C]: EXPERIMENTAL STUDY ON INDUCTIVE METHOD FOR ONLINE MATERIAL LOSS DETECTION WITH HIGH DEBRIS CONCENTRATION

Tongyang Li, Shaoping Wang, Enrico Zio, Jian Shi* and Wei Hong

The 2nd International Conference on Material Strength and Applied Mechanics (MSAM 2019)

https://doi.org/10.1088/1757-899X/629/1/012031